Performance evaluation of different satellite radar altimetry missions for monitoring inland water bodies

A thesis accepted by the the Faculty of Aerospace Engineering and Geodesy of the University of Stuttgart in partial fulfillment of the requirements for the degree of Doctor of Engineering Sciences (Dr.-Ing.)

by

Shirzad Roohi

born in Sananadaj, Kurdistan, Iran

Main referee:	Prof. Dr.-Ing. Nico Sneeuw
Co-referees:	Prof. Dr.-Ing. Florian Seitz
	Prof. Dr.-Eng. Hossein Nahavandchi
Date of defence:	31.03.2017

Institute of Geodesy
University of Stuttgart
March 2017

Contents

List of Figures

List of Tables

Abstract

Inland water bodies, e.g. lakes and rivers, play vital roles in society and in nature. Moreover, these water bodies can be considered as integrators of environmental change to study climate effects and hydrological cycle at global and regional scales. Because changes in the water level of lakes and rivers indicate changes in climatic parameters, such as precipitation and evaporation, it is necessary to monitor water level variation of inland water bodies continuously to understand long term changes.

Traditional methods, e.g. using in-situ gauges, provide precise water level determination. But they can not monitor these water bodies in a way that today's human needs are to be satisfied, because in-situ gauge networks do not cover all inland water bodies and their data are not publicly available. Furthermore, they are expensive to install and to maintain, especially in remote areas. In-situ gauge networks follow national policy and there is not a unified data base of their measurements.

Satellite altimetry as a space-borne technology helps us to partially solve the issue of water level monitoring. This technique was originally designed to observe ocean water surface. But due to advances in satellite radar systems and in data processing methodologies, the application of satellite altimetry has been extended to monitor small lakes and narrow rivers over the past 20 years.

So far, studying water level variations of inland water bodies has been a challenge for satellite altimeters in terms of spatial and temporal resolution as well as accuracy of water level determination. Due to a relatively large radar footprint, the illuminated area inside the footprint can be inhomogeneous, i.e. consisting of water, land and vegetation. Therefore, responses to the radar pulses from such a surface are complex and lead to multi-peak waveforms (corrupted waveforms). Seriously corrupted waveforms need to be analyzed to extract optimal ranges.

Retracking is an effective method to improve the accuracy of the range measurement from contaminated waveforms and, consequently, to determine a more accurate water level. The design of an optimal retracking algorithm appropriate for a specific inland water body is very important in this respect. The quality of retracked water level depends on the type of altimeters and on the algorithm that is used in the retracking process. Moreover, the shape and size of the inland water bodies can affect the quality of the water level determination.

In this thesis, we analyzed the waveforms in two different ways: full-waveform and sub-waveform retracking. For this purpose, different physical and empirical retracking algorithms have been employed to retrack the waveforms.

In full-waveform retracking, for a given waveform one retracked range correction is estimated. But in sub-waveform retracking more than one retracked range correction can be calculated. We analyze all sub-waveforms in a given waveform and select the optimal one to retrack and consequently to determine water level variations. Three different analyses have been performed to select the optimal sub-waveform. In the first analysis we retracked only the first sub-waveform for all of the waveforms. In the second analysis all detected sub-waveforms in a given waveform are retracked to calculate the mean retracked range correction. In the last analysis we retrack the sub-waveform that provides the water level with minimum RMS with respect to model fits.

For a given satellite, first we determine the water level according to on-board retrackers. The results of the on-board retrackers have been validated against available in-situ gauge data to find the best on-board retracker. Then, the full and sub-waveforms have been processed by different retracking algorithms to define the retracked water level. The retracked water level derived from different retracking scenarios have been compared with in-situ gauge data to evaluate the accuracy of each scenario. Finally, the results of the best on-board retracker were compared with the results from post-processing the waveforms to find the most accurate water level estimator.

Radar characteristics and geometry of the satellite orbit, that affect on the altimeter's performance, are designed based on main objectives of a given mission. Monitoring inland water bodies have not been the main objectives for the altimetry missions till now. We therefore do our analysis over data from different altimeters and evaluate their performance in water level monitoring of different inland water bodies. To complete our analysis, a comparison between different satellite altimeters has been performed to assess the performance of each altimeter in continental water level determination. We selected challenging objects with different shapes and sizes in different continents. For a given object, two or three satellite altimetry data sets have been analyzed to study water level variations.

We used different satellite altimetry missions in our study, divided into pulse-limited and beam-limited altimeters. For the pulse-limited altimeters we selected Envisat, Jason-2, SARAL and CryoSat-2 LRM and for the beam-limited ones we used CryoSat-2 SAR and SARIn modes and ICESat satellite altimeters. GDR and SGDR data of these altimeters have been analyzed over four lakes: Neagh (Northern Ireland), Nasser (Egypt), Urmia (Iran) and Qinghai (China). We also analyzed the same data type of Envisat, Jason-2 and SARAL missions over different sections of the Danube river.

We have found that over inland water bodies it is necessary to retrack the waveforms to achieve a qualified water level determination. Comparing the results from the on-board retrackers with those of the post-processed waveforms indicates that the retracked water level is more accurate. Our numerical results of the waveform retracking show that the sub-waveform outperforms the full-waveform especially over small lakes and complex shape (even large) lakes as well as over narrow rivers, e.g. Danube river. Over lakes Neagh and Nasser the beam-limited altimeters show better performance than the pulse-limited altimeters. In the case of Urmia lake, we analyzed only pulse-limited altimeters. Envisat provides the water level more accurately than CryoSat-2 LRM. Over Qinghai lake, covered by beam- and pulse-limited altimeters, both Envisat and CryoSat-2 LRM have the same performance. They show better performance than ICESat. Over Danube river, Envisat and SARAL show the same performance which is better than that of Jason-2.

If we compare the results of all retracking scenarios for all missions, we can conclude that the mean sub-waveform retracked with the threshold retracker is the best retracking scenario to monitor small and complex shape inland water bodies. The first sub-waveform retracked with this retracker is an alternative scenario for the inland water bodies.

Zusammenfassung

Binnengewässer, wie z.B. Seen und Flüsse, spielen eine wichtige Rolle für Mensch und Natur. Darüber hinaus können diese Gewässer als Integratoren von Umweltänderungen angesehen werden, um Klimaeffekte und den Wasserkreislauf auf globaler und regionaler Ebene zu studieren. Weil Änderungen im Pegel von Seen und Flüssen Änderungen der Klimaparameter, wie Niederschlag und Verdunstung, anzeigen, ist es notwendig, Pegeländerungen von Binnengewässern kontinuierlich zu berwachen, um langfristige Änderungen zu verstehen.

Traditionelle Methoden, wie Pegelstationen, ermöglichen genaue Wasserstandsmessungen. Sie können aber diese Gewässer nicht in einer Weise beobachten, dass alle Erfordernisse erfüllt werden, weil Pegelnetzwerke nicht gleichmäßig verteilt und die Daten nicht immer öffentlich verfügbar sind. Außerdem sind sie Installation und Instandhaltung teuer, speziell in abgelegenen Gegenden. Pegelnetzwerke sind nationaler Politik unterworfen und es gibt keine vereinheitlichte Basis ihrer Messungen. Satellitenaltimetrie als weltraumgestützte Technologie hilft uns, das Problem der Wasserstandsüberwachung teilweise zu lösen. Ursprünglich wurde diese Technik entwickelt, um die Ozeanoberfläche zu beobachten. Aber wegen der Fortschritte bei Satellitenradarsystemen und Datenprozessierungsmethoden konnte die Anwendbarkeit der Satellitenaltimetrie auch auf die Überwachung kleiner Seen und schmaler Flüsse ausgeweitet werden. Diese Technologie wird seit mehr als 20 Jahren dafür eingesetzt, Wasserstandsänderungen von Binnengewässern zu studieren.

Bislang war das Messen von Wasserstandsänderungen dieser Gewässer eine Herausforderung für Satellitenaltimeter bezüglich räumlicher und zeitlicher Auflösung wie auch der Genauigkeit der Wasserstandsermittlung. Wegen des relativ großen Radar-Fußabdrucks kann das beleuchtete Gebiet innerhalb des Fußabdrucks inhomogen sein, d.h. es kann aus Wasser, Boden und Vegetation bestehen. Daher sind die reflektionte Radarpulse einer solchen Oberfläche komplex und führen zu sogenannten multi-peak Wellenform (beschädigte Wellenform). Beträchtlich beschädigte Wellenform müssen analysiert werden, um einen optimale Abstandsmessung zu extrahieren.

Retracking ist eine effektive Methode, um bei beschädigten Wellenform die Genauigkeit der Entfernungsmessung zu steigern und, damit verbunden, einen genaueren Wasserstand zu ermitteln. In diesem Zusammenhang ist es wichtig, den Entwurf eines Retracking-Algorithmus auf ein bestimmtes Binnengewässer anzupassen. Die Qualität der retrackten Wasserstände hängt von Altimetertyp und dem im Retracking-Prozess verwendeten Algorithmus ab. Weiterhin können Form und Größe des Binnengewässers die Qualität der Wasserstandsermittlung beeinflussen.

In dieser Studie analysieren wir die Wellenform auf zwei verschiedenen Wegen mittels Sogenannten Full-Wellenform- und Sub-Wellenform-Retracking. Dafür wurden verschiedene physikalische und empirische Retracking-Algorithmen eingesetzt.

Beim Full-Wellenform-Retracking wird für eine gegebene Wellenform eine retrackte Entfernungskorrektur geschätzt, während beim Sub-Wellenform-Retracking mehr als eine retrackte Entfernungskorrektur berechnet werden kann. Wir decken alle Sub-Wellenform einer gegebenen Wellenform auf und wählen daraus die optimale aus, um diese zu retracken und schließlich die Wasserstandsänderungen zu bestimmen. Drei unterschiedliche Analysen

wurden durchgeführt, um die optimale Sub-Wellenform auszuwählen. In der ersten Analyse retracken wir nur die erste Sub-Wellenform. In der zweiten Analyse werden alle erkannten Sub-Wellenform retrackt, um die durchschnittliche retrackte Entfernungskorrektur zu berechnen. In der letzten Analyse retracken wir die Sub-Wellenform, welche den Wasserstand mit minimalem RMS gegenüber passenden Modellen lieferte.

Für einen gegebenen Satelliten ermitteln wir zuerst den Wasserstand mit den On-Board-Retrackern. Die Ergebnisse werden mittels verfügbaren Pegeldaten validiert, um den besten On-Board-Retracker zu finden. Danach wurden die Full- und Sub-Wellenform mit unterschiedlichen Retracking-Algorithmen prozessiert, um den retrackten Wasserstand zu ermitteln. Die retrackten Wasserstände aus verschiedenen Retracking-Szenarien wurden mit Pegeldaten verglichen, um die Genauigkeit eines jeden Szenarios zu beurteilen. Schließlich wurden die Ergebnisse des besten On-Board-Retrackers mit den Ergebnissen des Wellenform-Post-Processings verglichen, um den genauesten Wasserstandsschätzer zu finden. Außerdem wurde ein Vergleich zwischen verschiedenen Satelliten-Altimetern durchgeführt, um deren Leistungsfähigkeit bei der Wasserstandsermittlung zu bewerten.

Radar-Charakteristiken und die Geometrie des Satellitenorbits, welche die Altimeterleistungsfähigkeit beeinflussen, werden entsprechend der Hauptziele einer gegebenen Mission geplant. Das Monitoring von Binnengewässern war bislang kein Hauptziel von Altimetriemissionen. Deshalb analysieren wir verschiedene Altimeter und werten deren Leistungsfähigkeit in der Überwachung verschiedener Binnengewässer aus. Unsere Analyse schließt mit dem Vergleich verschiedener Altimeter, um deren Leistungsfähigkeit in der Ermittlung kontinentaler Wasserstände zu bewerten. Wir haben hydrologische Objekte von unterschiedlicher Form und Größe auf verschiedenen Kontinenten ausgewählt. für ein gegebenes Objekt wurden zwei oder drei Satelliten-Altimetriedatensätze analysiert, um Wasserstandsänderungen zu studieren.

Wir haben in unserer Studie verschiedene Satelliten-Altimetriemissionen verwendet, welche pulslimitierten und strahllimitierten Altimetern zugeordnet werden können. Für die pulslimitierten Altimeter haben wir Envisat, Jason-2, SARAL und CryoSat-2 LRM ausgewählt. Für die strahllimitierten Altimeter haben wir die CryoSat-2 (SAR- und SARIn-Modus) und ICESat benutzt. GDR- und SGDR-Daten dieser Altimeter wurden über vier Seen analysiert: Neagh (nördlich Irland), Nasser (Ägypten), Urmia (Iran) und Qinghai (China). Wir haben ebenfalls die selben Datentypen der Envisat-, Jason-2- und SARAL-Missionen über verschiedenen Teilen der Donau analysiert.

Wir haben herausgefunden, dass es über Binnengewässern notwendig ist, die Wellenform zu retracken, um eine geeignete Wasserstandsermittlung zu erzielen. Ein Vergleich der Ergebnisse der On-Board-Retracker mit denjenigen der post-prozessierten Wellenform zeigt, dass der retrackte Wasserstand genauer ist als derjenige der On-Board-Retracker. Unsere numerischen Ergebnisse des Wellenform-Retrackings zeigen, dass die Sub-Wellenform Ergebniss besser sind als die mit Full-Wellenform, besonders über kleinen Seen und solchen Seen (auch größerer) mit komplizierten Formen als auch schmalern Flüssen, z.B. Donau. Über den Seen Neagh and Nasser zeigen strahllimitierte Altimeter eine bessere Leistungsfähigkeit als pulslimitierte Altimeter. Im Fall des Urmia-Sees haben wir nur pulslimitierte Altimeter analysiert. Hier liefert Envisat einen genaueren Wasserstand als CryoSat-2 LRM. Über dem Qinghai-See, der mit strahl- und pulslimitierten Altimetern abgedeckt ist, zeigen sowohl Envisat als auch CryoSat-2 eine bessere Leistungsfähigkeit als ICESat. Über der Donau zeigen Envisat und SARAL die gleiche Leistungsfähigkeit, welche besser ist als die von Jason-2.

Wenn wir alle Ergebnisse von allen Retracking-Szenarien aller Missionen vergleichen, können wir den Schluss ziehen, dass die mittlere Sub-Wellenform, die mittls Threshold-Retracker retrackt wurden, das beste Retracking-Szenario für kleine Binnengewässer und solche mit komplizierter Form ist.

Chapter 1

Introduction

A sufficient supply of clean and freshwater is a fundamental element in society and in nature. Water plays a vital role in human survival and economic and industrial developments. However water is not distributed evenly on Earth's surface in terms of space and time. Inland water bodies are an essential component of the hydrological cycle. They are integrators of environmental changes that occur at global, regional and local scales. Lakes contain about 74.5% of the surface freshwater and rivers contribute 1.8% (Biancamaria et al., 2010). They support domestic, agricultural and industrial water supply. Inland water bodies are the habitat for diverse biological communities. Many human activities , e.g. fishery, agriculture, urban and industrial water purification and flood management, rely on the inland water. These activities change the quantity and the quality of water which can be a potential threat not only to the ecosystem but also to human life. Furthermore, because of water resource limitations climate change can accelerate the water reduction of inland water bodies. Therefore, due to their important role, inland water bodies need to be monitored.

An optimized water management for the inland water bodies requires the knowledge of the surface water resource distribution and water level changes. One must know how the storage of these water bodies change and how they react to climate change and human activities. Hydrology, as a discipline dealing with the water cycle, needs accurate information of the water volume and level changes as well as distribution of water at the global and regional scale. Monitoring and modeling of water level variations and discharges are fundamental for hydrology to develop and to manage regional water resources. Despite its important role, hydrology still depends on traditional and old measurement networks, i.e. in-situ gauges.

The in-situ gauges usually provide daily measurements. So they have enough temporal resolution for water level measurements of the inland water bodies. But with a poor spatial coverage, the in-situ gauge networks are not able to provide enough input data to hydrological models. Spatial distribution of these networks is not homogeneous around the inland water bodies, especially in developing countries. It is difficult to install these network in remote areas. In-situ gauge stations are vulnerable especially during the flood seasons and their maintenance, establishment and operation are expensive and difficult. Since installation of the in-situ gauge networks follows national policy there is no unified database of their measurements to access openly. Particularly in boundary zones sharing these data would be very important. It would require an agreement between governments of different countries (Biancamaria et al., 2010). Moreover when and where in-situ gauge time series are accessible, they usually suffer from gaps in recording the measurements and from differences in processing and quality control. During the last 10–15 years the number of in-situ gauge stations globally has decreased significantly (Shiklomanov et al., 2002) which is a great concern for the scientific community in detecting the impact of global change on the hydrological cycle.

Satellite radar altimetry helps us to partially overcome these limitations. It is a sophisticated and mature space-borne technology originally designed to measure ocean and sea surface heights. It has revolutionized the ocean science with its unprecedented accuracy of several centimeters in determining the sea surface height from space (Fu and Cazenave, 2001). There has been significant improvement in the radar altimetry missions since launching the first satellite altimeter in 1978. Figure 1.1 represents the schematic improvement of the orbit error of the satellite altimetry missions to sense the ocean variations.

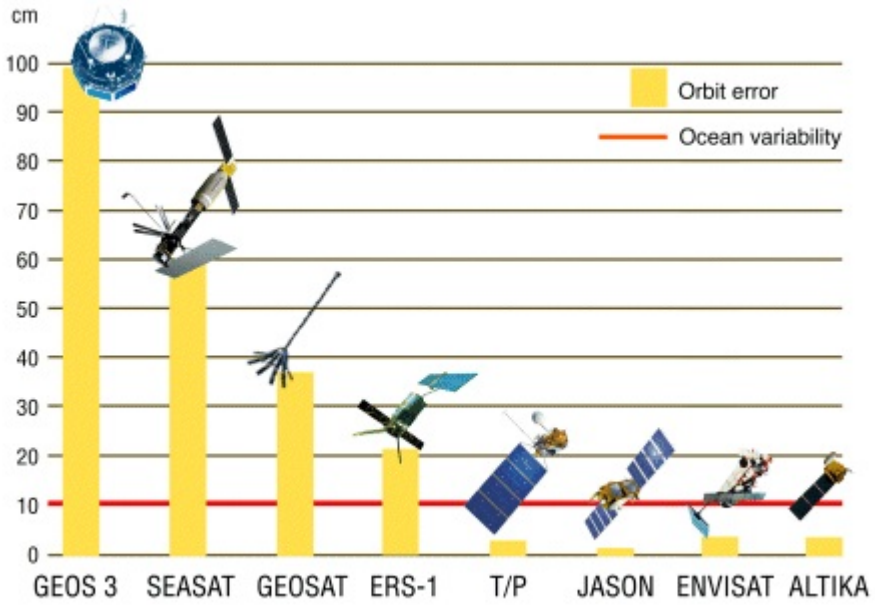

Figure 1.1: *Schematic representation of orbit error of the altimetry missions over the ocean surface (http://www.altimetry.info)*

Today, due to advances in radar systems and data processing methodology, satellite altimeters provide accurate measurements over not only open ocean but also over inland water bodies, e.g. lakes and rivers. The main advantage is that radar altimeters sample the Earth's surface day and night in all-weather conditions (Vignudelli et al., 2011). Thanks to their high accuracy, repeatability and stability, they have become an irreplaceable tool to address a wide variety of scientific questions from global ocean monitoring, long-term sea level rise, climate change to monitoring water level variations of small lakes and narrow rivers. Today there is increasing demand for satellite altimeter observations over the coastal zones and small inland water bodies. The radar system mounted on the satellite platforms can observe monthly, seasonal and annual variations of inland water bodies with respect to a specific reference frame to have a globally consistent uniform database. This technique permits a systematic monitoring for lakes and rivers. It can provide water level measurements for most of the water bodies over decades with a revisit time on each object ranging from a few days to a few months depending on the orbit. For instance the Topex/Poseidon, Jason-1 and Jason-2 satellite altimetry missions have a 10 days repeat cycle whereas for CryoSat-2 the revisit time is 369 days leading to a very dense coverage of the Earth's surface.

Several studies have been performed across the world based on the satellite altimetry measurements to determine water level variations. We found that in these studies the quality of water

level measurement depends on the shape and size of the water objects as well as on methodologies and algorithms used to determine water level variations. The accuracy of water level variations varies from a few to several centimeters.

Over oceans, large seas and lakes satellite altimeters perform well. They provide water level measurements with accuracy of a few centimeter. Over the Antarctic ocean Yang et al. (2012) obtained less than 10 cm of RMS in water level determination from ERS-1 mission data compared with tide gauge time series. Jain et al. (2015) investigated sea surface height changes in the Arctic region based on CryoSat-2 SAR mode data. They estimated sea surface anomaly with an RMS of 3 cm. Pascual et al. (2006) compared four different altimetry missions data (Jason-1, ERS-2, Envisat and Topex/Poseidon) to derive the sea level globally. They arrived at 5–10 cm RMS for the sea level time series. From the Topex/Poseidon mission data, tide heights were estimated by Shum et al. (1997) and Le Traon et al. (2001) with an RMS of 2–3 cm over the deep ocean. Fenoglio-Marc et al. (2015) analyzed CryoSat-2 SAR mode data about 10 km away from the coast in the German Bight during 2011–2012 to determine sea surface height, significant wave height and wind speed. They arrived at an RMS of 7 cm for the sea surface height relative to in-situ gauge data. Sea surface height at 1–7 km away from the coast, e.g. close to California, Florida, New Jersey and Louisiana in USA, was determined by Tseng et al. (2014) with 21 cm RMS with respect to in-situ gauge data. Lebedev and Kostianoy (2005) studied water level variations of Caspian sea during 1992–2004 from Topex/Poseidon and Jason-1 mission data. Instead of RMS, they used correlation coefficients between water level from Jason-1 and from in-situ gauge data to validate satellite results. They arrived at 96% correlation in the validation process. A comparison between in-situ hydrological data and retracked water level from Topex/Poseidon in (Morris and Gill, 1994) showed very good performance of this mission over the Great lakes. An RMS of about 4 cm was obtained in this study.

According to these studies satellite altimeters are showing a good performance, i.e. a few centimeters RMS, over the ocean, coastal zones (at more than 10 km distance from the coast) and large lakes. Over these areas the illuminated surface inside the radar footprint is homogeneous, i.e. there is only one type of terrain (water) inside the footprint. The response to the radar pulse from such a surface creates waveforms with a simple shape according to the Brown model in equation (2.8). Therefore extracted ranges from the simple (uncorrupted) waveforms are accurate and lead to accurate water level determination. If one goes closer toward the coast, i.e. a few kilometers, the altimeters are providing a larger RMS (Tseng et al., 2014), because the reflections would be complex due to the presence of non-water materials inside the illuminated surface.

Nowadays the application of satellite radar altimetry has been extended to monitor inland water bodies because of the advances in the radar systems and methodologies for data processing. But over these objects the performance of satellite altimetry is limited in terms of not only spatial and temporal resolution but also the accuracy of water level determination. Over inland water bodies the area inside the footprint of the radar can be a complex terrain. Therefore responses to the radar pulse would be partially from land or vegetation canopy that contaminate the measured waveform. This contamination reduces the accuracy of water level determination.

Waveform retracking as an effective method helps us to increase the accuracy of water level measurement specially over small and shallow inland water bodies. This technique permits us to extend the application of satellite altimetry to monitor small lakes and narrow rivers. Retracking can be performed in two forms: full-waveform retracking or sub-waveform retracking,

based on different retracking algorithms. In the full-waveform retracking the whole of a given waveform is considered to be one waveform. Then it is retracked by retracking algorithms. In the sub-waveform retracking, a given waveform is supposed to be a combination of a number of small waveforms called sub-waveform each of which results from different scatters. Each sub-waveform is then retracked. In chapter 3 the full- and sub-waveform will be described in more detail.

Waveform retracking has been used in different studies over different objects to define water level variations. Hwang et al. (2005) analyzed data from Topex/Poseidon mission for different lakes in China. They found contaminated waveforms over these lakes and retracked them to have qualified water level for each lake. Guo et al. (2009) did waveform retracking using Topex/Poseidon data over Hulun lake in the North of China. They indicated that waveform retracking techniques act quite well in monitoring lake level and seasonal variations. In this study the maximum and minimum RMS with respect to the in-situ gauge data are about 25 cm and 10 cm for sub-waveforms retracked by the threshold algorithm.

Lee et al. (2011) processed RA2 L2 data of Envisat to determine water level of lakes Qinghai and Ngoring in China and lake Athabasca in Canada using on-board tracker and retrackers. Their results indicate that ice-1 retracker provides water level variation with a minimum RMS of 12 cm with respect to the in-situ gauge data for lake Athabasca. Over an ice-covered lake like Qinghai, Tseng et al. (2013) arrived at an RMS of less than 10 cm compared with in-situ gauge time series.

Jain et al. (2015) investigated sea surface height changes in the Arctic region based on CryoSat-2 SAR waveform retracking. They retracked only the first detected sub-waveform with empirical retracking algorithms in summer and winter times. All retrackers have almost the same performance for summer and winter times. They obtained a minimum RMS of 3 cm for estimated sea surface anomaly using Offset Center Of Gravity (OCOG) retracker. A recent study of the CryoSat-2 mission (SAR mode) over Skanderborg Sø, Mossø, and Arresø (Denmark), Okeechobee (North America), and Vänern (Sweden) lakes is showing a very good performance for SAR mode of this mission (Nielsen et al., 2015). They followed Jain et al. (2015) methodology to extract the sub-waveform and used a mixture of Gaussian and Cauchy distributions to model water level from each single pass. In that they combined the modeled water level of each pass to compare with in-situ gauge data. They arrived at a few centimeters of RMS in the comparison process.

In (Kleinherenbrink et al., 2014) the position of the retracked gate was estimated from cross-correlation between an observed waveform of CryoSat-2 SARIn mode and a generic simulated waveform. In that study, water level estimated from CryoSat-2 SARIn mode was validated against Jason-2 derived water level with an RMS of 30 cm for Nasser lake in Egypt. Kleinherenbrink et al. (2015) used the same method as Kleinherenbrink et al. (2014) to retrack the SARIn waveforms of CryoSat-2 over 125 lakes on the Tibetan Plateau and Tian Shan. They compared retracked water level from CryoSat-2 with Jason-2 derived water level over two of these lakes: Langa Co and Bosten lake. They found 55 cm and 26 cm RMS for water level of these lakes respectively. Table 1.1 provides an overview (incomplete) of studies on satellite altimetry for water level monitoring in terms of RMS with respect to in-situ gauge data for a number of lakes.

During the past years satellites have also been used to study water level variations of rivers. The Ob river (in Russia) water level variations was studied by Kouraev et al. (2004) during

Table 1.1: *Comparison of satellite altimetry derived water level with in-situ gauge data for different lakes*

Lake	Country	Area (km^2)	Time frame	RMS (cm)	Reference
Argentino	Argentina	1466	1992–2011	22	Crétaux et al. (2016)
Athabasca	Canada	7900	1992–2009	28	Ričko et al. (2012)
Aydarkul	Uzbekistan	3000	2002–2010	12	Crétaux et al. (2016)
Woods	USA, Canada	4300	1992–2011	27	Ričko et al. (2012)
Baikal	Russia	31500	1992–2009	11	Crétaux et al. (2016)
Erie	USA, Canada	25800	1992–2011	10	Ričko et al. (2012)
Guri	Bolivia	3500	2002–2010	82	Ričko et al. (2012)
General Carrera	Argentina	1800	2002–2010	22	Ričko et al. (2012)
Huron	USA	59500	1992–2011	8	Crétaux et al. (2016)
Qinghai	China	4300	2003–2010	10	Tseng et al. (2013)
Issykkul	Kyrgyzstan	6000	2002–2014	3	Crétaux et al. (2016)
Athabasca	Canada	7850	2002–2008	12	Lee et al. (2011)
Khanka	China, Russia	4400	2000–2010	13	Crétaux et al. (2016)
Hulun	China	2340	1993–2005	10–25	Guo et al. (2009)
Ladoga	Russia	18000	1992–2010	8	Crétaux et al. (2016)
Great	USA, Canada	244000	1992–1994	4	Morris and Gill (1994)
Mead	USA	350	2001–2010	64	Crétaux et al. (2016)
Michigan	USA	58000	1992–2011	11	Ričko et al. (2012)
Onega	Russia	18200	1992–2010	15	Crétaux et al. (2016)
Ontario	USA, Canada	19000	1992–2011	6	Ričko et al. (2012)
Powell	USA	400	1992–2010	85	Crétaux et al. (2016)
Superior	USA, Canada	82200	1992–2011	6	Ričko et al. (2012)
Tana	Ethiopia	3000	1992–2006	17	Crétaux et al. (2016)
Chad	Chad, Niger, Nigeria	1500	1992–2008	28	Ričko et al. (2012)
Titicaca	Peru, Bolivia	7800	2000–2005	7	Crétaux et al. (2016)
Volta	Ghana	8500	1999–2010	53	Ričko et al. (2012)
Oahe	USA	700	2002–2010	45	Crétaux et al. (2016)
Urmia	Iran	2286[1]	2002–2011	18	Roohi (2015)
Bratsk	Russia	3100	1992–2009	41	Crétaux et al. (2016)

1- Surface area in 2015

open water and ice covered periods from Topex/Poseidon mission's GDR data. In that study an RMS of 23–40 cm was achieved for the open water period with respect to in-situ gauge data, and during the ice covered period 2–3 m of RMS was estimated. Frappart et al. (2006) analyzed the GDR data of Envisat over the Amazon river based on the on-board retrackers. They found that the ice-1 retracker with an RMS of 30 cm with respect to in-situ gauge data provides the most accurate water level for the river. The Mekong river was studied by Birkinshaw et al. (2010) based on GDR data of Envisat and ERS-2. They arrived at 44–65 cm of RMS for Envisat and an RMS of 46–76 cm for ERS-2 missions compared with in-situ gauge data. Michailovsky et al. (2012) analyzed Envisat SGDR data to derive water level variation of Zambezi river in Africa. They obtained RMS of 32–72 cm for water level of the river with respect to in-situ gauge data. Dubey et al. (2014) estimated 45–95 cm of RMS for Brahmaputra river (in the south-east of Asia) water level based on GDR data of Envisat mission with respect to in-situ gauge data during both monsoon and non-monsoon seasons. Maillard et al. (2015) analyzed GDR data of Envisat and SARAL missions over different segments of São Francisco river in Brazil to determine water level variations. They defined different models for water level of the river at cross section locations (intersection of the river and satellite ground tracks) based on the river center line and the river bank positions. They validated the modeled water level time series against available in-situ gauge data and arrived at 30–60 cm RMS for the water level. A recent study over the Ganges and Brahmaputra rivers has been done by Villadsen et al. (2015). They retracked waveforms of CryoSat-2 mission for all measurement modes over different sections of these rivers. They retracked only the first peak (the first sub-waveform) in a given waveform with the threshold retracker to retrieve water level of the rivers. They validated the CryoSat-2 results against water level derived from Envisat ice-1 on-board retracker in terms of annual signal and amplitude. A 10 cm difference and 2.7 days delay were estimated in their study for the amplitude and phase respectively. GDR data of Envisat mission were analyzed by Sulistioadi et al. (2015) over the Mahakam and Karang Mumus rivers in Indonesia. They compared water level time series of the rivers derived from the Envisat on-board retrackers with available in-situ gauge data and obtained an RMS of 68 cm. A number of rivers were studied in (Tourian et al., 2016) from a combination of different satellite altimetry missions. They arrived an RMS of 80 cm in the validation of satellite results against in-situ gauge data.

Many of these studies, over inland water bodies, used full-waveform or sub-waveform retracking. In sub-waveform retracking they only retracked the first detected sub-waveforms in a given waveform and neglected the remaining part of the waveform. The remaining part of the waveform can contain useful and valuable information about the reflecting surface. As will be shown in chapter 3 the waveforms can be highly corrupted and include a number of peaks. Therefore it is better to find all of the meaningful sub-waveforms in a given waveform and to retrack them. In our study we did full- and sub-waveform retracking over different inland water bodies with different shapes and sizes. In the sub-waveform retracking we considered all possible sub-waveforms in a given waveform in the retracking process. This is the main difference between our study and previous retracking studies (mentioned above) over inland water bodies.

1.1 Objectives

Since there is no satellite altimetry mission dedicated only for monitoring inland water bodies we used a number of altimeters to study water level variations. Moreover for a given altimeter

there is no standard retracking algorithm to retrack the waveforms over all inland water bodies. Therefore in this thesis we analyze data of different altimetry missions based on different full- and sub-waveform retracking algorithms to:

- analyze the performance of the full and sub-waveform retracking based on different retracking algorithms,
- select the optimized sub-waveform for the retracking,
- analyze the performance of different retracking algorithms,
- select the best retracking scenario to derive water level variations,
- increase the number of valid observations,
- increase the quality of water level determination,
- assess the monitoring ability of different altimetry missions,

for a given inland water body.

1.2 Outline of this thesis

We employ different physical retrackers, e.g. β-parameter and SAMOSA3, and empirical retrackers, e.g. OCOG and threshold, to retrack the full- and sub-waveforms. We perform different retracking scenarios to define water level variations with an accuracy better than what is derived from the on-board trackers and on-board retrackers. We compare different retracking scenarios and select the best retracking scenario for each object.

In the second chapter we introduce the principle of satellite radar altimetry for water level measurement. In that chapter we also discuss different types of altimeters and how the waveform is constructed. Moreover in chapter 2, we describe challenges in using satellite altimetry for monitoring inland water bodies. In the third chapter we explain waveform retracking and all of the retracking algorithms that we use in our study in terms of theory and mathematics. The area of study and the data sets are described in chapter four. Our methodology will be described in chapter 4. We process altimetry data with our methodology based on the on-board retrackers and post-processing the waveforms in chapter 5 to determine water level variation of the study areas. In that chapter the water level derived from different retracking scenarios are validated against in-situ gauge data to find the best retracking scenario for each object. Chapter 6 discusses the numerical results of chapter 5. It also includes the summary and conclusion of the thesis.

Chapter 2

Satellite altimetry

2.1 Altimeter measurement principle

A radar altimeter mounted on a satellite sends electromagnetic pulses with a known power and frequency to the Earth surface. One part of these signals reflects at the surface and is received by the altimeter. The radar system measures the time τ for the pulse to travel round trip between the satellite and the Earth surface and back. Figure 2.1 shows the basic principle of range measurements between satellite and water surface. The round trip travel time for the range is:

$$\tau = 2\frac{R}{c} \ , \tag{2.1}$$

in which c is speed of light. Then the range from the satellite to the surface is determined from:

$$R = \frac{1}{2}c\tau \ . \tag{2.2}$$

R is a raw range that needs to be corrected:

$$R = c\frac{\tau}{2} + \sum_{\mathrm{i}} \Delta R_{\mathrm{i}} \ , \tag{2.3}$$

in which ΔR_{i} are the range corrections (Fu and Cazenave, 2001) including the following items:

- Troposphere (Dry and wet)
  The lower part of the atmosphere, less than approximately 100 km above the Earth surface, is called neutral atmosphere, i.e. non-ionized atmosphere (Saastamoinen, 1972). The delay in the travel time of electromagnetic pulses passing through this part of the atmosphere is a function of dry and water vapor pressure as well as of the temperature (Hopfield, 1971). According to Dejong (1991) 99.9% of all atmospheric mass is included in the lower part, up to 50 km, of the neutral atmosphere. The delay experienced by a radar pulse through this part of the atmosphere is called tropospheric (dry and wet) delay, because the troposphere (the lowest part of neutral atmosphere) accounts for 80% of the total delay (Hopfield, 1971). The tropospheric delay is the largest error source in satellite altimetry measurements. The average range correction due to this delay varies from 1.7 m to 2.5 m. About 80% of the correction depends on the dry atmosphere and 20% is due to the water vapor of the troposphere, wet troposphere (Kruizinga, 1997). The variations in the composition of dry atmosphere with respect to height (Smith and Weintraub,

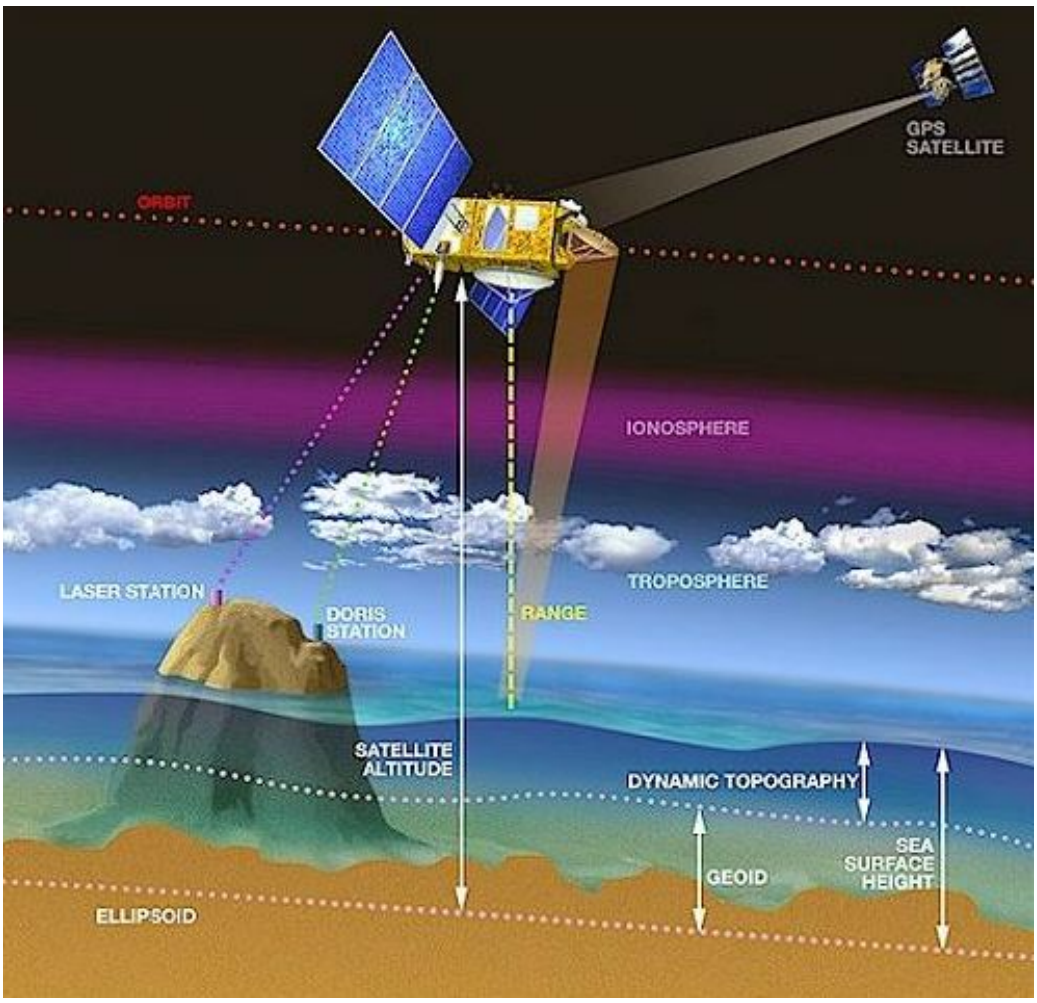

Figure 2.1: *Basic measurement principle of the satellite radar altimeter to measure the sea surface height (ESA and CNES, 2016)*

1953) are small. The water vapor with a smaller contribution (in the tropospheric delay) varies widely with both height and latitude. The dry and wet troposphere corrections depend on the knowledge of atmosphere pressure and temperature observations which are provided by a microwave radiometer carried on-board most of altimeter satellites, e.g MWR on-board Envisat. For an altimeter without microwave radiometer the pressure and temperature are provided by atmospheric models like European Center for Medium-range Weather Forecasts (ECMWF) (Fernandes et al., 2014). More information about the tropospheric delay in terms of theory and mathematics can be found in literature such as (Hopfield, 1971) and (Saastamoinen, 1972).

- Ionosphere
  The ionosphere is the ionized part of the atmosphere, ranging from 100 to 1000 km above the Earth surface (Hopfield, 1971). The ionospheric delay depends on the electromagnetic frequency. Due to the presence of free electrons in the ionosphere, the radar pulse propagation is delayed. The impact of the ionosphere on the radar pulse propagation is characterized by the Total Electron Content (TEC). The TEC is accounted in a cylinder column with a cross sectional area of 1 m, along the path of the radar pulse between the satellite and water surface. It varies highly in time and space. The ionospheric correction is a function of frequency and computed from combining the dual-frequency measurements of the radar altimeter, e.g. for Jason-1/2 and Topex from Ku and C bands (Seeber, 2003; Bronner et al., 2013). For a single-frequency altimeter, e.g. SIRAL on-board CryoSat-2 the ionosphere correction is provided from models which are calculated from double-frequency altimeters. This correction has a typical range of 6 to 12 cm (ESA and MSSL-UCL, 2013). Mathematical equations used to determine the correction can be found in (Seeber, 2003).

- Pole tide
  The pole tide, a tide-like motion, is a response of both the solid Earth and the ocean to the centrifugal potential. It is generated by a small perturbation in the Earth rotation axis. The perturbation occurs at a period of 433 days, called Chandler wobble (Wahr, 1985). Modeling the pole tide requires knowledge of Love numbers and time series of the Earth rotation axis. More information about the Love numbers and how they are computed can be found in (Longman, 1966). The displacement due to the pole tide typically varies from 1 to 2 cm per year in the radial direction (Wahr, 1985) and can be measured by space measurement techniques, e.g. Very Long Baseline Interferometry (VLBI) and Satellite Laser Range (SLR) (Haas and Schuh, 1996; Wu et al., 2001).

- Solid earth tide
  The solid Earth responds to external gravitational forces from, e.g. sun and moon, like oceans do. In the presence of these forces the Earth can be considered as an equilibrium surface. More information about tide forces are in (Scherneck, 1991; Cartwright and Tayler, 1971). Changing in the height due to these forces depends on the latitude and tide frequencies that are estimated based on the Love numbers (Wahr, 1985). The solid Earth tide correction removes the height changes induced by tidal forces from the Sun and Moon. Typical value of this correction ranges from -30 to $+30$ cm (ESA and MSSL-UCL, 2013).

- Saturation
  Waveform saturation occurs when the power in the reflected pulse varies more than a

gain function of radar's receiver. It causes distortion in the waveform and mostly happens in high-amplitude waveforms, reflected back from flat or bright surfaces, e.g. ponds on ice sheet and leads in sea ice areas. Saturation correction varies from a few to several centimeters (Brenner et al., 2003) and it is more usual in laser altimeters, e.g. GLAS/ICESat. This correction is described in more detail in chapter 4.

- Instrumental errors
  Range measurements from an altimeter need to be corrected due to instrumental effects. According to Callahan et al. (1994) the instrumental range correction can be written as:

$$R_{\text{inst}} = R_{\text{cm}} + R_{\text{track}} + R_{\text{osc}} + R_{\text{Dopp}} + R_{\text{intcal}} \ , \tag{2.4}$$

  in which R_{cm} is the center of mass correction due to the separation of the radar's antenna from the satellite center of mass, because the satellite orbit height is referenced to this point. The largest instrumental error arises from mispointing angle of the antenna. R_{track} compensates this error (Chelton et al., 1989). The reference Ultra Stable Oscillator (USO), used to measure the travel time of the radar pulse, has an offset in frequency which causes an incorrect range. The offset is corrected by using the oscillator correction R_{osc} (Callahan et al., 1994). An altimeter measures time, by counting the number of cycles of an oscillator. Any error in knowledge of the oscillator frequency therefore results in an error in the estimated two-way travel time. The error is corrected by R_{Dopp}. Most altimeters perform an internal calibration of the electronic system. The delay in the electronic system can vary with time and environmental conditions (Chelton et al., 1989). The internal calibration R_{intcal} is applied in the altimeter range measurements.

These corrections are provided in each altimetry database that must be applied to range measurements over inland water bodies. For ocean or coastal altimetry applications further corrections, e.g. ocean tide and sea state bias, are necessary.
Tables 2.1 and 2.4 represent a part of orbital geometry and radar characteristics of a number of satellite radar altimetry missions.

2.2 Spatial and temporal resolution

Depending on the mission's purpose an altimeter satellite is usually placed in a fixed repeat orbit. A careful repeat orbit design plays an important role in sampling the water bodies from space. If the satellite mission focuses on inland hydrological applications, it must be able to monitor water bodies such as lakes and rivers with a sufficient spatial and temporal resolution.

A repeat orbit mode β/α occurs if the satellite performs β revolutions with respect to its ascending node in α nodal days. A nodal day is the time between two consecutive passages of a fixed earth meridian (Greenwich) over the satellite ascending node. Due to nodal precession it is not exactly equal to a sidereal day.

The repeat cycle duration governs the temporal resolution. Table 2.2 represents the temporal resolution for different altimetry missions. According to this table, The Topex-Jason family with 10 days repeat cycle, seems to be the best mission in terms of temporal resolution. This mission provides, during a short time, a global coverage but its spatial resolution is not sufficient to observe many inland water bodies. Therefore, for altimetry missions, only time resolution is not

Table 2.1: *Satellite mission and operating characteristics of altimeters (AVISO, 2016b; NASA, 2016; Vignudelli et al., 2011)*

Altimeter	Launch	End	H (km)	Inclination	Band	Frequency (GHz)	Wavelength (cm)
Seasat	26 Jun 1978	Oct 1978	800	108.0°	Ku	13.56	2.21
Geosat	12 Mar 1985	Jan 1990	800	108.0°	Ku	13.50	2.22
ERS-1	17 Jul 1991	Mar 2000	784	98.0°	Ku	13.80	2.20
Topex	10 Aug 1992	Jan 2006	1336	66.0°	Ku C	13.60 5.30	2.20 5.65
Poseidon	10 Aug 1992	Jan 2006	1336	66.0°	Ku	13.65	2.20
ERS-2	21 Apr 1995	Sep 2011	784	98.0°	Ku	13.80	2.20
GFO	10 Feb 1998	Sep 2008	800	108.0°	Ku	13.50	2.22
Jason-1	7 Dec 2001	Jul 2013	1336	66.0°	Ku C	13.60 5.30	2.20 5.65
Envisat	1 Mar 2002	May 2012	784	98.0°	Ku S	13.60 3.20	2.20 9.37
ICESat	1 Jan 2003	Aug 2010	600	94.0°	Laser Laser	...[1] ...[2]	...[1] ...[2]
Jason-2	20 Jun 2008	Present	1336	66.0°	Ku C	13.60 5.30	2.20 5.65
CryoSat-2	8 Apr 2010	Present	717	92.0°	Ku	13.60	2.20
HY-2A	15 Aug 2011	Present	971	99.3°	Ku C	13.58 5.25	2.21 5.71
SARAL/Altika	25 Feb 2013	Present	800	98.6°	Ka	35.75	0.84

1-Wavelength 1064 nm (281759.83 GHz frequency), infrared light for surface elevation measurements
2-Wavelength 532 nm (563519.66 GHz frequency), visible green light for vertical distribution of clouds, aerosol and atmospheric measurements

Table 2.2: *Repeat orbit of different missions*

Mission	β	α (day)	Sub-cycle (day)	Inclination
Envisat	501	35	16	98.6°
ICESat	1354	91	33	94.0°
Topex-Jason family	127	10	3	66.0°
CryoSat-2	5344	369	30, 85	92.0°
SARAL/Altika	501	35	16	98.6°
Sentinel-3	385	27	4	98.6°
SWOT	292	21	10	77.6°

Table 2.3: *Ground track separation at the equator* (km)

Mission	After 10 days	After sub-cycle	After full repeat cycle
Envisat	280	174.0	80.0
ICESat	269.3	81.6	29.6
Topex-Jason family	315.5	1051.8	315.5
CryoSat-2	277	92.2, 32.5	7.5
SARAL/Altika	280	174.0	80.0
Sentinel-3	281	703.0	104.0
SWOT	288	288.0	137.0

enough and the spatial resolution must also be considered. The spatial resolution is defined as the inter-ground track spacing along a certain parallel, e.g. at equator. It can be calculated from β as $2\pi R_e/\beta$ (R_e is the Earth's radius), that is the space between two neighboring ascending nodes crossing the equator after an entire repeat cycle α. According to tables 2.3 and 2.2 the best spatial resolution, 7.5 km, belongs to the CryoSat-2 with 369 days repeat cycle but Jason-2, with 315.5 km spatial resolution, has 10 days temporal resolution. The space-time sampling behavior can be explained based on the Heisenberg rule. According to this rule (Reubelt et al., 2010) the better the spatial resolution the worse the temporal resolution and vice versa. So to have an optimized altimetry mission it is necessary to consider both its spatial and temporal sampling behavior.

A sub-cycle is a period of time smaller than the repeat period after which the satellite provides approximately an homogeneous global sampling but sparser than that after a complete cycle. In other words one can define the sub-cycle as the time interval between two same neighboring passes, i.e. two ascending or two descending passes. From table 2.2 one can see that the shortest sub-cycle belongs to Jason-2, that is 3 days. According to table 2.3 during this time it has the largest inter-track spacing (315.5 km at the equator). So it misses most of the inland water bodies to observe. From figure 2.2 (a) one can see, for instance, that Jason-2 during its sub-cycle can not observe Issykul lake (located in Kyrgyzstan). It covers this lake only after completing its repeat cycle (figure 2.2 (b)). Considering the spatial resolution, for hydrological purposes, an orbit with a shorter sub-cycle is preferred because during a short time an altimeter can provide more observations over a given inland water body. For example Envisat measures Issykul lake (figure 2.2 (a)) every 16 days (its sub-cycle) though its repeat cycle is 35 days. Therefore we have more altimetry data over such a lake. Another advantage of an orbit with a shorter sub-

cycle is related to flood management. During the flood seasons we need measurements with a higher temporal resolution to monitor flooded area.

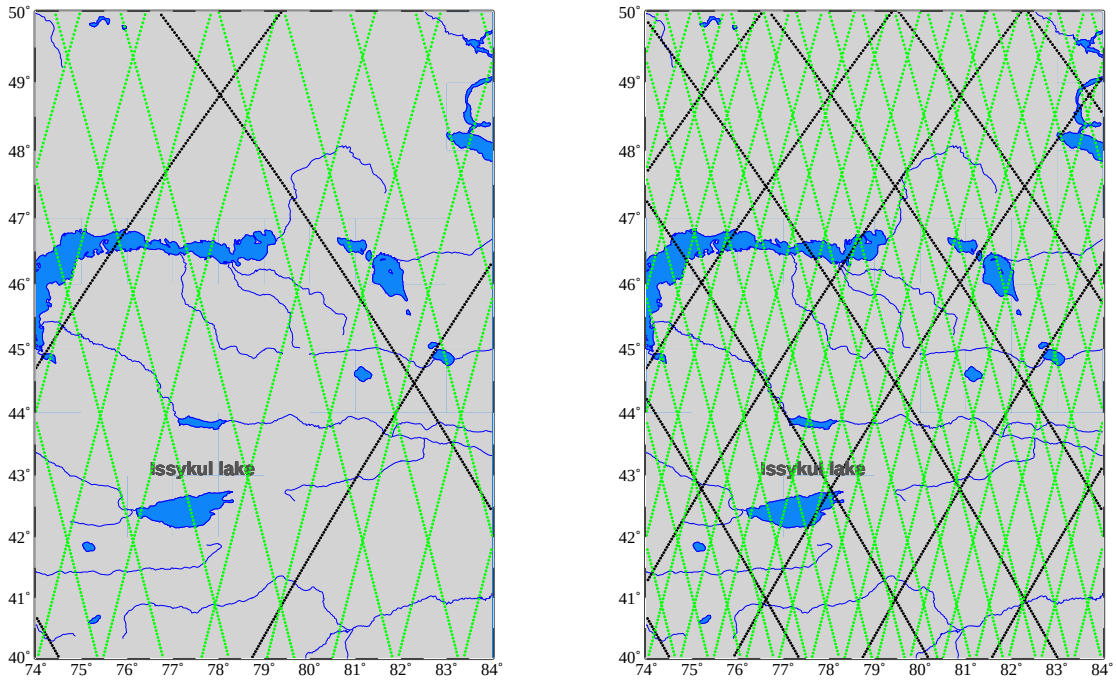

Figure 2.2: *Envisat (green) and Jason-2 (black) coverage over and around Issykul lake, Kyrgyzstan, after their sub-cycles of 16 and 3 days (a) and after their full-cycles of 35 and 10 days (b) respectively*

2.3 Radar equation

If a non-directional antenna (an antenna which emits radiation uniformly in all directions) transmits signals with a power P_t, the amount of received energy at range r is $P_t \frac{1}{4\pi r^2}$ (Rosmorduc et al., 2011). The signals propagate uniformly in all directions at the transmitted power but the power decreases at points far from the antenna. On the other hand only nadir direction is important in satellite altimetry. We need more radiation in this direction to illuminate the water surface beneath the satellite which requires a non-uniform antenna gain pattern. Figure 2.3 represents a non-uniform gain pattern. The ratio of the energy propagated in these directions and the energy that would be propagated if the antenna were not directional is known as antenna gain (Barton, 1988). A transmitting antenna with a gain of 3 dB means that the power received far from the antenna will be 3 dB higher than what would be received from a non-directional antenna with the same input power. In the non-uniform propagation, an antenna gain pattern G causes to transmit more radiation in the nadir direction. So the directional power density increases as $P_t \frac{1}{4\pi r^2} G$. The size and scattering properties of a target inside the antenna footprint known as normalized radar cross-section σ affects the radar signal. So the power intercepted by the target is $P_t \frac{1}{4\pi r^2} G\sigma$. According to Kirchhoff's law the ratio of emissivity and absorptivity is constant (Salisbury et al., 1994). Therefore the reflected power density back at range r is

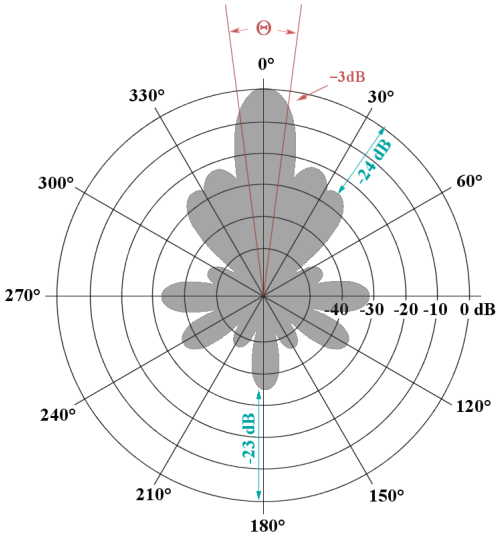

Figure 2.3: *Schematic propagating the radiation (in the polar coordinate system) for a non-uniform propagation (Wolff, 1998)*

$P_t \frac{1}{4\pi r^2} G\sigma \frac{1}{4\pi r^2}$. This is the power intercepted by a radar antenna whose effective area is A_e, so the received power P_r is given by:

$$P_r = \frac{P_t G}{4\pi r^2} \sigma \frac{1}{4\pi r^2} A_e \quad . \tag{2.5}$$

$A_e = A\ K_a$ in which K_a is efficiency. A_e is related to antenna gain by $G = \frac{4\pi A}{\lambda^2} K_a$ (λ is the wavelength and A is the geometrical antenna area). So the radar equation can be written in the more useful form:

$$P_r = \frac{P_t G^2 \lambda^2 \sigma}{(4\pi)^3 r^4} \quad . \tag{2.6}$$

2.4 Backscatter coefficient

One of the fundamental measurements of satellite altimetry is the ratio of the received signal power at the antenna and the transmitted signal power from the antenna. After the signals are transmitted from the radar, they are attenuated by the atmosphere before they arrive at the water surface. A part of the power is scattered back and the rest is absorbed by water. The reflected part is attenuated again by the atmosphere. The backscatter coefficient, called *normalized radar cross section* (Anzenhofer et al., 1999), is quite difficult to estimate and is normally determined by measurements. We suppose that the backscatter coefficient σ is spatially homogeneous over the area inside the antenna footprint. Therefore from the radar equation one can compute the backscatter coefficient:

$$\sigma = \frac{P_r (4\pi)^3 r^4}{P_t G^2 \lambda^2} \quad . \tag{2.7}$$

Table 2.4: *Summary of instrument characteristics of altimeter missions (AVISO, 2016b; NASA, 2016; Vignudelli et al., 2011)*

Altimeter	Band	Antenna beamwidth	PRF (Hz)	Number of waveform gates	Nominal tracking point	Gate width[1] (ns)	Gate width (cm)
Seasat	Ku	1.59 °	1020	60	29.5	3.125	47
Geosat	Ku	2.00 °	1020	60	30.5	3.125	47
ERS-1	Ku	1.30 °	1020	64	32.5	3.030	45
Topex	Ku	1.10 °	4500	128	32.5	3.125	47
	C	2.70 °	1200	128	32.5	3.125	47
Poseidon	Ku	1.10 °	1700	60	29.5	3.125	47
ERS-2	Ku	1.30 °	1020	64	32.5	3.030	45
GFO	Ku	1.60 °	1020	128	32.5	3.125	47
Jason-1	Ku	1.28 °	1800	104	31.0	3.125	47
	C	3.40 °	300	104	31.0	3.125	47
Envisat	Ku	1.29 °	1800	128	46.5	3.125	47
	S	5.50 °	450	64	25.5	6.250	94
ICESat	Laser	0.029 °	40	1000	500	5.000	75
	Laser	0.010 °	40	544	272	5.000	75
Jason-2	Ku	1.26°	1800	104	31.0	3.125	47
	C	3.38°	300	104	31.0	3.125	47
CryoSat-2, LRM	Ku	1.08°, 1.20°	1970	128	63.0	3.125	47
CryoSat-2, SAR	Ku	1.08°,1.20°	18181	128	63.0	1.5625	23
CryoSat-2, SARIn	Ku	1.08°,1.20°	18181	512	255.0	1.5625	23
HY-2A	Ku	41.00°,49.00°	2000	128	32.5	3.125	47
	C	41.00°,49.00°	2000	128	32.5	6.250	94
SARAL/Altika	Ka	1.29°	1800	128	46.5	3.125	47

1: Pulse width

2.5 Area illumination and waveform construction

An altimeter employs a nadir-pointing radar to transmit a short pulse with a duration of a few nanoseconds from the antenna. An altimeter like SIRAL, carried by CryoSat-2, in SAR mode sends a burst of pulses instead of a single pulse. Each burst includes 64 pulses. The shape of the received signal, called waveform, indicates the time evolution of the reflected power as the radar pulse hits the water surface. The waveform is a fundamental measurement to observe geophysical parameters of the Earth surface (Anzenhofer et al., 1999). It provides information about the properties and nature of the reflecting surface such as significant wave height and backscatter coefficient. Figure 2.4 demonstrates how a waveform arises. The radar antenna transmits an electromagnetic or laser pulse that propagates as a spherical wavefront. The wavefront hits the surface at t=t_0, it illuminates one point and a reflected power starts to return to the altimeter. As time goes on the pulse progresses and the wavefront spreads the other points and forms a disc. Within the disc, the backscattered power reaches the radar and builds up rapidly rising part of the waveform (leading edge). The maximum return power corresponds to the occasion of maximum disc area, t=t_1 (Deng, 2003). After t_1 (at t=t_2) the disc transits to an annular ring and the power begins to decay (figure 2.4). The signal reflected back from the ring, generates the next part of the waveform with long decay (trailing edge). The first part of the waveform, before the leading edge, is thermal noise in the radar. In order to reduce the statistical fluctuation and to perform the time tracking as well as to reduce the noise level the returned signals are usually averaged on-board based on the radar instrument characteristic and frequency of the transmitted pulse (ESA and CNES, 2016). For example Envisat sends pulses with Pulse Repetition Frequency (PRF) of 1800 Hz (with an interval of about 50 ms) and every 50 ms the returned signals are averaged over 100 waveforms for Ku band and over 25 waveforms for S band (Benveniste et al., 2002). These waveforms are recorded by on-board altimeter sensor during the time tracking with 128 gates for the Ku band and 64 gates for the S band.

The return waveform mainly includes three parts:

- The thermal noise adds a constant power level to the returned waveform.
- The leading edge contains the returned power from the scattering surface within the footprint of the radar which gives us information about the range and significant wave height.
- The trailing edge contains the returned power from the scattering surface inside the ring.

The averaged returned waveform is a time series of mean returned power, referred to as the Brown model, explained by convolution of three components according to Brown (1977) and Hayne et al. (1994):

$$W(t) = P_{\mathrm{fs}}(t) * Q_{\mathrm{s}}(t) * S_{\mathrm{r}}(t) \ , \tag{2.8}$$

where P_{fs} is the average flat surface response, Q_{s} is the probability distribution density function of specular points in the radar footprint and S_{r} is the radar system point target response. Several consecutive waveforms of a single pass of CryoSat-2 SAR mode over Neagh lake, located in Northern Ireland, are plotted in figure 2.5. Figure 2.6 shows consecutive waveforms of Envisat with different shapes and different power from a single pass over Urmia lake, located in the Northwest of Iran. Consecutive waveforms from a single pass of the GLAS/ICESat mission over Neagh lake with almost constant shape and power are plotted in figure 2.7. From figures 2.5–2.7 one can see that different altimeters and different surfaces have different waveforms in

terms of shape and power, because the components which construct the waveform depend on the radar characteristics and geographical locations of the footprint which vary for different objects and different altimeters.

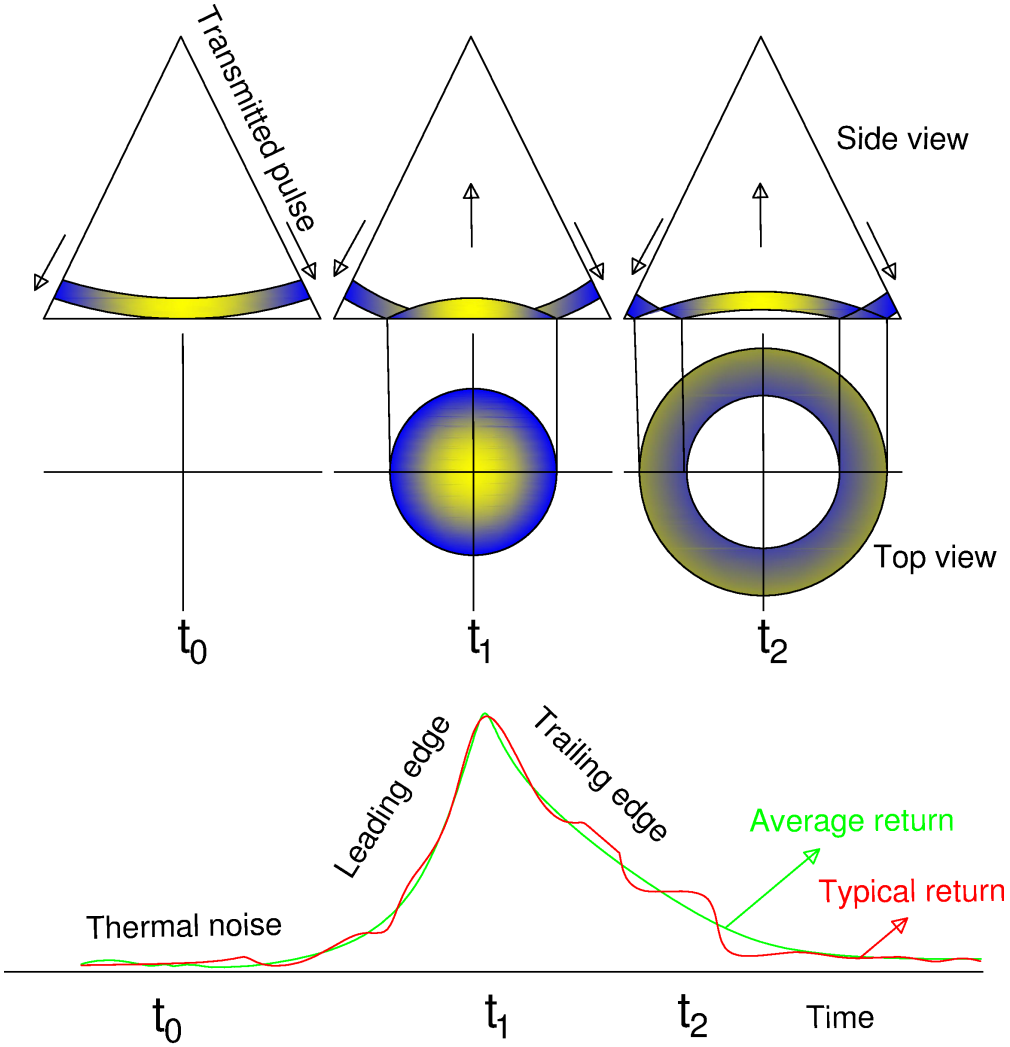

Figure 2.4: *Schematic geometrical description of the interaction of a pulse and scattering surface and build up of a returned waveform over the duration of a pulse, adapted from (Deng, 2003). It should be noticed that t_0, t_1 and t_2 in the waveform correspond to t_0, t_1 and t_2 at the illuminated surface.*

2.6 Pulse- and beam-limited radar altimeters

Radar altimeters can be divided into pulse-limited and beam-limited altimeters. All of the microwave altimeters like Topex/Poseidon, ERS-1, ERS-2, Jason-1, Jason-2, Envisat, SARAL and CryoSat-2 LRM are pulse-limited altimeters in the sense that a transmitted pulse meets the scattering surface over an area that is limited by the width of the transmitted pulse. Laser altimeters like GLAS/ICESat and CryoSat-2 in SAR and SARIn modes (in the along-track direction) are beam-limited altimeters. In this type of altimeters an illuminated area is limited by the beamwidth of the radar. This difference between two types of altimeters leads to different response from the illuminated surface especially where the surface is titled. The geometry of

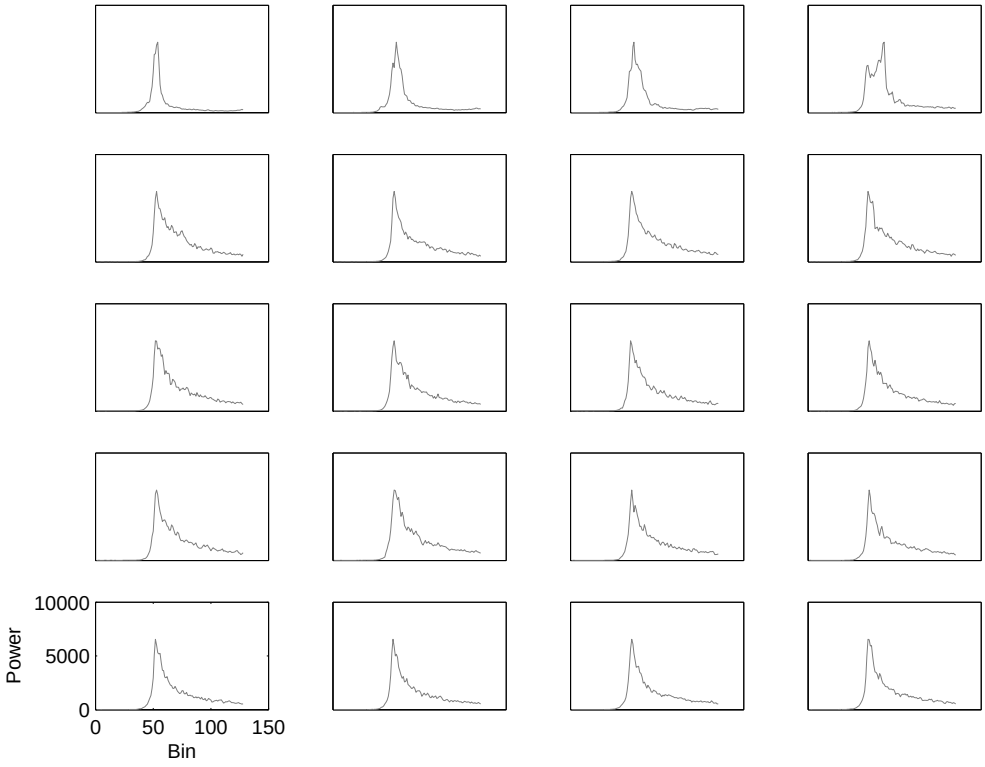

Figure 2.5: *CryoSat-2* SAR *mode waveforms over Neagh lake, Northern Ireland, 21 April 2012*

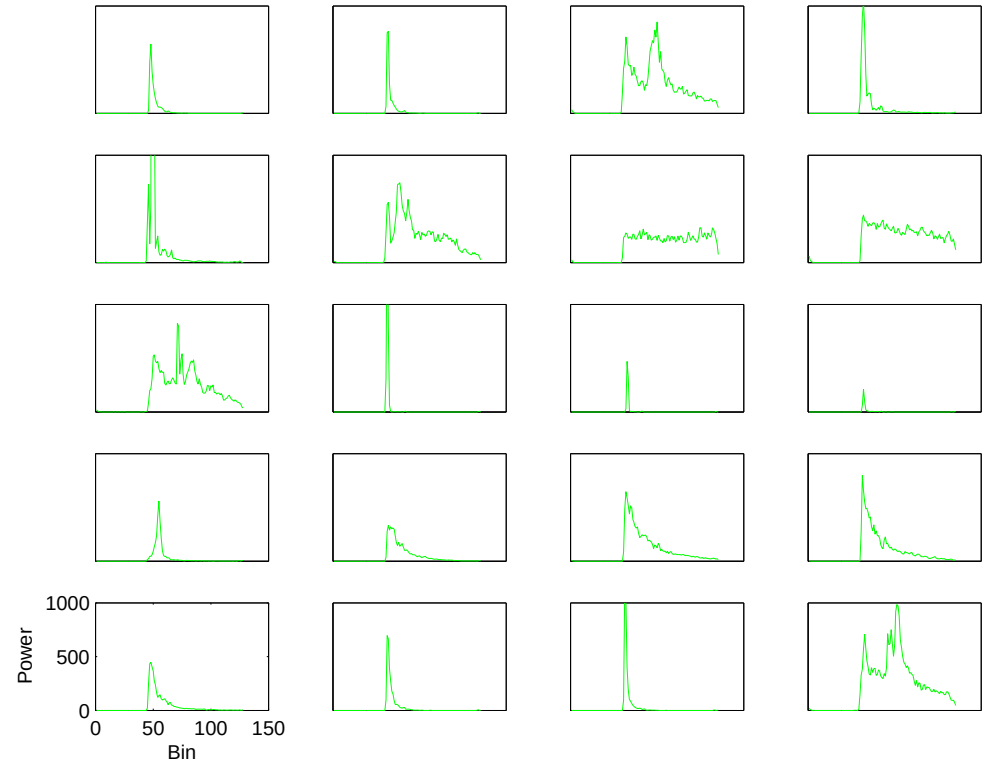

Figure 2.6: *Envisat waveforms over Urmia lake, Iran, 5 January 2010*

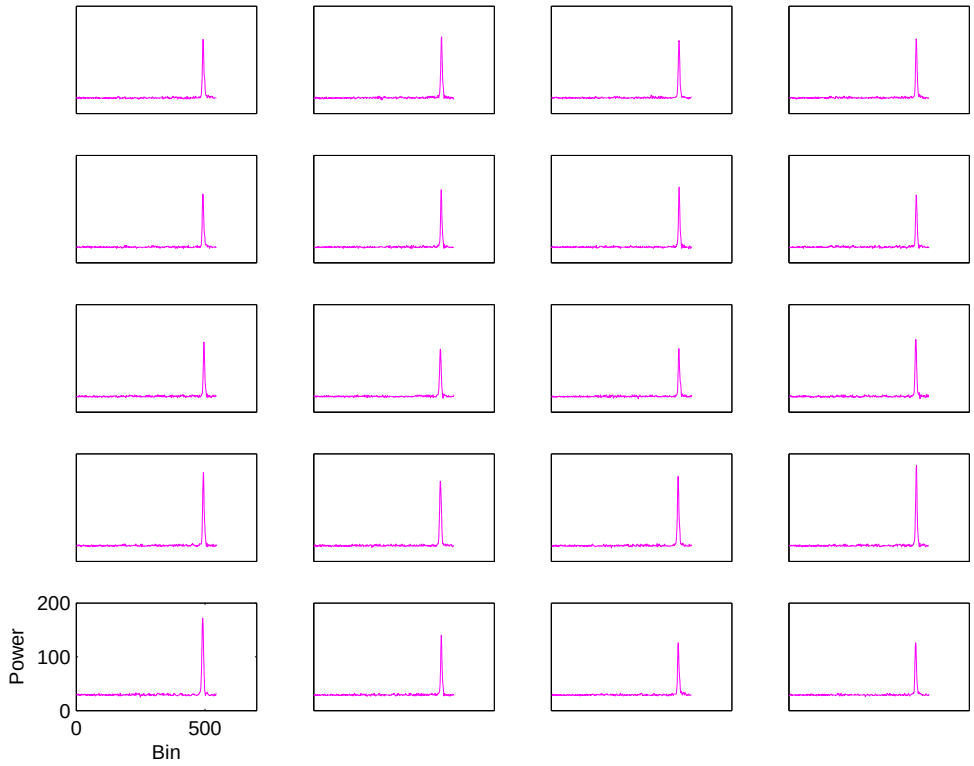

Figure 2.7: *ICESat waveforms over Neagh lake, Northern Ireland, 25 October 2004*

the pulse-limited and the beam-limited altimeters is shown in figure 2.8. The upper panel of this figure represents the geometry over a flat illuminated surface and the lower panel stands for a sloped surface. As one can see from the lower panel the measured range is constant and the illuminated area is variable for the pulse-limited altimeters but for the beam-limited altimeters the measured range is variable and the illuminated area is constant. For the pulse-limited altimeters the slope causes the illuminated surface moves away from the nadir because the illuminated area is always considered around a point on the surface that is the nearest point to the altimeter. The situation shown in figure 2.8 (upper panel) reflects the geometry of satellite altimeters over lakes but the lower panel represent the geometry over sloped ice sheets. Difference between the performance of these two types of altimeters is significant over sloped surface.

The footprint size plays an important role in constructing the returned waveform for both altimeter types (Anzenhofer et al., 1999). According to figure 2.4 the transmitted pulse from the pulse-limited altimeter illuminates the surface beneath the satellite progressively. The illuminated area at any time since t_0 (beginning of transmission) can be calculated as:

$$A_t = \frac{\pi R c R_e}{R + R_e} t \quad . \tag{2.9}$$

The maximum area occurs at t=τ:

$$A = \frac{\pi R c R_e}{R + R_e} \tau \quad , \tag{2.10}$$

in which R is the range (satellite altitude above the nadir point), c the speed of light, τ the pulse width (gate width) and R_e is the Earth's radius (Chelton et al., 1989). As an example for the LRM

mode of CryoSat-2, τ is 3.125 ns and R=750 km, so the pulse-limited illuminated area is about 2.2 km. Equation (2.10) says that for a given range R the effective footprint area of the returned pulse can be controlled by the pulse duration. For the pulse-limited altimeter the shape of the returned pulse is dictated by the length (width) of the pulse (Chelton et al., 1989). The whole area inside the footprint contributes to construct the waveform (figure 2.9, left middle panel).

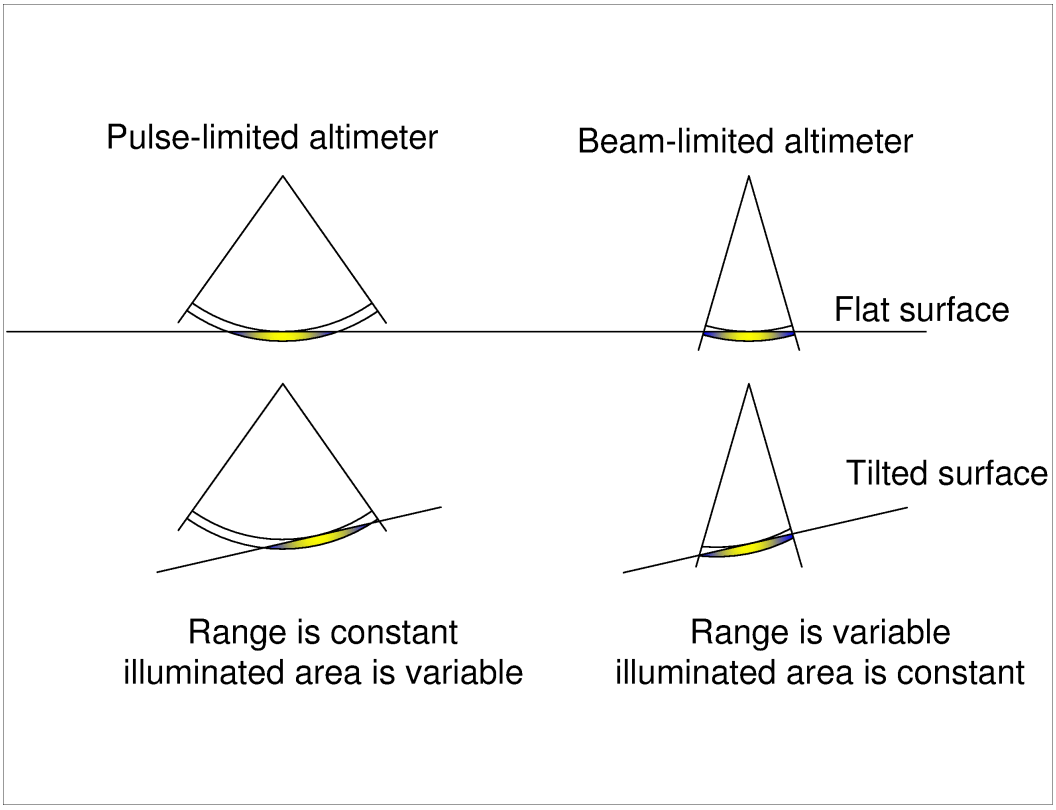

Figure 2.8: *Schematic representative of the pulse-limited and beam-limited illuminating over flat and tilted surfaces, adapted from (Jensen, 1999)*

For the beam-limited altimeter type, the shape of the returned pulse is dictated by the width of the antenna beam angle (Chelton et al., 1989). As it is shown in figure 2.10 the footprint is defined as the whole area on the Earth's surface illuminated by the antenna beam angle which depends mainly on the antenna gain pattern. According to Raney (1998) the accuracy of the range measurement (especially over sloped surface) from the beam-limited altimeter is very sensitive to the antenna pointing error due to the geometry of this type of altimeters (Jensen, 1999). Another disadvantage of the beam-limited altimeters is that their narrow beam width (angle) requires a large antenna diameter according to the following equation:

$$\gamma = k\frac{\lambda}{d} \ , \tag{2.11}$$

in which γ is the antenna beam-width, k is a constant, λ is the wavelength and d is the antenna diameter (Moreira et al., 2013). Using a synthetic aperture it is possible to reduce the limitation of antenna size. According to ESA and MSSL-UCL (2013) the size of the footprint D (shown an

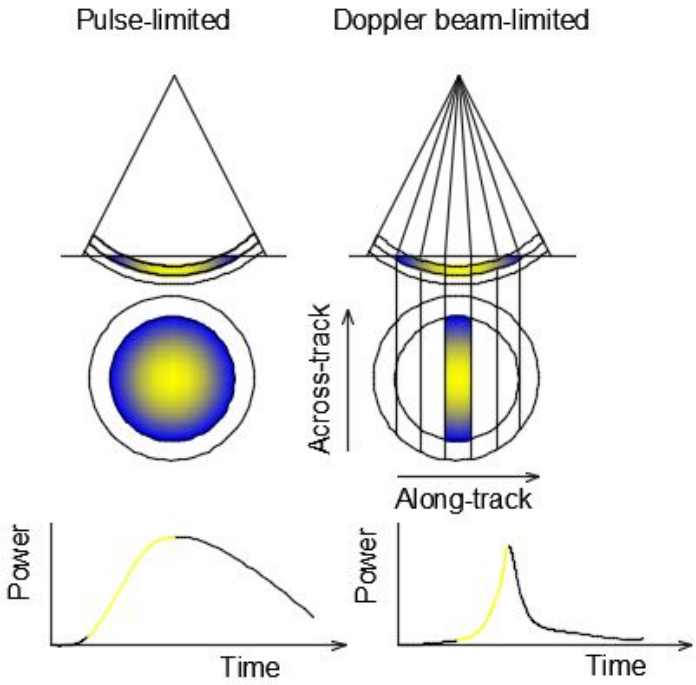

Figure 2.9: *Schematic representative of the pulse-limited and Doppler beam-limited footprints and their waveforms, adapted from (ESA and MSSL-UCL, 2013)*

figure 2.10) of the beam-limited altimeter can be calculated from:

$$D = R\tan(\theta_B + \vartheta/2) - R\tan(\theta_B - \vartheta/2) \ , \tag{2.12}$$

where θ_B is the angle of central beam direction and ϑ is the antenna beam width. Figure 2.10 gives more insight about all parameters of this equation. For an assumed purely beam-limited altimeter with R=750 km, θ_B=0° (for the nadir pointing) and ϑ=1.08° in the along-track direction and θ_B=0.4° and 1.02° the cross-track directions, the footprint size would be 14.13 km in the along track and 15.7 km in the cross track direction. A footprint with this size is not appropriate for monitoring inland water bodies. To overcome the limitations of the beam-limited altimeter synthetic aperture and Doppler processing techniques are used. So this type of altimeters are Doppler beam-limited altimeters.

For instance CryoSat-2 in SAR and SARIn mode is not a simple beam-limited but a Doppler beam-limited altimeter. When it operates in SAR mode the SAR processor uses the Doppler beam formation to discriminate the direction of arrival pulses in the along-track direction (ESA and MSSL-UCL, 2013). Doppler processing leads to defining an illuminated area in both along- and cross-track directions independently. The resolution increases in the along-track to about 300 m (ESA and MSSL-UCL, 2013). In the cross-track direction the illuminated area is similar to what is illuminated by pulse-limited altimeters. During the SARIn mode operation time, an additional antenna is employed to do the cross-track interferometry. In this mode successive bursts of 64 pulses are transmitted by one of the antenna but the 64 returned echos are received by both antenna (Galin et al., 2013). From the phase difference between the received pulses for a given returned burst the surface gradient and elevation error due to the surface slope can be calculated (Galin et al., 2013; Abulaitijiang et al., 2015).

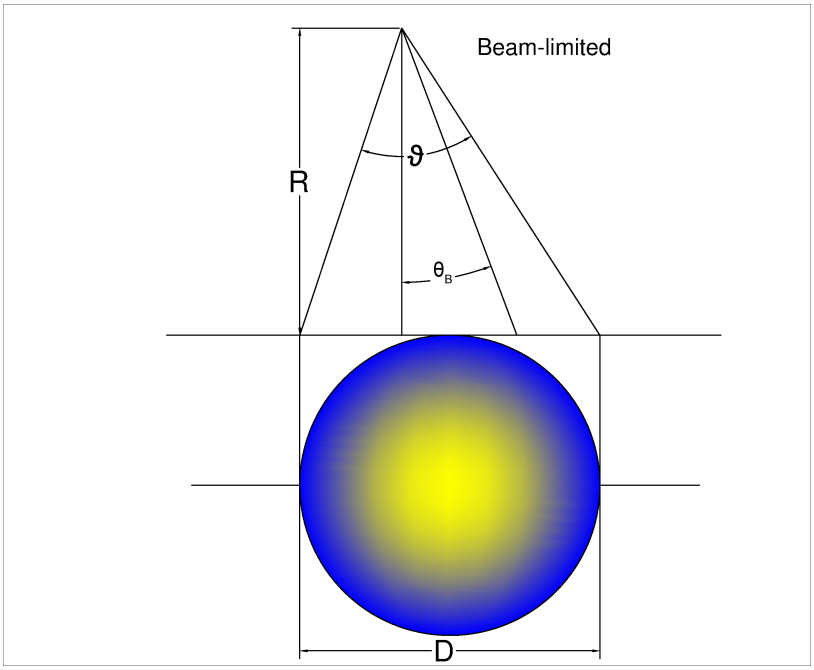

Figure 2.10: *Schematic representative of the beam-limited footprint, adapted from (ESA and MSSL-UCL, 2013)*

As figures 2.9 and 2.11 show, in the along-track direction the footprint is narrow because the Doppler principle allows to sharpen a number of beam-limited widths (for CryoSat-2 64 beams) in along-track direction (ESA and MSSL-UCL, 2013). The along-track footprint size of the Doppler beam-limited altimeters can be calculated from:

$$\Delta x = H \frac{\lambda}{2v} \frac{\text{PRF}}{64} \quad , \tag{2.13}$$

where λ is the wavelength, v satellite velocity and PRF is the pulse repetition frequency (ESA and MSSL-UCL, 2013). In the case of CryoSat-2 if $H = 750\,\text{km}$, $v = 7500\,\text{m}\,\text{s}^{-1}$, PRF=18.181 kHz and $\lambda = 0.0221\,\text{m}$, the along-track footprint size is just 314 m. However the footprint size in the cross-track direction remains the same size as that of the pulse-limited altimeters. Figure 2.12 shows a sequence of 4 illuminating bursts for the pulse- and Doppler beam-limited altimeters which illuminate water surface. In the case of a pulse-limited altimeter there is no overlap between the returned burst of pulses because the time interval between pulses is big enough, about 500 μs resulting in uncorrelated return pulses. But in Doppler beam-limited altimeter the interval between pulses is too short, about 50 μs (ESA and MSSL-UCL, 2013), hence the return pulses are correlated. Considering the whole burst as one and doing inter-burst Doppler processing, each ground location (Doppler cell) is sensed at multiple times. Each Doppler cell on the ground in the illuminated area is sensed until the satellite moves out of the footprint. Therefore it is possible to reduce the noise.

A full Doppler beam-limited altimeter or SAR altimeter is a new generation of satellite altimeter that will use Doppler correction and SAR processing in both along-track and cross-track directions. This type of altimeter provide water surface instead of water level profile. The

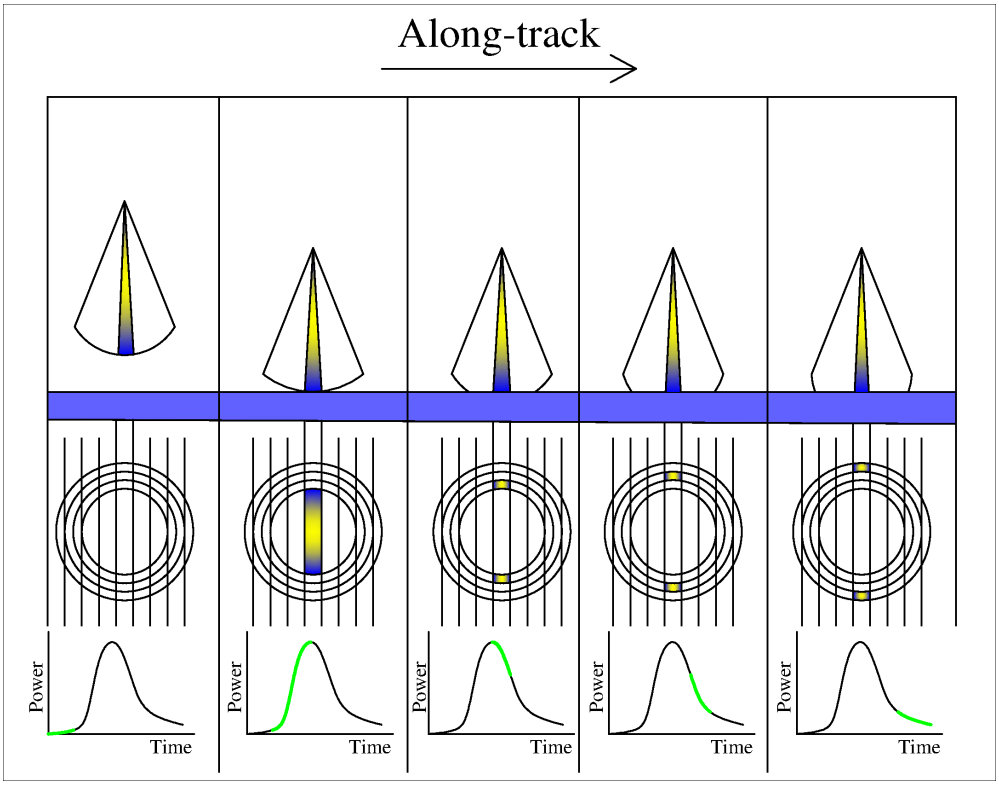

Figure 2.11: *Schematic representative constructing of a* SAR *waveform, adapted from (ESA and MSSL-UCL, 2013)*

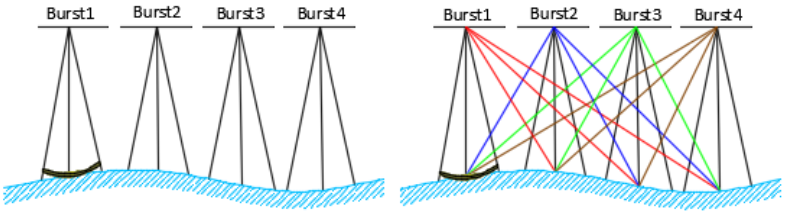

Figure 2.12: *Schematic comparison of illumination from the pulse-limited (left) and Doppler beam-limited (right) altimeters, adapted from (Dinardo and Benveniste, 2013)*

Surface Water and Ocean Topography (SWOT) mission will revolutionize the ability of satellite altimetry to monitoring inland water bodies. It provides a swath width coverage of 120 km in each pass which leads to a very higher spatial resolution. With a 21 days repeat cycle, a 10 days sub-cycle and swath width sampling characteristic, SWOT has a higher temporal resolution too. This mission is discussed in more detail in appendix B.

2.7 Challenges

More than 73% of water used for human activity is supplied by inland water bodies (Biancamaria et al., 2011). Monitoring water level variation of these water bodies with enough spatial and temporal resolution is very important in this respect. During the last two decades satellite altimetry has been extensively used to measure the water level of the inland water bodies. Based on the satellite altimetry principle shown in figure 2.1, for a given inland water body covered with the satellite altimetry measurements, the water level is the difference between the satellite orbit height h_{sat} and the measured range R. So we can write:

$$h_w = h_{sat} - R \ , \tag{2.14}$$

in which h_{sat} is the satellite altitude above the ellipsoid, R corrected range and h_w is the water height above the ellipsoid. As mentioned in the first chapter, several studies were performed over different inland water bodies with different shapes and sizes. A few to several centimeters RMS in water level determination relative to the in-situ gauge data were achieved in those studies. The water level measurements of the inland water bodies are mainly used in hydrological modeling. The quality of water level measurements plays an important role in this modeling. However there are a number of challenges for satellite nadir altimeters over inland water bodies that are described below.

2.7.1 Insufficient spatial and temporal resolution

There are many inland water bodies across the globe that are not sensed by the current altimeters due to limitation of their spatial resolution. For instance there are small lakes on figure 2.2 that are not observed by Envisat and Jason-2 missions. According to (Biancamaria et al., 2010) the current generation of satellite altimetry mission can only monitor 15% of global water volume variations of the inland water bodies. So there is a large gap in the water level data base which is a big obstacle for hydrological modeling. One can combine data from different altimetry missions but still the spatial resolution would not be sufficient to cover inland water bodies.

Temporal resolution is another challenge due to a long repeat cycle for the satellite altimetry orbit. Retrieving the real behavior of the water level variation from an altimeter satellite with a long repeat cycle would be difficult or impossible. For example CryoSat-2 mission can observe many inland water bodies (higher spatial resolution) but its repeat cycle is 369 days (table 2.2). So inter-seasonal or monthly behavior of water level variations may not be detected for many inland water bodies by this mission. Figure 2.13 show CryoSat-2 (SAR mode) samples over a number of lakes in Ireland for 2011. As one can see from this figure CryoSat-2 measures even small lakes, e.g. Mask and Ree lakes, with surface areas of about 80 km^2 and 100 km^2 respectively, which is good in terms of spatial sampling. But there are

only a few samples (poor temporal resolution) per year over these lakes that can not reflect water level variations accurately.

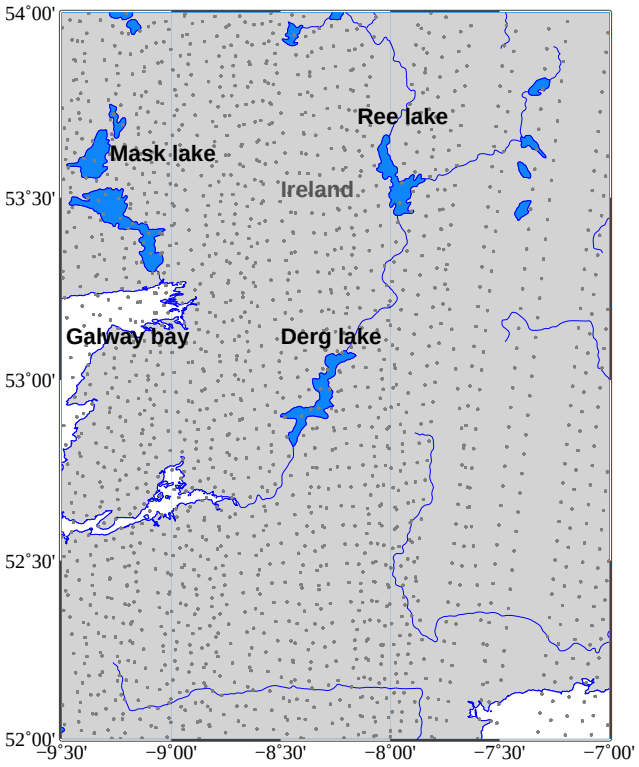

Figure 2.13: *CryoSat-2 SAR mode sampling behavior in 2011*

The GLAS/ICESat sampling behavior is another example that shows the problem of temporal resolution. For a given water body covered by this mission, there are only 3 water level measurements per year, which can not reflect the real variations of water level.

Since the lifetime of each satellite altimetry mission is limited, we do not have a long continuous water level time series (which is necessary for hydrological modeling at regional and global scales) for these water bodies even with a combination of the water level measurements from different altimeters. One can combine measurements from different altimeters to define a longer water level series but there would be a bias between water level from different missions (Tourian et al., 2016).

2.7.2 Waveform contamination

In addition to the temporal and spatial sampling limitations, range measurements over inland water bodies is also a challenge for the current radar altimeters. Due to relatively large footprints for most of altimetry missions, an illuminated surface inside the radar footprint can be inhomogeneous, i.e. include water, vegetation and land. Consequently the radar pulses reflected back from such a surface lead to corrupted waveforms. Therefore the measured ranges would be corrupted as well. Figure 2.14 illustrates the waveform contamination over a given inland water bodies schematically.

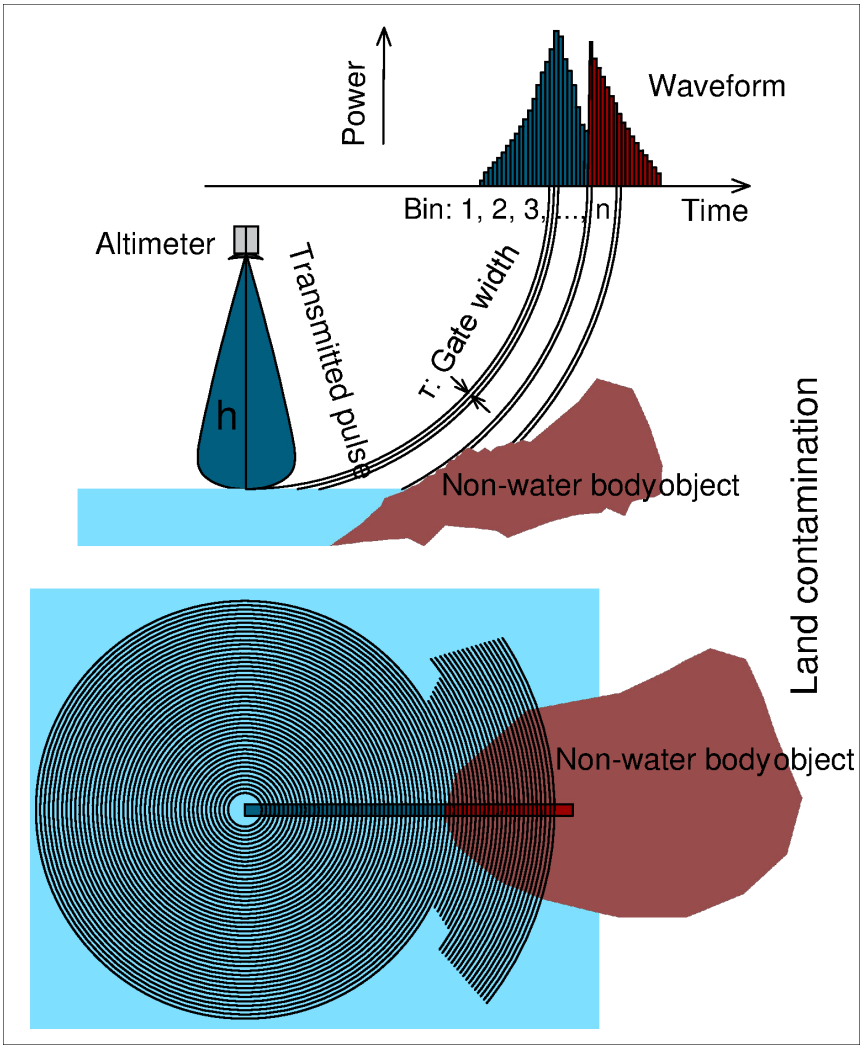

Figure 2.14: *Schematic representation of a transmitted pulse from the altimeter to the water surface of an inland water body (top panel). A top-down view of the pulse limited footprint corresponding to each waveform (lower panel), adapted from Vignudelli et al. (2011).*

As shown in figure 2.14 multiple responses from the illuminated surface inside the radar footprint create corrupted waveforms (multi-peak waveforms).

Waveforms must be retracked to derive accurate ranges and to obtain an accurate water level especially over shallow lakes. Waveform retracking will be explained in chapter 3. Figure 2.15 shows a real example in which the satellite is flying very close to the shoreline of Urmia lake (located in the northwest of Iran) during the descending tracks. Passing very close to the shoreline can result in water level determination as shown in figure 2.16.

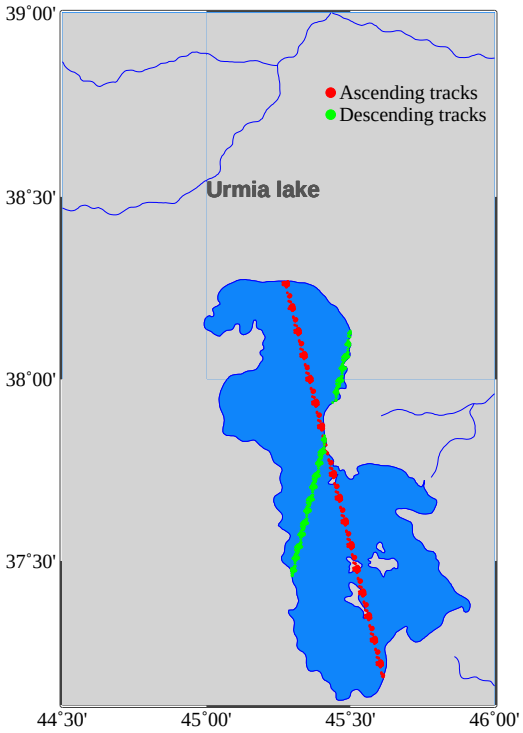

Figure 2.15: *Envisat sub-satellite points over Urmia lake from cycle 6 to cycle 113 (2002–2012)*

Figure 2.16 represents separately water level variations of Urmia lake from ascending and descending tracks of Envisat using on-board range measurements, i.e. without waveform retracking. As it is clear from this figure, the water level of the lake from the descending tracks varies a lot over entire time series especially it is diverged after 2008. Such a time series can not reflect real behavior of the lake water level variations. There is not such an event in the water level of the lake derived from the ascending tracks. So the on-board range measurements can not provide qualified water level variations especially when satellite is flying close to the shoreline, because the waveforms would be contaminated due to complex responses from the land and water surfaces. The on-board ranges are computed based on a nominal bin in the waveforms, e.g. bin 46.5 for RA-2 altimeter carried bay Envisat. But the nominal bin in the contaminated waveforms is not an optimal bin to derive the range. Therefore the ranges are erroneous which decrease the quality of water level determinations (equation (2.14)).

2.7.3 Off-nadir effect

Another limitation for the range measurements over inland water bodies is the effect of off-nadir responses that is common in GDR data. For nadir pointing altimeters it is assumed that the location of the footprint is at nadir of the satellite. However the responses can come back to the radar before and after the satellite passes over the water surface. Since ranges before and after the nadir location are larger than nadir range, water heights follow a quadratic form. According to Santos et al. (2010) the off-nadir effect can be modeled by fitting a degree two polynomial to the successive water height values. It is known as hooking effect in (Schwatke et al., 2015). They used the method of Santos et al. (2010) to correct water level time series of their study areas. Tourian (2012) found off-nadir effect in water level determination of inland

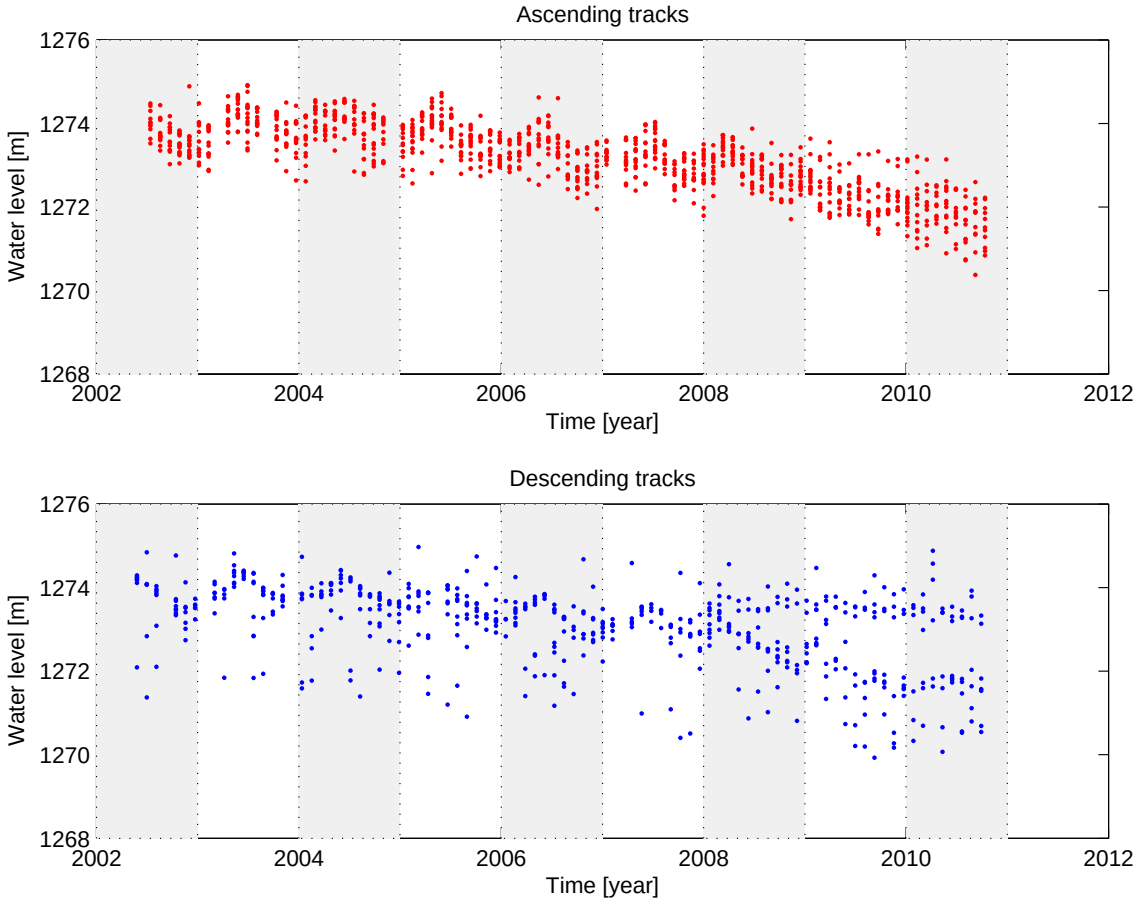

Figure 2.16: *Water level time series of Urmia lake before waveform retracking*

water bodies and used the method of Santos et al. (2010) method to remove the effect. Figure 2.17 represents the geometry of off-nadir correction schematically.

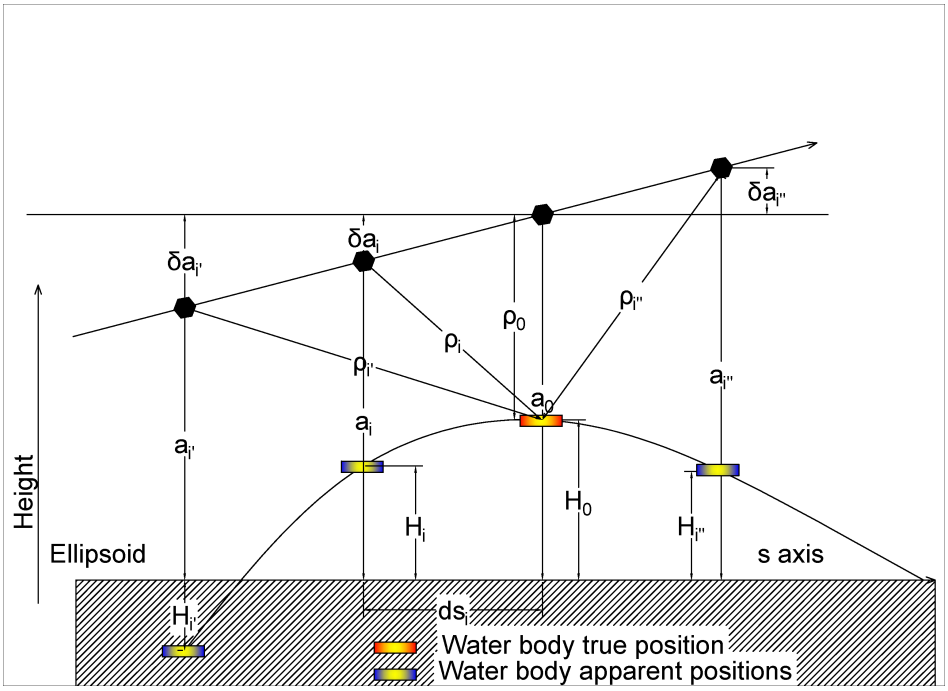

Figure 2.17: *The schematic representative of off-nadir effect on the along-track water height, in this figure a_i, $a_{i'}$ and $a_{i''}$ are the satellite altitude and ρ_0, $\rho_{i'}$ and $\rho_{i''}$ are the slant ranges at the successive times t_i, $t_{i'}$ and $t_{i''}$ respectively. a_0, ρ_0 and H_0 are the satellite altitude, range and water height at nadir respectively, adapted from Santos et al. (2010)*

With all of the mentioned limitations satellite altimetry is still extensively used for water level monitoring of inland water bodies across the world. From equation (2.14) one can say that the more precise satellite orbit height h_{sat}, range R and range corrections the more accurate water level h_w.

POD

The satellite orbit height h_{sat} can be estimated from Precise Orbit Determination (POD). POD deals with accurately determining the position and velocity vectors of an orbiting satellite. There are different approaches of POD such as kinematic, dynamic and reduced dynamic. More information about POD can be found in (Montenbruck et al., 2005; Kang et al., 2006; Bock et al., 2007; Jäggi et al., 2007) and other literature.

Satellite altimeters usually carry a GPS or DORIS (Doppler Orbitography and Radiopositioning Integrated by Satellite) receiver. By post-processing GPS and DORIS measurements, the satellite orbit height h_{sat} can be estimated. DORIS is a French Doppler satellite tracking system developed by Center National d'Etudes Spatial (CNES) for precise orbit determination and positioning. It is on-board most of the satellite altimetry missions, e.g. CryoSat-2, HY-2A, SARAL and Jason-2. The complete DORIS system includes the DORIS on-board package, a network of approximately 60 beacons located around the world and a ground system (Bronner et al., 2013).

More information about DORIS system can be found in Willis and Ries (2005); Willis et al. (2005); Tavernier et al. (2005)

The satellite altitude h_{sat}, estimated from any method, is included in the altimetry database that can simply be used in equation (2.14).

In equation (2.14) we only focus on the range measurements and deal with algorithms and techniques in data processing that provide the smaller error for R to determine the more accurate water level h_w.

From satellite altimetry data one can derive the water level variations from on-board measured ranges or by post-processing on-board measured waveforms (waveform retracking). This issue will be explained in more detail in chapters 4 and 5.

Chapter 3

Waveform retracking

3.1 Why waveform retracking?

In order to keep the returned power well centered in the altimeter tracking window the on-board computer processes the radar echoes that the receiver has just recorded. It adjusts the tracking window and processes all of the returned waveforms for the purpose of recording the pulse's travel time. Statistical computations, e.g. averaging the waveforms, are also performed by the on-board processor. Finally it extracts a range from the averaged waveform. The on-board processor uses a predesignated (nominal) gate in the waveform (for example gate 46.5 for RA-2 on-board the Envisat) as a reference gate in the time tracking process. So the on-board range measurements could be erroneous especially where there are complex responses for the radar pulses, because the predesignated and real gates do not necessarily correspond. Therefore the recorded waveforms need to be retracked to estimate the real gate (retracked gate) and, consequently, to derive an optimized range.

Retracking also leads to improved estimation of parameters such as significant wave height and backscatter coefficient. This technique can increase the number of valid observations, particularly in coastal zones or over inland shallow water bodies (Anzenhofer et al., 1999). Near the lake shoreline or over shallow water, the altimetry waveforms are generally contaminated by responses from non-water surfaces inside the footprint of the radar. This so called land (or environmental) contamination of the waveform is illustrated in figure 2.14. These corrupted waveforms must be analyzed to determine water level variation precisely.

The quality of water level estimation from a given altimeter depends on the type of retracking algorithm. In this chapter we describe the mathematics behind the retracking algorithms that we used in our study. These algorithms include different physical retrackers, such as β-parameters and SAMOSA3, and empirical retrackers, such as OCOG and threshold. The retracked gate is used in the following equation to determine the retracked range correction:

$$\Delta R_{\text{ret}} = (\text{Gate}_{\text{ret}} - \text{Gate}_{\text{nom}})\tau\frac{c}{2} \ , \tag{3.1}$$

where Gate_{ret} is the retracked gate and Gate_{nom} is the nominal tracking gate known from the radar characteristics, e.g. 63 for LRM and SAR modes and 255 for SARIn mode of the SIRAL altimeter carried by CryoSat-2. The gate or bin is the number of samples in a given waveform (column " Number of waveform gates" in table 2.4). The parameter τ is the gate width or pulse width included in table 2.4, e.g. 3.125 ns for LRM and 1.5625 ns for SAR and SARIn modes.

According to equation (2.8) the waveform is a function of three components: statistical characteristics of the illuminated surface inside the footprint, surface responses to the radar pulse and the radar system. So the waveforms vary for different altimeters over different inland water bodies (objects). Even for a given altimeter and a given object they change along-track the satellite ground-track. Figures 3.1–3.3 represent the along-track waveform variations for the longest satellite passes over different lakes.

From figure 3.1 we see that the leading edges are around gate 50 to 55 for the SAR mode of CryoSat-2 mission. However for both LRM and SAR modes the nominal gate is located at gate 63 (ESA and MSSL-UCL, 2013), which emphasizes the need for retracking.

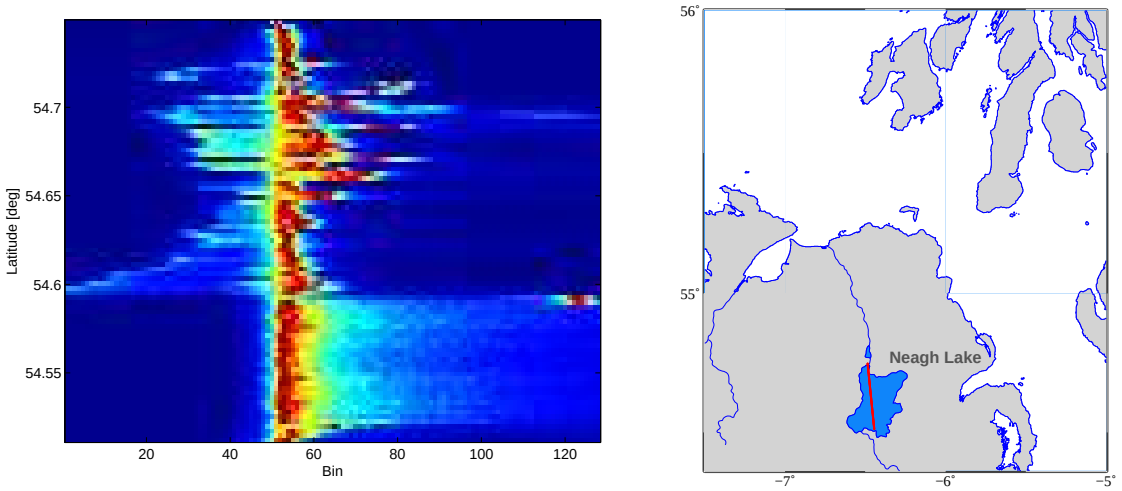

Figure 3.1: *Along-track waveform variations for the longest pass of CryoSat-2* SAR *mode over Neagh lake, Northern Ireland, 20 April 2012*

Figure 3.2 shows waveform variations for CryoSat-2 SARIn mode for a pass over Nasser lake, Egypt. The leading edge positions are almost at gate 150, i.e. the optimal gates for ranging are located close to 150, although the nominal ranging gate is 255 for this measurement mode (ESA and MSSL-UCL, 2013).

Figure 3.3 (left panel) shows that the leading edge positions of CryoSat-2 LRM vary from gate 25 to approximately 70.

It is clear from figures 3.1–3.3 that the nominal gate differs from the optimal retracked gate. The nominal gate does not represent the leading edge, i.e. it does not represent the appropriate height. Therefore waveform retracking is necessary to estimate the optimal gate to correct the on-board range measurements. In the following we describe several algorithms used to retrack waveforms.

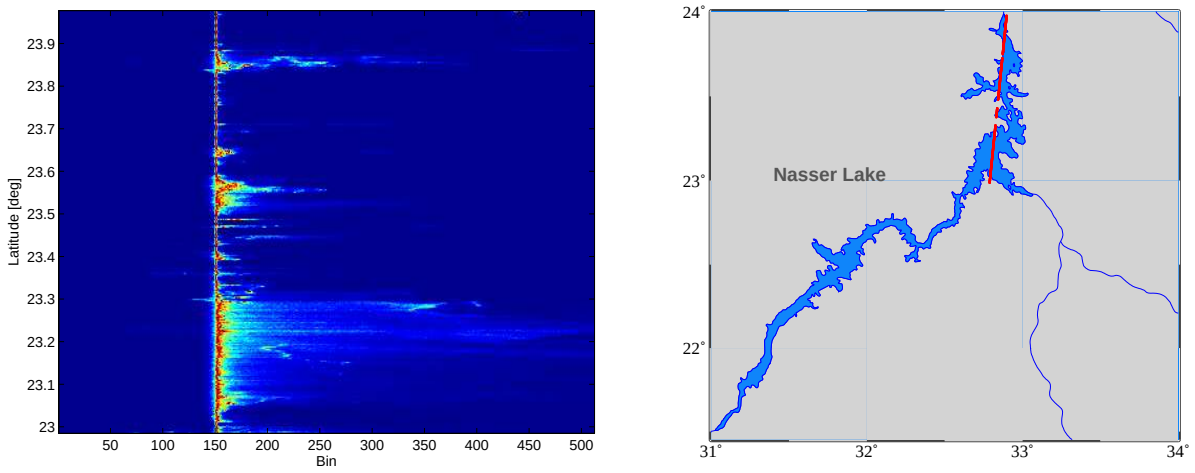

Figure 3.2: *Along-track waveform variations for the longest pass of CryoSat-2 SARIn mode over Nasser lake, Egypt, 13 August 2011*

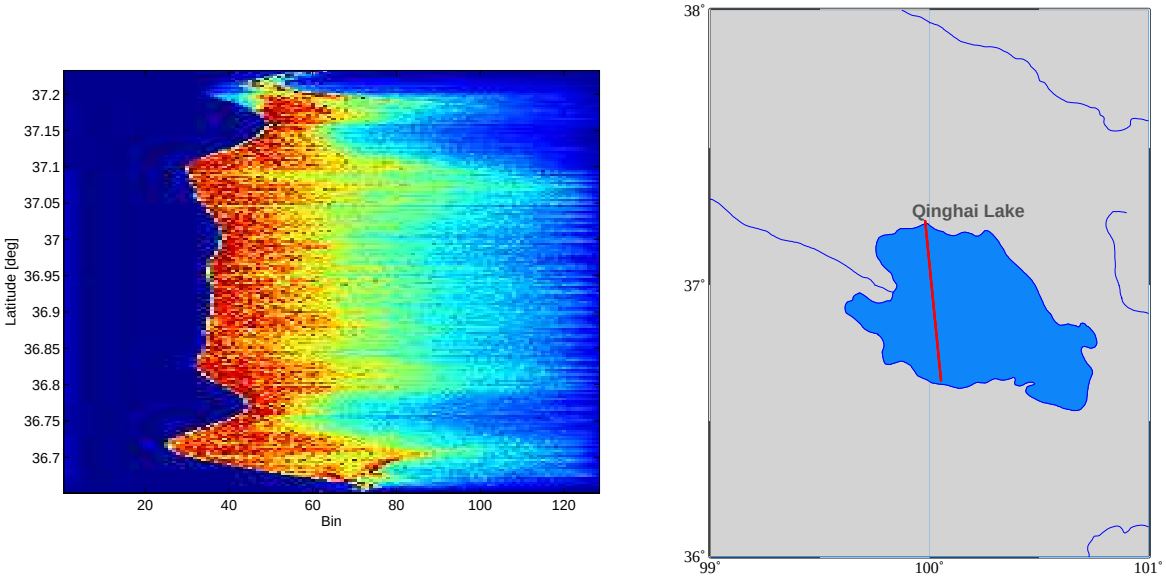

Figure 3.3: *Along-track waveform variations for the longest pass of CryoSat-2* LRM *over Qinghai lake, China, 26 September 2011*

3.2 Empirical waveform retracking algorithms

Retracking means to quantify the leading edge position in the waveform, i.e. finding the optimal gate that represents the height measurement. A number of different waveform retracking algorithms exist to process altimetry waveforms. In this section we explain the retrackers that we used to process the waveforms from different altimetry missions.

3.2.1 Offset Center of Gravity (OCOG)

The offset center of gravity retracking algorithm was developed by Wingham et al. (1986) to provide robust retracking. In this method the gravity center of the waveform is searched based on the power level of gates. Figure 3.4 shows a schematic representation of this retracker. OCOG is a simple waveform retracker based on statistical properties of the waveform.

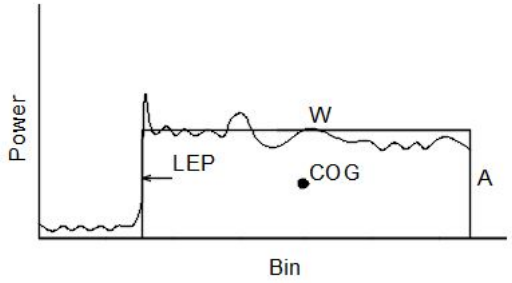

Figure 3.4: *Schematic diagram for* OCOG *retracker, adapted from (Wingham et al., 1986)*

It is very easy for OCOG to retrack waveforms but its precision is generally low because it is independent of physical characteristics of the reflecting surfaces. OCOG is the algorithm behind the ice-1 retracker on-board Envisat. Sometimes it is used to calculate the initial values for other retracker algorithms, e.g. β-parameter and SAMOSA3. Based on the definition of a rectangle about the effective center of gravity (COG) of the waveform, we have the following formulas (Wingham et al., 1986):

$$A = \sqrt{\frac{\sum_{k=1+n_1}^{N-n_2} P^4(k)}{\sum_{k=1+n_1}^{N-n_2} P^2(k)}} \quad , \quad W = \frac{\left(\sum_{k=1+n_1}^{N-n_2} P^2(k)\right)^2}{\sum_{k=1+n_1}^{N-n_2} P^4(k)} \quad , \quad \mathrm{COG} = \frac{\sum_{k=1+n_1}^{N-n_2} kP^2(k)}{\sum_{k=1+n_1}^{N-n_2} P^2(k)} \quad . \tag{3.2}$$

In these equations A is the amplitude, W is the width and COG is the (fractional) bin of the center of gravity of the waveform. $P(k)$ is the waveform power, N is the total number of bins in the waveform, $n_1 = n_2 = 4$ are the number of bins affected by aliasing at the beginning and end of the waveform. Finally, the Leading Edge Position (LEP) is:

$$\mathrm{LEP} = \mathrm{COG} - \frac{W}{2} = \mathrm{Gate}_{\mathrm{ret}} \quad . \tag{3.3}$$

3.2.2 Threshold

The threshold retracking method was developed by Davis (1995) for detecting ice sheet elevation changes. However this retracker is usually used to retrack waveforms over coastal zones and lakes (Davis, 1997). It is sensitive to the surface topography but is simple to implement. In this method of retracking, the dimensions of the rectangle defined by OCOG algorithm are used. The threshold value is usually related to the OCOG amplitude, for instance 10%, 20% or 50% (Guo et al., 2006). The retracked gate is determined by linear interpolation between neighboring gates whose power are smaller and bigger than the threshold value. The threshold method is also statistical and has no physical meaning. For volume scattering when the reflection is caused by inclusion of materials inside the footprint, a threshold level of 10–20% and for surface scattering 50% threshold level is used (Vignudelli et al., 2011). The retracked gate can be computed from the following equations:

$$P_N = \frac{1}{5}\sum_{k}^{5} P_k \ , \ \mathrm{Th} = P_N + q(A - P_N) \ , \ \mathrm{Gate}_{\mathrm{ret}} = (k-1) + \frac{\mathrm{Th} - P_{k-1}}{P_k - P_{k-1}} \ , \tag{3.4}$$

where A is computed from equation (3.2), P_N is thermal noise, q is the threshold value, e.g. 0.2 (20%), k is the first gate whose power exceeds the threshold Th.

3.2.3 Ice-1

The ice-1 retracker is based on the OCOG algorithm, i.e. it uses the rectangle defined in OCOG. When using the ice-1 the retracked gate is estimated from a gate whose power reaches 30% of the OCOG amplitude. So one can categorize the ice-1 as a threshold retracker with a 30% threshold value (Benveniste et al., 2002).

3.2.4 Sea-ice

The sea-ice retracker was developed by Laxon (1994) to retrack the waveforms over sea-ice areas. The maximum power of the waveform is considered as the amplitude of the waveform. The retracked gate is a gate whose power is greater than half of the waveform amplitude (Laxon, 1994). Linear interpolation is used to find this gate.

3.2.5 Ground Segment (GS)

The GS retracking algorithm is used to produce range measurement from the CryoSat-2 mission (Bouzinac, 2012) at L2 and L2i level (data sets will be described in chapter 4). The GS includes the ocean and OCOG retrackers. Over oceans the ocean retracker and over land the OCOG is used. The ocean retracker is described in section 3.3.

3.3 Physical waveform retracking algorithms

3.3.1 β-parameter

The β-parameter retracker was developed by Martin et al. (1983) to retrieve ranges from the Seasat radar altimeter over continental ice sheets. The method uses a relevant parametric function to fit the altimeter waveform, based on the Brown model. The ice altimetry group of National Aeronautics and Space Administration (NASA), Goddard Space Flight Center (GSFC), has developed algorithms based on these function to retrack the ice sheet's waveform (Vignudelli et al., 2011). So this method of retracking is also known as NASA algorithm. It uses either 5 or 9 β-parameters indicated by β_j, $j = 1, 2, ..., 5$ or 9 to fit to single and double ramped waveforms respectively. A double ramped waveform can be considered as a waveform that includes two sub-waveforms (for instance the waveforms shown in figures 3.12 and 3.13). The sub-waveform will be explained in section 3.5. The general model for this retracker reads:

$$y(k) = \beta_1 + \sum_{i=1}^{n} \beta_{2i}(1 + \beta_{5i} Q_i) P\left(\frac{k - \beta_{3i}}{\beta_{4i}}\right) \quad , \tag{3.5}$$

in which:

$$Q = \begin{cases} k - (\beta_{3i} + 0.5\beta_{4i}) & \text{if} \quad k \geq \beta_{3i} + 0.5\beta_{4i} \\ \\ 0 & \text{if} \quad k < \beta_{3i} + 0.5\beta_{4i} \end{cases} \quad , \tag{3.6}$$

$$P(x) = \int_{-\infty}^{x} \frac{1}{\sqrt{2\pi}} \exp\left(\frac{-q^2}{2}\right) dq \quad . \tag{3.7}$$

n=1 or 2 stands for the number of ramps. The other parameters are:

- β_1: the thermal noise level
- β_{2i}: the returned signal amplitude
- β_{3i}: the mid-point on the leading edge (retracked gate)
- β_{4i}: the risetime (the mean of the start and end gates of the leading edge)
- β_{5i}: the slope of the trailing edge

These unknown parameters can be estimated by the least squares method. Since equation (3.5) is non-linear it must be linearized. So we use linear least squares parametric adjustment (LLSPA) in an iterative way to estimate the unknown parameters. Initial values of β_1, β_{2i}, β_{3i} were calculated from the OCOG retracker. An initial value for β_{4i} was calculated from the mean of the approximate start and end gates of the waveform leading edge. Based on the general shape of the waveform trailing edge an initial value for β_{5i} was selected. To do so we looked at a number of waveforms of different arbitrary passes.

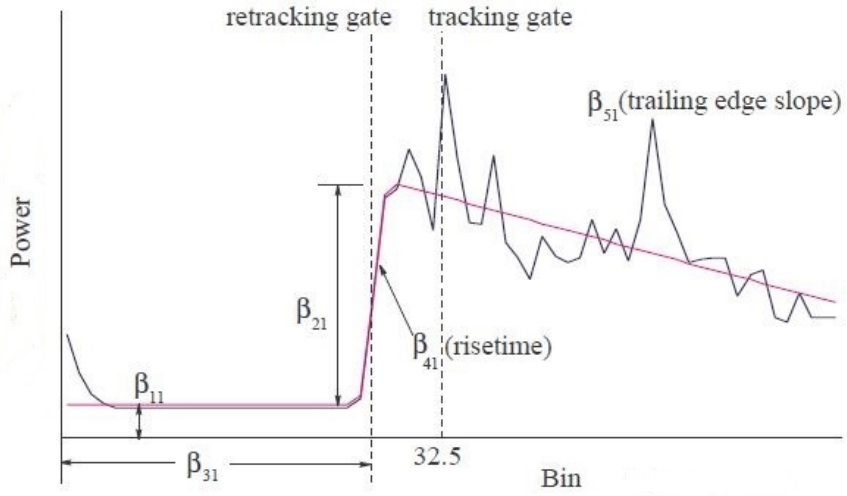

Figure 3.5: *5β-parameters model to fit a single ramped waveform of* ERS-1 *(Martin et al., 1983).*

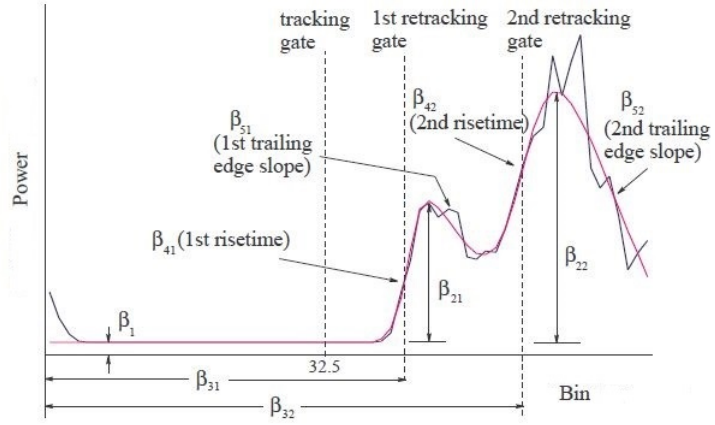

Figure 3.6: *9β-parameters model to fit a double ramped waveform of* ERS-1 *(Martin et al., 1983)*

3.3.2 SAMOSA3

This retracker is fully physically based and dedicated to retrack SAR waveforms. The model is based on radar instrument characteristics, satellite velocity, changes in satellite orbit height and physical properties of the scattering surface. A SAR waveform is constructed from:

$$W_{k,l} = P_u \left(\alpha_p^2 \sqrt{2\pi}\right) \sqrt{g_l} \Gamma_{k,l}(0) \left\{ f_0(g_l k) + \frac{\sigma_z}{L_\Gamma} g_l \frac{\sigma_z}{L_z} T_k f_1(g_l k) \right\} \quad . \tag{3.8}$$

This mathematical expression of the SAMOSA3 retracking algorithm and all of the related parameters are fully described in appendix A.

The SAR waveform is constructed based on the following principles:

- generation and transmission of a burst of chirp pulses

- reception of the reflected burst and multiplication of it by the complex conjugate of a delayed copy of the transmitted burst

- discrete sampling of the product signal (A/D conversion)

- Doppler correction
  The radar sensor and scattering cells on the illuminated surface inside the footprint are moving relatively. This relative motion leads to a change in the frequency of the received signals at the radar receiver. This Doppler shift affects the range measurements. Therefore the measured ranges need to be corrected.

- along-track Fast Fourier Transformation (FFT)

- Range Cell Migration Correction (RCMC)
  A given scattering cell is sensed several times. To have the same radar range for this cell, all of the ranges measured from this cell need to be corrected (Nielsen et al., 2014). This correction is called range cell migration correction. Figure 3.7 represents schematically a part of a SAR altimetry block diagram that includes the RCMC and Doppler corrections.

- along-track Inverse Fast Fourier Transformation (IFFT)

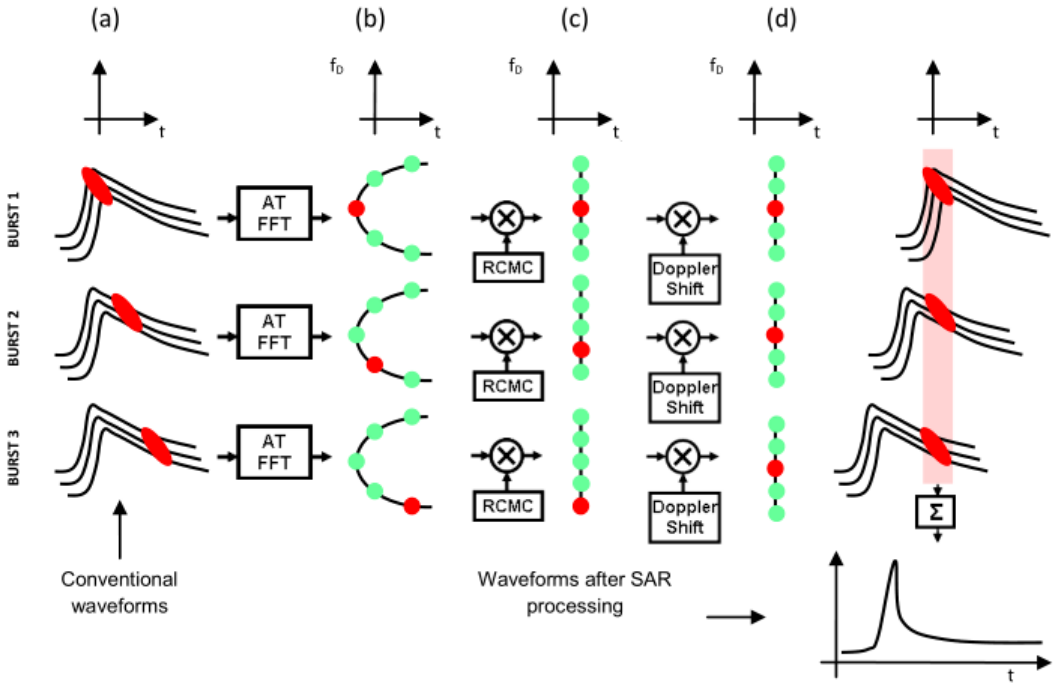

Figure 3.7: *Returned waveforms from the same Doppler cell (a), after along-track* FFT *(b), compensation of delay due to the range cell migration (c), Doppler shifted bins (d), f_D is the Doppler frequency. The red points show the information of the same scatterer (Nielsen et al., 2014).*

The whole processing chain to produce a SAR waveform is summarized in figure 3.8.

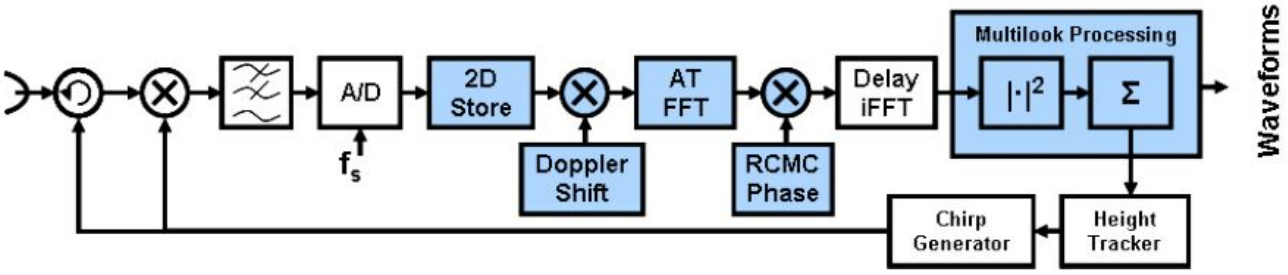

Figure 3.8: *Delay-Doppler altimetry block diagram (Nielsen et al., 2014)*

In the SAMOSA3 retracking algorithm the analytical function (3.8) must be fitted to the SAR waveform. Different parameters, e.g. waveform amplitude, backscatter coefficient and retracked gate, can be estimated. We are more interested in the retracked gate to be used in equation (3.1). The function (3.8) is non-linear and we use the Levenberg-Marquardt algorithm to estimate the unknown parameters. The Levenberg-Marquardt method is a standard technique used to solve nonlinear least squares problems. More information can be found in literature such as (Press et al., 1996) and (Gavin, 2011).

Figure 3.9 shows a number of example of SAMOSA3 model functions fitted to the measured SAR waveforms.

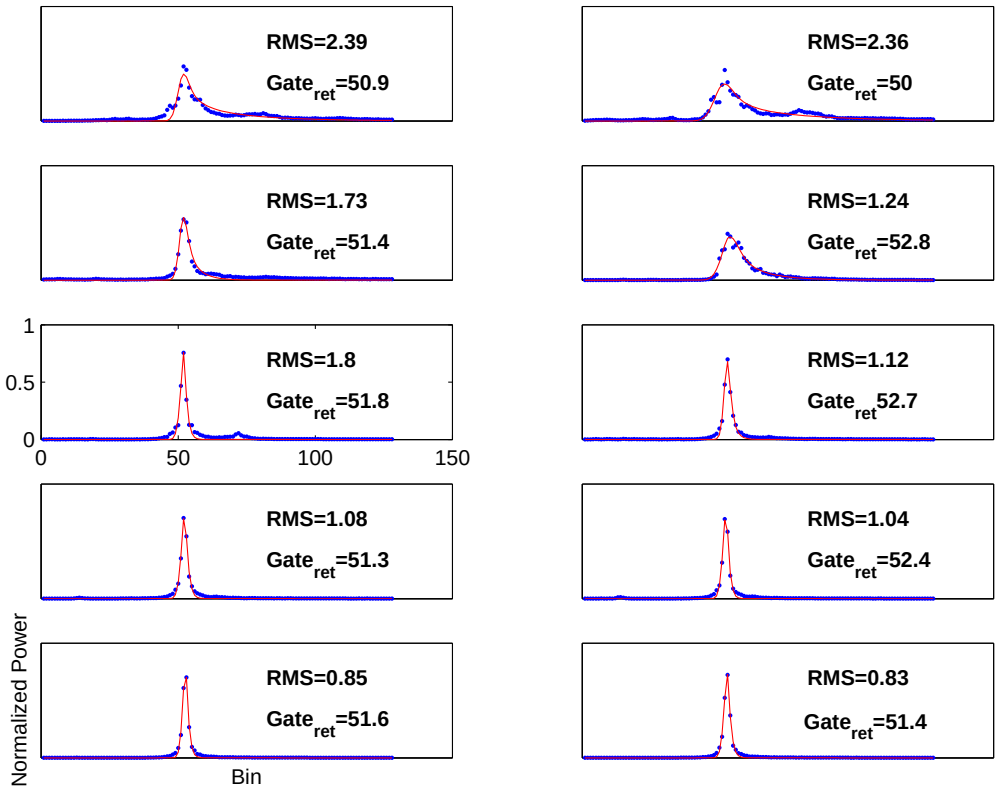

Figure 3.9: *Fitting the SAMOSA3 model to measured CryoSat-2 waveforms over Neagh lake, 25 November 2010. Blue dots are measured samples and red curves are the fitted functions. The RMS was calculated based on the normalized waveforms.*

3.3.3 Ice-2

The ice-2 retracker is intended to retrack the waveform over ice sheets. The expression of the waveform is derived from the Brown model. According to Legresy and Remy (1997) an error function is fitted to the leading edge of the waveform and the trailing edge is spanned by an exponential decrease function:

$$y(k) = \frac{P_u}{2}\left[1 + \text{erf}\left(\frac{k - \text{Gate}_{\text{ret}}}{\sigma_L}\right)\right] \exp\left[s_T(k - \text{Gate}_{\text{ret}})\right] + P_n \ , \tag{3.9}$$

in which, $\text{erf}(x) = \frac{2}{\sqrt{\pi}} \int_0^x e^{-k^2} dk$, k is the number of samples in a waveform, σ_L the width of the leading edge, P_u is the amplitude of the waveform, S_T the slope of the logarithm of the trailing edge and P_n is the thermal noise level.

3.3.4 Ocean

The ocean retracker is based on the Brown model. It is designed by Collecte Localisation Satellites (CLS) to retrack the waveform over the oceans. According to (Hayne, 1980) the mathematics behind this retracker is:

$$\begin{aligned} y(k) = a_\xi \frac{P_u}{2} \exp(-v) \Bigg\{ [1 + \text{erf}(u)] + \frac{\lambda_s}{6} \left(\frac{\sigma_s}{\sigma_c}\right)^3 \Bigg\{ [1 + \text{erf}(u)]\, c_\xi^3 \sigma_c^3 - \ldots \\ \frac{\sqrt{2}}{\sqrt{\pi}} \left[2u^2 + 3\sqrt{2} c_\xi \sigma_c u + 3 c_\xi^2 \sigma_c^2 - 1\right] \exp(-u^2) \Bigg\} \Bigg\} + P_n \ , \end{aligned} \tag{3.10}$$

in which $\text{erf}(x) = \frac{2}{\sqrt{\pi}} \int_0^x e^{-k^2} dk$, λ_s is the skewness parameter, $\gamma = \frac{1}{2\ln(2)} \sin\theta_0$, $\alpha = \frac{4cR_e}{\gamma H R_e + H}$, θ_0 is the antenna beam-width, c velocity of light, H satellite height, R_e is the Earth's radius and $\sigma_c^2 = \sigma_p^2 + \sigma_s^2$, σ_p is point target response with a significant wave height, SWH $= 2c\sigma_s$ and σ_s is the surface RMS wave height. Other parameters in equation (3.10) are:

$$a_\xi = \exp\left(\frac{-4\sin^2\xi}{\gamma}\right), \ b_\xi = \cos(2\xi) - \frac{\sin^2(2\xi)}{\gamma}, \ c_\xi = b_\xi \alpha, \ \xi = \text{mispointing angle} \ , \tag{3.11}$$

$$u = \frac{k - \text{Gate}_{\text{ret}} - c_\xi \sigma_c^2}{\sqrt{(2)}\sigma_s}, \ v = c_\xi \left(k - \text{Gate}_{\text{ret}} - \frac{c_\xi \sigma_c^2}{2}\right) \ . \tag{3.12}$$

The ice-1, ice-2, sea-ice and ocean retrackers are used on-board the Envisat and SARAL missions. The ice-1 and ocean retracker are also used on-board Jason-2.

3.4 Full-waveform retracking

When doing full-waveform retracking, we assume that there is only one type of terrain inside the footprint which leads to homogeneous responses from the illuminated area. If we consider the whole of a given waveform as one waveform then we can retrack it by all of the retracking algorithms mentioned in sections 3.2 and 3.3. For example the waveform in figure 3.10, which is a multi-peak waveform, is considered as one waveform. So for a given waveform and an individual retracker only one retracked range correction would be estimated.

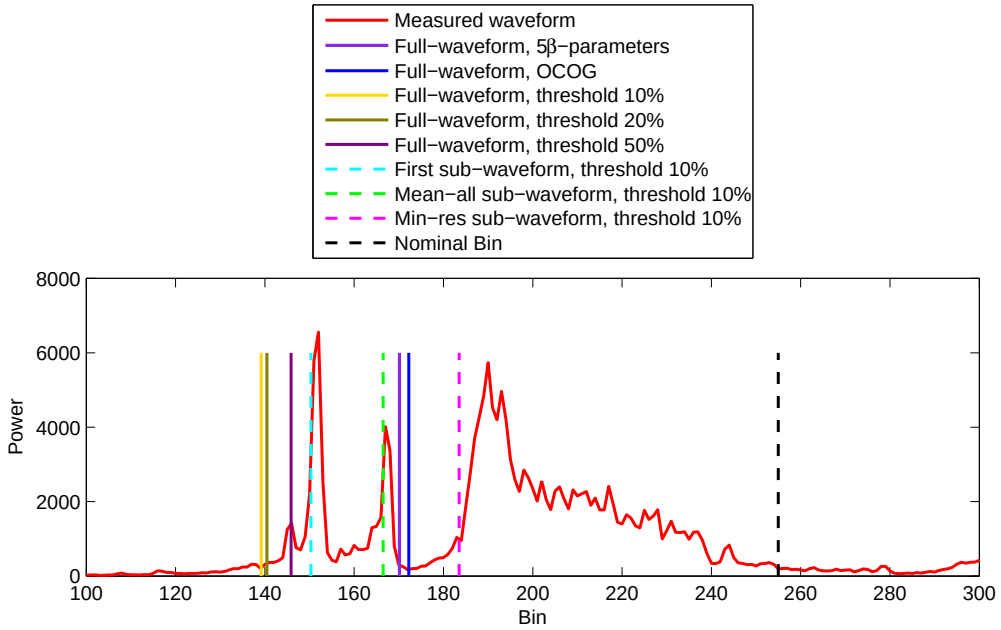

Figure 3.10: *A full-waveform of CryoSat-2* SARIn *mode over Nasser lake, 4 October 2010, includes 3 sub-waveforms. For visual purpose the waveform is plotted from gate 100 to gate 300. The* SARIn *mode waveform of CryoSat-2 consists of 512 gates.*

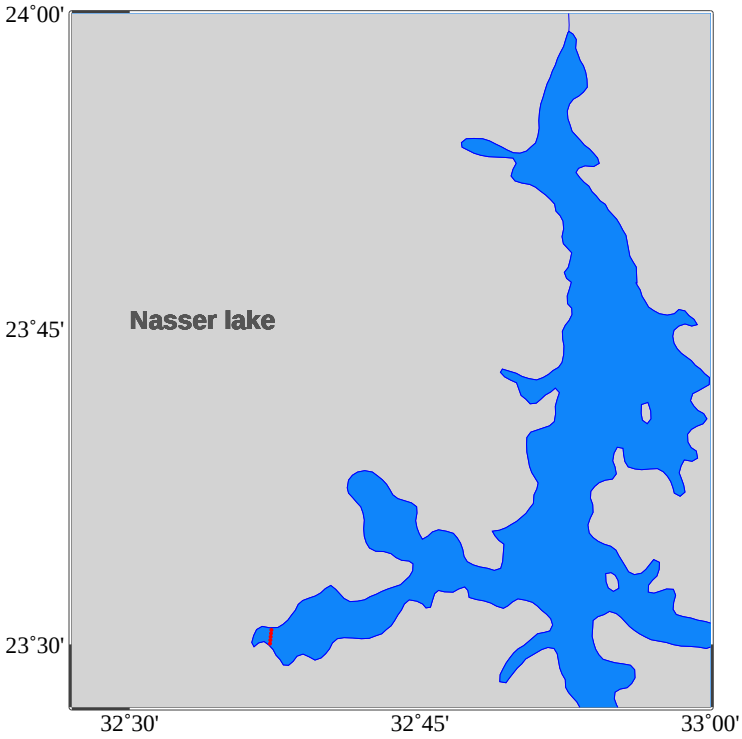

Figure 3.11: *Location of a track of the CryoSat-2* SARIn *mode (marked in red) which includes the corrupted waveform shown in figure 3.10*

sub1

Table 3.1: *Retracking scenarios*

retracker	full-waveform	sub-waveform		
		first	mean-all	min RMS
On-board	√	–	–	–
5β-parameters	√	√	√	√
OCOG	√	√	√	√
Threshold 10%	√	√	√	√
Threshold 20%	√	√	√	√
Threshold 50%	√	√	√	√
SAMOSA3 (SAR only)	√	√	–	–

3.5 Sub-waveform retracking

According to convolution (2.8) one of the main components that defines the waveform is the response of the illuminated surface inside the radar footprint. The surface response to the radar pulse depends on its constructing material properties. Over shallow water or near shorelines the waveforms are highly contaminated, because inside a given footprint there are different terrains, e.g. water, land and vegetation, with different responses to the radar pulses. This causes multiple meaningful peaks in the waveforms, each of which belongs to a small waveform. Therefore the returned waveform can be considered as a combination of several small waveforms, called sub-waveforms (Guo et al., 2010a). Figure 3.11 (red line) represents a pass of CryoSat-2 over a narrow part of Nasser lake. Flying over such a narrow and complex part of the lake leads to corrupted waveforms. Figure 3.10 shows a multi-peak waveform of CryoSat-2 SARIn mode for this pass.

Martin et al. (1983) also used the sub-waveform concept but for ice sheet monitoring. They mentioned in (Martin et al., 1983) that over an area covered with snow and ice there are double peak waveforms due to the responses from the snow and ice layers. As mentioned in section 3.3 they developed a special algorithm, i.e. 9β-parameter, to retrack this kind of waveforms. The 9β-parameters retracker which includes two peaks (corresponding to two sub-waveforms) is a proper retracker to analyze double peak waveforms (Martin et al., 1983).

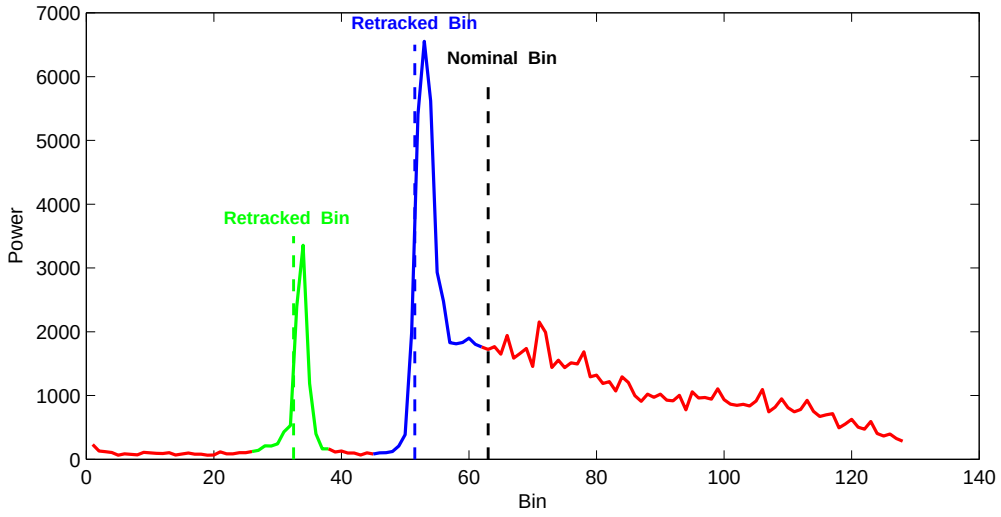

Figure 3.12: *A full-waveform of CryoSat-2 LRM mode over Qinghai lake, 9 August 2010 including 2 sub-waveforms*

The idea of sub-waveform retracking was then followed by Guo et al. (2006) for recovery of gravity anomalies over coastal oceans. Each leading edge corresponds to a potentially meaningful peak. For more precise ranging, the leading edges need to be scrutinized. The goal of the sub-waveform retracking technique is to detect all potentially meaningful leading edges for further processing. After detecting them, the sub-waveforms are constructed. For instance figures 3.10 and 3.12 show multi-peak waveforms of CryoSat-2 SARIn and LRM modes which

include three and two sub-waveforms respectively. In sub-waveform retracking, all detected meaningful sub-waveforms are retracked by the retrackers shown in table 3.1, to find out the best retracking scenario for water level monitoring of study areas (to be described in chapter 4). For sub-waveform retracking, the 9β-parameters model does not make sense because it is used for double-peak waveforms and is not used here. After finding and retracking all sub-waveforms, we must identify and select the proper one to be used for water level monitoring. Three strategies were considered to select the optimal sub-waveform for retracking:

1. First sub-waveform
   We assume that the first sub-waveform is the response from the water surface at nadir location. So, in this strategy, for all of the waveforms only the first detected sub-waveform is considered to be retracked to calculate the retracked range correction.

2. Mean correction from all of the sub-waveforms
   In this strategy we assume that we don't know which sub-waveform belongs to the water surface at nadir. So for a given full-waveform we use all detected sub-waveforms to compute range corrections. The final range correction is the mean value of the range corrections from all sub-waveforms. For example the full-waveform in figure 3.12 includes 2 sub-waveforms (shown with green and blue color) so we have 2 range corrections ΔR_1 and ΔR_2. The mean of ΔR_1 and ΔR_2 would be the representative range correction for the whole waveform. Figure 3.13 represents another example of a corrupted waveform including two sub-waveforms. This figure compares the retracked gate positions from the full- and sub-waveform retracking based on the OCOG algorithm. The blue vertical line is the retracked gate obtained from the full-waveform retracking and the cyan lines stand for retracked gates calculated from the first and second sub-waveforms. The green line is the mean retracked gate based on the first and second sub-waveforms.

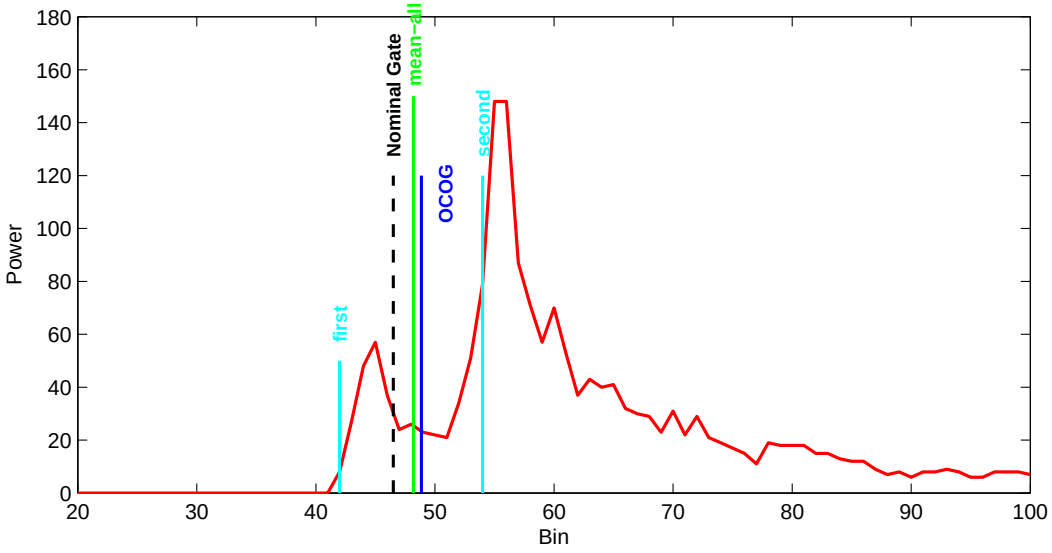

Figure 3.13: *A full-waveform of Envisat over Urmia lake, 15 August 2011 including 2 sub-waveforms*

Zwally et al. (2002) also used all peaks in the laser waveform, measured by ICESat mission, over ice sheets, ocean and land to estimate retracked range correction. They did not use the concept of the sub-waveform in their study and they determined one range correction per waveform. The maximum number of peaks in a given waveform in (Zwally et al., 2002) was supposed to be 6.

3. Minimum RMS sub-waveform
In this strategy, we select those sub-waveforms that minimize residuals with respect to a modeled time series. These models are used to remove outliers from the water level time series. We describe the models in chapter 4. To find a sub-waveform with the minimum RMS, the retracked water height was defined from each sub-waveform included in the given waveform. Then a sub-waveform which corresponds to the water level with the minimum RMS (with respect to the model) was selected to retrack water level variations. This retracking depends on the models that we fitted to the time series. The models and how they are fitted to the water level time series will be described in chapter 4.

Sub-waveform detection methodology

To detect potentially meaningful peaks, first the mean difference between the power at every gate and the gate after the next is computed:

$$d_2^i = \frac{1}{2}(P_{i+2} - P_i) \ , \qquad i = 1, 2, ..., N-2 \ . \tag{3.13}$$

While $d_2^i > \epsilon_2$, the index i is set to $i = i+1$, until $d_2^{i+j-2} > \epsilon_2$ and $d_2^{i+j-1} \leq \epsilon_2$ with $j \geq 3$, now the leading edge has been found with a doubt. To be sure that it is the leading edge, the power difference between the neighboring gates is computed:

$$d_1^k = P_{k+1} - P_k \ , \qquad k = i, i+1, ..., i+j-1 \ . \tag{3.14}$$

If d_1^k is greater than a threshold value ϵ_1, the k-th gate included in the leading edge gates. Guo et al. (2006, 2009) used fixed number for ϵ_1 and ϵ_2. They considered only the first detected peak (sub-waveform) in the waveforms. Fenoglio et al. (2010) used $\epsilon_1 = 0.2S_1$ and $\epsilon_2 = 0.2S_2$. Since over shallow water waveforms have different shapes it is better to compute ϵ_1 and ϵ_2 according to the shape of the waveforms. Here we used ϵ_1=AS_1 and ϵ_2=AS_2. A is selected based on the general shape of the waveforms for each inland water body. In our study A varies from 0.2 to 0.5.

After finding the leading edge n samples forward from the i-th gate and backward from $(i+j-1)$-th gate, $P_k(k = i-n, ..., i+j-1+n)$ are selected to form the sub-waveform. In general $n \leq$5. The parameters S_1 and S_2 are computed from the following equations (Guo et al., 2006, 2009):

$$S_1 = \sqrt{\frac{(N-1)\sum_{i=1}^{N-1}(d_1^i)^2 - \left(\sum_{i=1}^{N-1} d_1^i\right)^2}{(N-1)(N-2)}} \ , \tag{3.15}$$

$$S_2 = \sqrt{\frac{(N-2)\sum_{i=1}^{N-2}(d_2^i)^2 - \left(\sum_{i=1}^{N-2} d_2^i\right)^2}{(N-2)(N-3)}}, \tag{3.16}$$

where N is the number of gates in the waveform. For instance two sub-waveforms were detected from the waveform in figure 3.12. For this waveform S_1, S_2 and A are 4469.12, 5371.68 and 0.2 respectively.

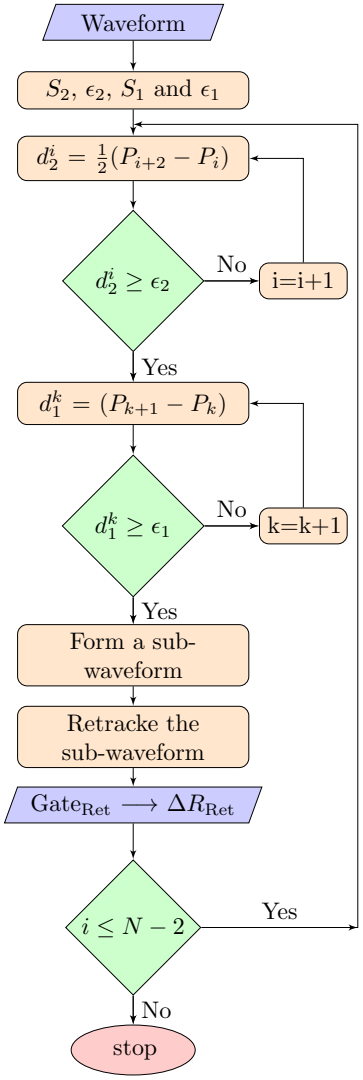

Figure 3.14: *Flowchart of finding and retracking sub-waveforms included in a given waveform*

Chapter 4

Areas of study, data sets and methodology

4.1 Areas of study

In this thesis we selected a small number of lakes with different shapes and sizes. We also selected different sections of a river to analyze the performance of different altimetry missions. Water level variations derived from satellite altimetry data must be validated against available in-situ gauge data. So the availability of in-situ gauge data was taken into account to select the study areas. Table 4.1 includes statistic information and satellite coverage over the study areas. In the following we describe the study areas and altimetry data that we used.

Table 4.1: *Study areas*

Object	Area (km^2)	Depth (m)	CryoSat-2 mode	Other missions
Neagh lake	392	10	SAR	Envisat, GLAS/ICESat
Nasser lake	5250	25	SARIn	Jason-2
Qinghai lake	4298	21	LRM	Envisat
Urmia lake	2286[1]	16	LRM	Envisat
Danube river	–	–	–	Envisat, SARAL, Jason-2

1-Surface area in 2015

4.1.1 Neagh lake

Neagh lake is the largest fresh water lake in Northern Ireland with a surface area of less than 400 km^2. The average depth of the lake is about 10 m and its maximum depth is 25 m (Harris and Mason, 1989). Besides the availability of in-situ gauge data, CryoSat-2 SAR mode coverage was another criterion to select this lake for studying. Out of the oceans and coastal zones the SAR mode coverage is limited for a small number of lakes and rivers as testing areas (ESA and MSSL-UCL, 2013). Size was another motivation to study this lake because small inland water bodies are the more challenging areas for satellite altimetry to monitor.

Neagh lake is observed by CryoSat-2 SAR mode, Envisat and GLAS/ICESat. Figure 4.1 shows the sub-satellite points (the nominal center of the footprint) of these altimeters over and around the lake.

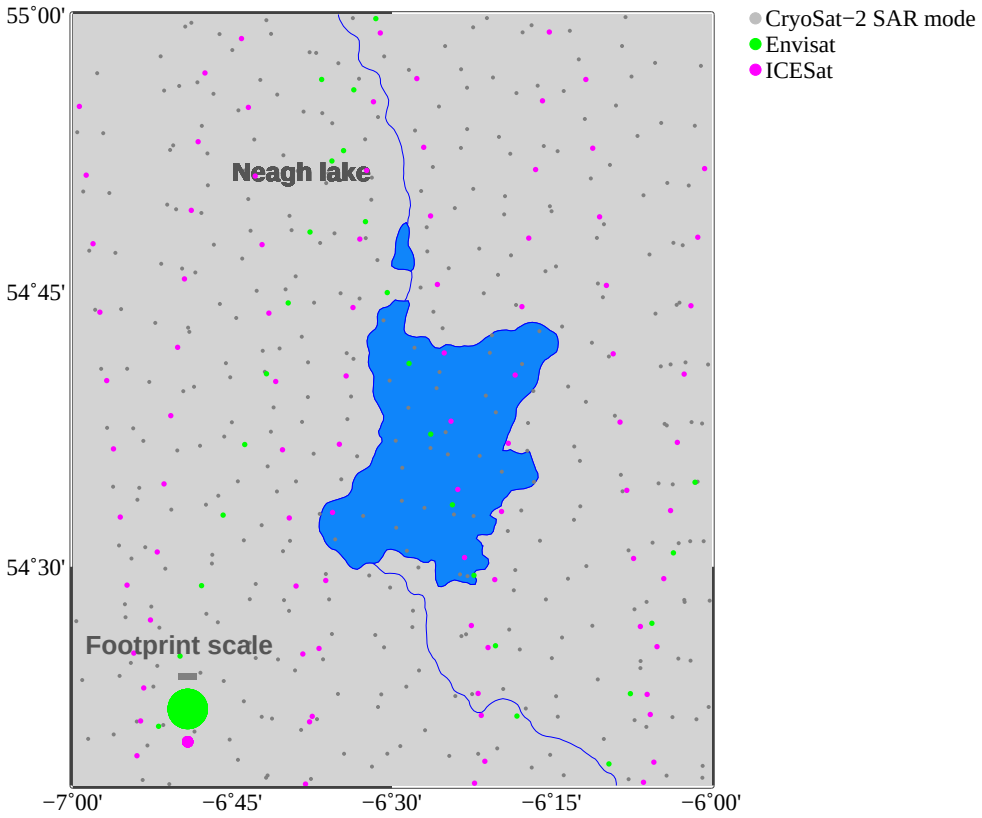

Figure 4.1: *CryoSat-2* SAR *mode (2012), Envisat (October 2010) and* ICESat *(Jan, Feb and April 2005) sub-satellite points over and around Neagh lake*

4.1.2 Nasser lake

Nasser lake is the biggest artificial fresh water resource in the world (El Gammal et al., 2010). It is located in the South of Egypt and the North of Sudan in a desert region with a very hot-dry climate and an annual evaporation ranging from 2.1 m yr^{-1} to 2.6 m yr^{-1} (Ebaid and Ismail, 2010). According to Elsawwaf et al. (2010) the annual rainfall over the lake is negligible. The main water inflow is provided by the Nile river. Nasser lake was created after constructing the Aswan dam across the Nile river (South of Aswan city) in 1964 (Mohamed, 2013). The lake has a surface area of 5250 km^2 with a length of 500 km and a width of 10 km to 60 km. The average and maximum depths of this lake are 25 m and 90 m respectively (Mohamed, 2013).

Nasser lake is one of the testing objects for the SARIn mode of CryoSat-2. We estimate its water level variations from CryoSat-2 (SARIn mode), Jason-2 and GLAS/ICESat data. The ground tracks of these altimeters are shown in figure 4.2.

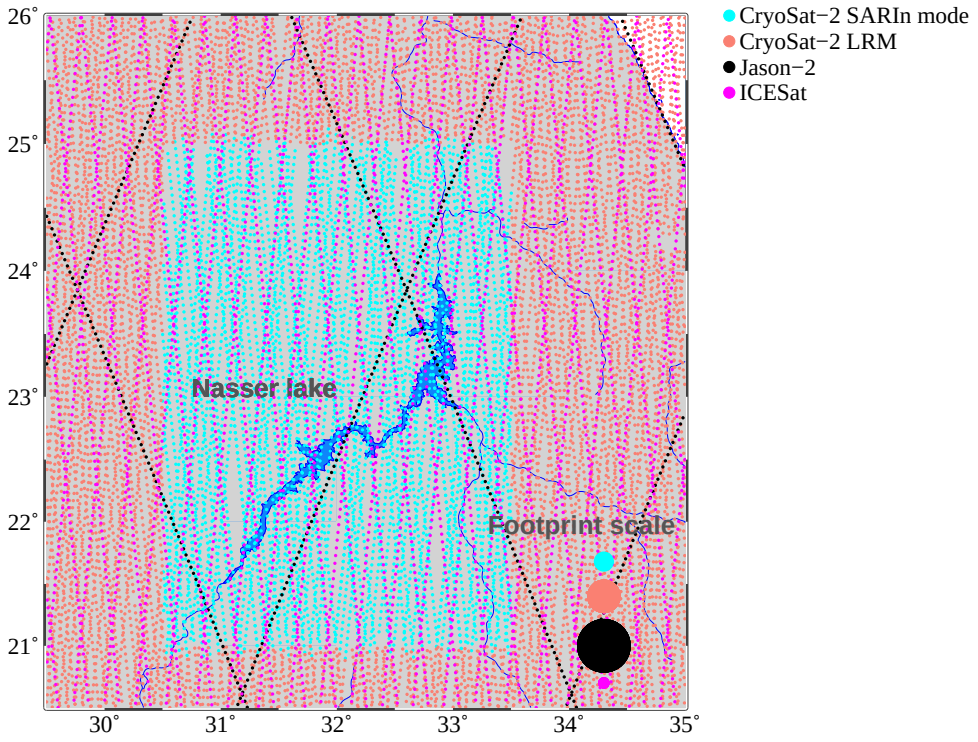

Figure 4.2: *CryoSat-2 (2012), Jason-2 (cycle 129, Jan 2012) and ICESat (Jan, Feb and April 2005) sub-satellite points over and around Nasser lake*

4.1.3 Urmia lake

Lake Urmia, located in the Northwest of Iran near its border with Turkey, is a hypersaline and endorheic lake which means that it retains water and allows no outflow to other external water bodies. It used to be the largest lake in the Middle East and the third largest salty water lake (salinity 300 g l^{-1}) on Earth (Asem et al., 2012). Because of high salinity, it is not fish habitat. Nevertheless Urmia lake is a significant natural habitat of Artemia which serves as a food

source for migratory birds like flamingos. The lake has been registered as an international protected area by UNESCO Biosphere Reserve (Rezvantalab and Amrollahi, 2011). Urmia lake has been divided into north and south parts by a causeway with a length of about 15 km with an opening bridge of 1500 m in the middle.

Its surface area was about 6100 km^2 in 1995 but it has been declining and it was estimated about 2366 km^2 in August 2011 (Pengra et al., 2012). During the last two decades the lake surface area has significantly shrunk due to human activities and climate effects. The water inflow to the lake is provided by several rivers and precipitation. Urmia lake is located in the middle of an important agricultural area. Over the inflowing rivers, several dams have been constructed to provide and retain water for irrigation purpose. So the water influx has been reduced significantly. On the other hand less precipitation and more evaporation are additional factors in the reduction of the lake's water supply. That caused an increased salinity and a reduced lake viability. The salinity has increased especially in the southern half of the lake which is shallower and warmer. A recent study (Tourian et al., 2015) shows the lake has lost 70% of its surface area during the last 14 years with an average rate of 220 $km^2\ yr^{-1}$.

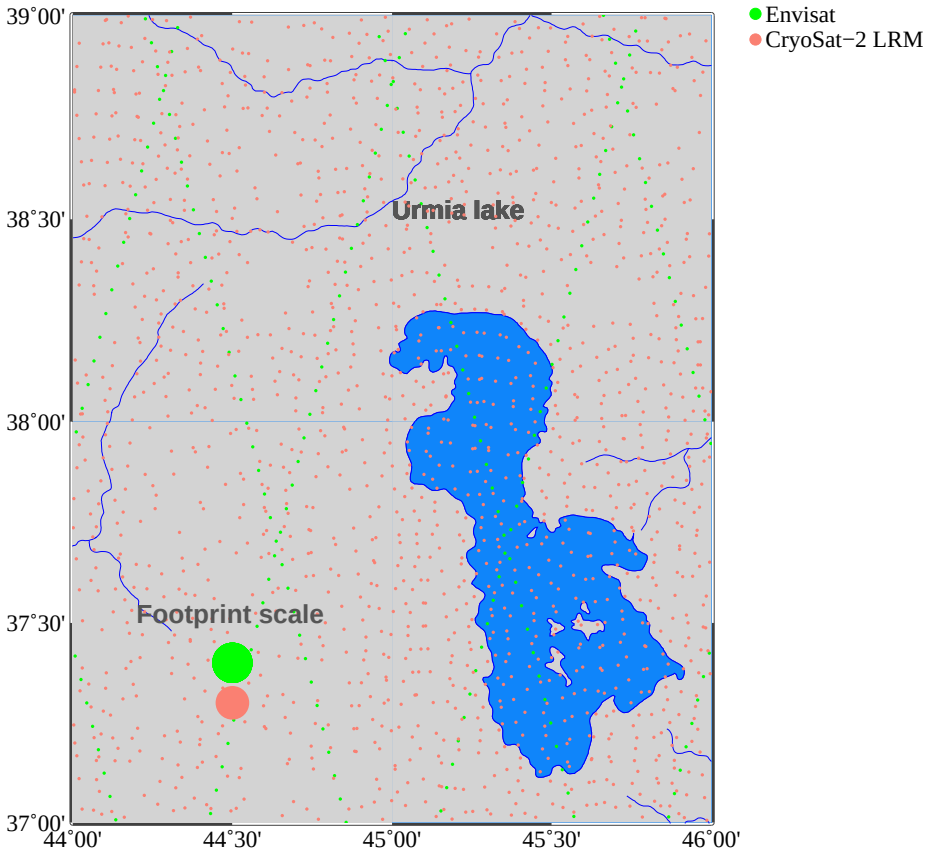

Figure 4.3: *Envisat and CryoSat-2 LRM sub-satellite points over and around Urmia lake*

To monitor water level variations we analyzed Envisat and CryoSat-2 LRM data. The coverage of these missions over Urmia lake is shown in figure 4.3.

4.1.4 Qinghai lake

Qinghai lake is an endorheic brackish lake with a salinity of 12.5 g l^{-1} (Zhu et al., 2014) that is located in the Northeast of the Tibetan Plateau. It is the largest lake in China that was formed due to inter-mountain tectonic depression (Zhang et al., 2011a). With a dimension of about 106 km length and 67 km width it has a surface area of 4318 km^2. The average depth is 21 m and its maximum depth is 25.5 m. Water influx is provided by direct rain and runoff of about 50 seasonal rivers (Zhu et al., 2014). Climatologically, this lake is located in a semi-arid region with cold-dry winters and humid summers. Due to the high altitude (about 3200 m) the annual mean temperature is 1.2° (Zhang et al., 2011a). According to Li et al. (2007) the annual mean precipitation and evaporation are 357 mm yr^{-1} and 924 mm yr^{-1} respectively. The main rainfall occurs from May to September. The east Asian monsoon, Indian summer monsoon and westerly jet stream cover the area (Li et al., 2007). Therefore it is one of the most sensitive regions for studying climate change. A high quality knowledge of water level variations of this lake is important to the climate, ecology and environmental research as well as the economy of the region.

We analyzed CryoSat-2 (LRM), Envisat and GLAS/ICESat data to determine water level variations. Figure 4.4 shows how these missions cover the lake.

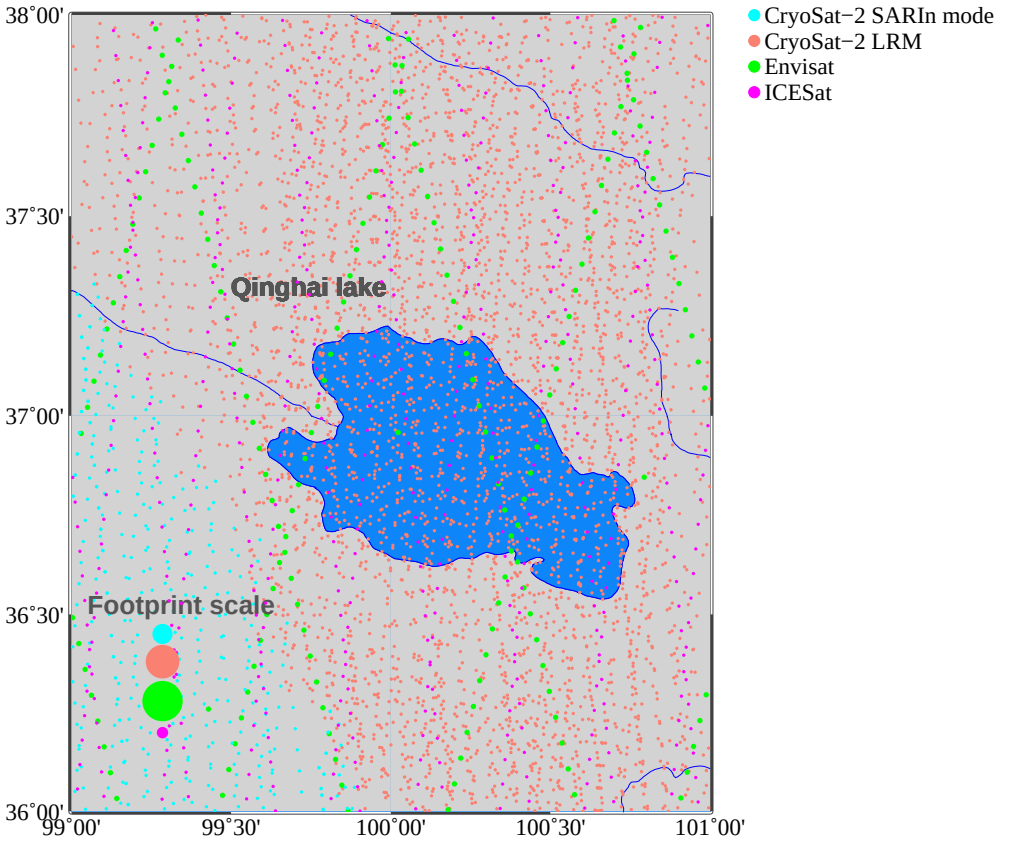

Figure 4.4: *CryoSat-2 (2012), Envisat (October 2010) and ICESat (Jan, Feb and April 2005) sub-satellite points over and around Qinghai lake, CryoSat-2 switches between LRM and SARIn mode around this lake.*

4.1.5 Danube river

With a length of 2850 km Danube is the longest river in western Europe (Zoran, 2003). It is originating in the Black Forest of Germany. The river passes thorough different countries like Germany (7.0% of basin area), Austria (10.0%), Slovakia (5.9%), Hungary (11.6%), Croatia (4.4%), Serbia (10.2%), Bulgaria (5.9%), Moldova (1.6%), Ukraine (3.8%) and Romania (29.0%) (Sommerwerk et al., 2009). It discharges into the Black Sea.

Wide rivers, e.g. Amazon, are not that difficult for the satellite altimetry to monitor. The narrower a river the more challenging to monitor by altimeters. Danube river, with a width of less than 1000 m, can be considered as a challenging object to be sensed by satellite altimeters. So it is interesting to evaluate their performance over such an object. Moreover the availability of in-situ gauge data for different stations along the river was a criterion to select this river for studying, because it gives us more chance to select a proper section of the river for studying.

Since the Danube river is narrow it was difficult to select proper locations to study its water level variations. The orientation of the river and satellite ground tracks is important in this respect. We analyzed satellite ground tracks over the river to find the locations where the river intersects the satellite ground tracks at steep angles, leading to a longer water profiles over the river. Being close to in-situ gauge stations was another criterion. We chose three locations of the river in Hungary close to in-situ gauge Baja and Dunaföldvár stations. Cyan stars on figure 4.5 show the location of the in-situ gauge stations. The distance from the in-situ gauge stations varies from 3.5 km to 10 km. The intersection of satellite ground tracks and the river are shown with red triangles on figure 4.5.

We studied water level variations of Danube river from analyzing Envisat, SARAL/Altika and Jason-2 mission data.

4.2 Data sets

4.2.1 Satellite data

Different sensors are usually mounted on a satellite platform, e.g. altimeter, radiometer, laser reflector and GPS receiver. Each sensor collects special data. Accordingly, each satellite mission data base includes a variety of data. Based on the objective in this research we used data collected by the altimeter sensors. We analyzed Geophysical Data Record (GDR) and Sensor Geophysical Data Record (SGDR) from different altimeters over different objects. We describe these data in the following separately for each mission.

4.2.1.1 Envisat

In the framework of its Earth observation program, ESA launched Envisat in March 2002 following two successful missions ERS-1 and ERS-2 in the 1990s. Envisat helped scientific communities to a better understanding of the Earth environment and climate change. It has an orbit with 98.6° inclination and 35 days repeat period which covers the Earth surface from $-81.4°$ to $+81.4°$ latitude. The main objectives of this mission were to provide long term observation of

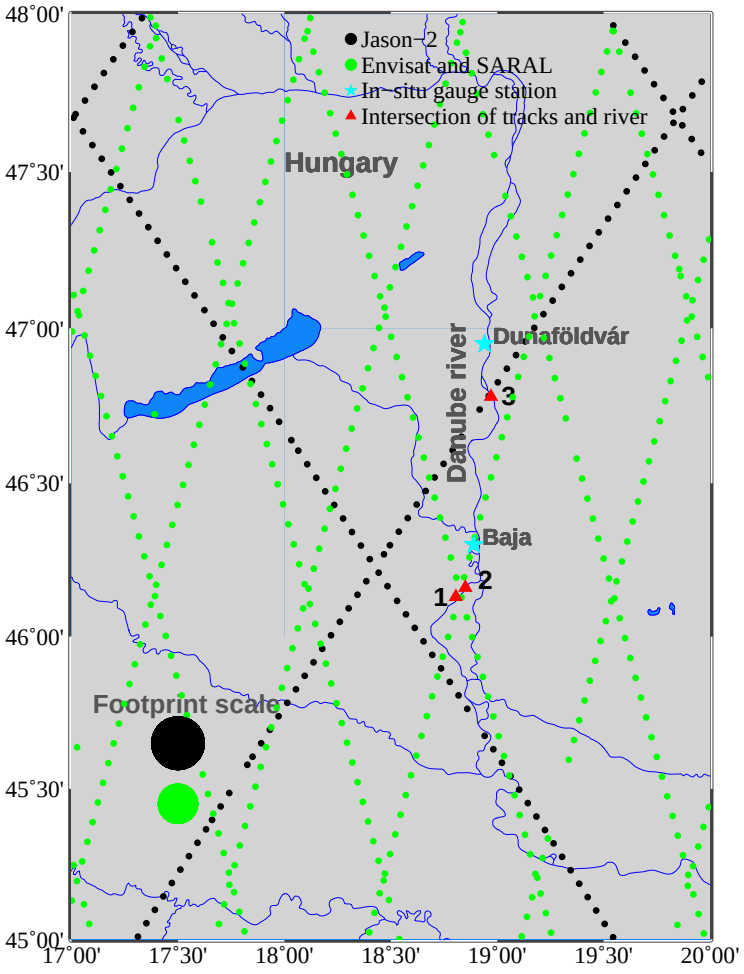

Figure 4.5: *Envisat (October 2010),* SARAL *(April 2013) and Jason-2 (Jan 2012) sub-satellite points over and around Danube river*

Earth's environment at a global scale and to improve the monitoring of Earth's resources (Frappart et al., 2006). To this end, Envisat carried a dual frequency (Ku- and S-band) radar altimeter RA-2 and other sensors, e.g. an Advanced Synthetic Aperture Radar (ASAR) and radiometers. The RA-2 instrument is a nadir looking pulse-limited altimeter operating at 13.575 GHz (2.3 cm wavelength) in Ku-band and at 3.200 GHz (9.4 cm wavelength) in S-band. Its footprint size is about 3.4 km.

In the thesis we use Envisat RA-2 GDR and SGDR from May 2002 to April 2012 (cycles 6–113) to estimate water level variations of Urmia and Qinghai lakes as well as Danube river. We also analyze GDR data of this mission for the same period of time over Neagh lake.

The RA-2 GDR data, distributed by ESA, fulfills the needs of most researchers. GDR data include time of range measurements, ranges, satellite positions, geophysical corrections, media corrections (mentioned in section 2.1) and other information. For the range measurements four different tracking and retracking algorithms, i.e. ocean, sea-ice, ice-1 and ice-2 are operationally applied to the RA-2 raw data to provide accurate height estimates (Frappart et al., 2006). Each retracker has been developed for a specific surface response. The RA-2 SGDR includes GDR, clusters of 20 waveforms for Ku- and S-band and additional information for each epoch. We are interested only in GDR and Ku-band waveform data (as part of SGDR data). Envisat heights are referenced to the WGS84 ellipsoid. The geoid heights are also provided based on the EGM96 gepotential model. More information about the RA-2 data content can be found in (Benveniste et al., 2002).

4.2.1.2 ICESat

Within the Earth observation system program NASA launched the Ice, Cloud and land Elevation Satellite (ICESat) in January 2003. The primary objectives of this mission were to monitor ice sheet mass balance (in Greenland and Antarctica) and to quantify the effect of changes in the Earth's atmosphere and climate on sea level and ice mass (Zwally et al., 2002). ICESat also measured global distributions of clouds and aerosols for atmospheric purposes. As secondary objectives, it provided observations to study land topography, sea ice and vegetation cover (Schutz et al., 2005).

With an inclination of 94°, ICESat had a 8 days repeat orbit during its calibration phase, after which it moved to nominal orbit with a 91 days repeat period and 33 days sub-cycle. It covered the Earth surface between $-86°$ and $+86°$ latitude.

The Geoscience Laser Altimetry System (GLAS) on-board ICESat used three laser transmitters that operated alternately. The altimeter sent 1064 nm (infrared) laser pulses to measure the surface elevation and 532 nm visible green laser pulses to detect the vertical distribution of clouds and aerosol (Schutz et al., 2005). It had a beryllium receiver telescope of 1 m diameter, solid state detectors for both 1064 and 532 nm signals. It also had a sub-system to measure pointing angles of each laser pulse and waveform digitizers to record the laser backscatter signal at both 1064 and 532 nm. One can find more information about characteristics of this laser altimeter in (Brenner et al., 2003). The GLAS altimeter, with a small footprint of about 70 m and spaced at 172 m along-track (Zwally et al., 2002), can also be used to monitor inland water bodies (Zhang et al., 2011b; Baghdadi et al., 2011).

GLAS/ICESat data are provided by the National Snow and Ice Data Center (NSIDC) of the University of Colorado (NSIDC, 2016) in binary and hdf formats with different versions for different surfaces. We used GLA14 (L2 level released 34) data which includes surface elevations, laser footprint geolocation, instrument and atmospheric corrections for range measurements (NSIDC, 2016). We analyzed this data from 2003 to 2009 to study water level variations of Neagh, Nasser and Qinghai lakes. We also used GLA01 (L1A level released 34) for the same period to extract the waveforms. The GLAS/ICESat waveforms are saturated under certain conditions, e.g. reflections over bright ice sheets and calm water bodies. For a precise water level determination the saturated waveforms need to be analyzed to derive saturation corrections.

Waveform saturation
The amount of energy in the laser waveform bins varies widely. In some of the bins the received energy exceeds the GLAS receiver's gain function. The higher returned energy saturates the detector and causes distortions in the measured waveform (Brenner et al., 2003; Abshire et al., 2005). This so called saturation effect frequently happens with large amplitude echoes from bright or flat illuminated surfaces, e.g. ice sheets and calm water (Brenner et al., 2003; Abshire et al., 2005). The saturation effect usually causes a positive range bias that leads to a negative bias in the surface height. Figure 4.6 shows examples of unsaturated and saturated waveforms. Based on the antenna gain function of the GLAS altimeter a threshold value is defined for each bin in the waveform. If the received energy for a given bin is higher than the threshold value, there is saturation effect. So the range extracted from the saturated waveform must be corrected. The saturation threshold values for each bin in the waveforms are shown in figure 4.7. The saturation corrections are provided in the GLA14 data files. They can be extracted and added to the measured ranges.

The reference ellipsoid of the ICESat mission is the same as used by Topex mission, i.e. a=6378.137 km and f= 1/298.257, (Leuliette et al., 2004) and the geoid heights are based on EGM96 model.

4.2.1.3 Jason-2

Launched in August 2008, Jason-2 is a follow-on mission of Jason-1. The Jason-2 mission is conducted under a cooperation between the NASA, the French space agency, CNES, the European Organization for the Exploitation of Meteorological Satellite (EUMETSAT) and the US National Oceanic and Atmospheric Administration (NOAA). The main goal of this mission is to extend the record of precise sea level measurements which was started with the launch of Topex/Poseidon in 1992 and continued by Jason-1 in 2001 (Dumont et al., 2009). Other objectives are to provide precise altimetry measurements in near-real time to be used in ocean forecasting and to make qualified measurements over coastal zones and inland water bodies (Nerem et al., 2010; Beckley et al., 2010).

Jason-2, with a 10 days repeat orbit, flies on the same ground track as the original Jason-1. There was a tandem period between Jason-1 and 2 for 180 days during the calibration phase of Jason-2 (Nerem et al., 2010). After that Jason-1 moved to a new orbit. Jason-2 covers the the Earth's surface from -66° to $+66^\circ$ latitude. Because of the large inter-ground track spacing (315.5 km at the equator) it can not observe many inland water bodies.

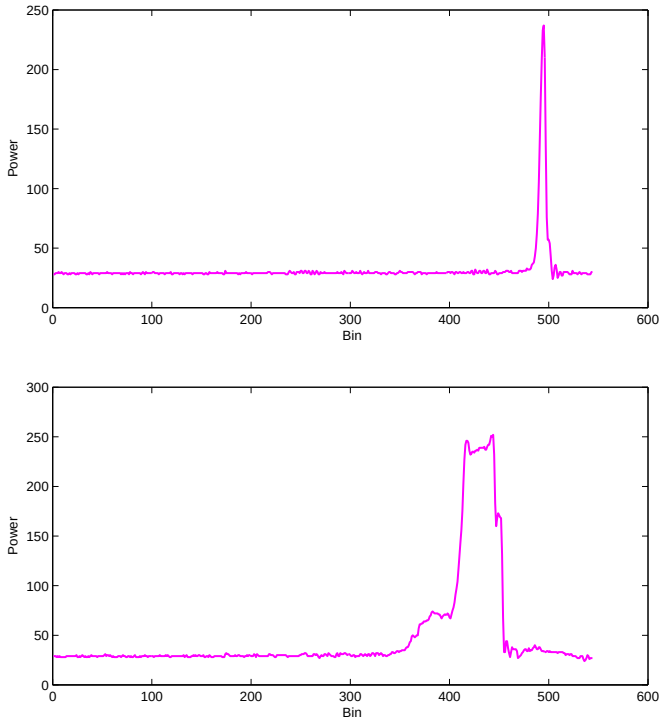

Figure 4.6: *Unsaturated (upper panel) and saturated (lower panel) waveforms of* GLAS/ICESat *over Neagh lake, October 2004*

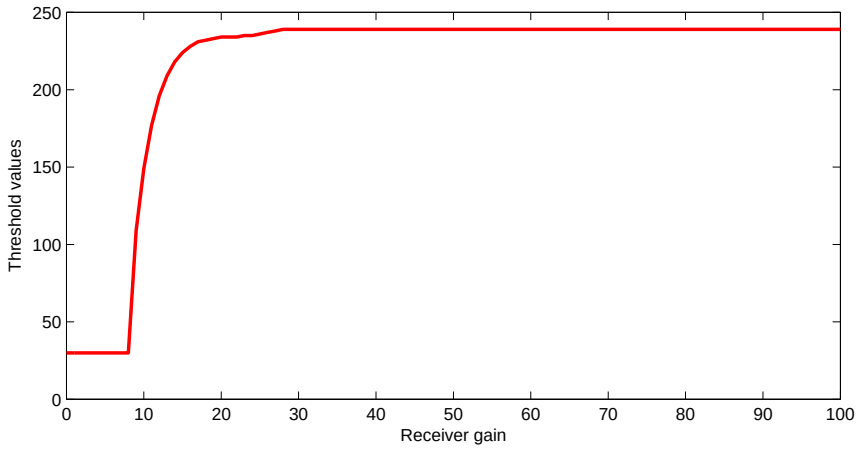

Figure 4.7: *Saturation threshold values for different bins in the laser waveform*

The Poseidon-3 altimeter, mounted on the platform of Jason-2, measures range with an accurate ionospheric correction. This correction is derived from the dual-frequency altimeter, Poseidon-2, carried by Jason-1 mission (Dumont et al., 2009). Poseidon-3 operates at 13.575 GHz (Ku-band) and 5.300 GHz (C-band). More information about Poseidon-3 is available in Dumont et al. (2009). This altimeter provides range measurements based on the ocean and ice-1 retrackers.

The reference ellipsoid of Jason-2 is the same as Jason-1 and Topex/Poseidon with an equatorial radius of 6378.137 km and the flattening coefficient of $f = 1/298.257$. The Jason-2 geoid is calculated from EGM96 geopotential model. Data of this mission is provided by Archiving, Validation and Interpretation of Satellite Oceanographic (AVISO), CNES data center (AVISO, 2016a). We used gdr_d data from July 2008 to June 2014 (cycles 0–238) to determine water level variation of Nasser lake. We also used sgdr_d data from July 2008 to December 2014 to study water level variation of Danube river.

4.2.1.4 CryoSat-2

CryoSat-2 is a European Space Agency satellite that was launched on 8 April 2010 within the Earth Explorer Program. The primary objective of this mission was to accurately determine the fluctuation in the Earth's marine ice cover and continental ice sheets (ESA and MSSL-UCL, 2013).

The SAR Interferometric Radar Altimeter (SIRAL) carried by CryoSat-2 is operating at 13.575 GHz with different measurement modes (Wingham et al., 2006). Over oceans, lands and flat ice sheets it operates in Low Resolution Mode (LRM), like conventional pulse-limited radar altimeters, e.g. Envisat and Jason-2. It works in Synthetic Aperture Radar (SAR) mode when it flies over sea-ice and a number of testing areas such as coastal zones, small patches of open ocean and selected rivers and lakes. SIRAL operates in Synthetic Aperture Radar Interferometry (SARIn) mode to monitor edges/slopes of ice sheets and a few inland water bodies (ESA and MSSL-UCL, 2013). CryoSat-2 has limited extra resources to acquire data in SAR or SARIn modes over experimental areas. They are selected upon user request based on a geographical mask which is updated every two weeks (ESA and MSSL-UCL, 2013). Figure 4.8 shows a rough view of the coverage of all measurement modes for 2012, based on the raw latitude and longitude from real data. A small gap close to the North of Africa could be due to sensor deficiency or an error to change the measurement modes. Even though CryoSat-2 was designed for ice monitoring, its radar system facility offers the possibility of studying water level variations of inland water bodies.

CryoSat-2, with a long repeat period of 369 days, has a dense spatial resolution and it covers many inland water bodies. Its ground track separation at the equator is 7.5 km according to table 2.3. It senses the Earth surface from -88° to $+88^\circ$ latitude. Figures 4.1–4.4 show the ground tracks of CryoSat-2 and the other missions over different areas.

We used both L1b and L2 level data of SAR and LRM modes of this mission from July 2010 to January 2014 to study water level variations of Neagh and Qinghai lakes respectively. We also analyzed L1b and L2i data of CryoSat-2 SARIn mode for the same period of time over Nasser lake. All CryoSat-2 data, used in this thesis, are based on the interferometer baseline B, B=1.168 m. More information about the interferometer baseline can be found in (Galin et al., 2013).

The SIRAL altimeter measures heights with respect to the WGS84 ellipsoid. The geoid height is also provided in CryoSat-2 data base according to EGM96 geopotential model. So by adding the geoid term to the satellite derived heights one arrives at heights referenced to the geoid model. The CryoSat-2 on-board range measurements are included in L2 and L2i data. They are calculated from the full-waveform processing based on the CryoSat-2 Ground Segment (SG) retracking algorithm. The GS retracker was developed by ESA. More information about this retracker can be found in Wingham et al. (2006), Nielsen et al. (2014) and ESA and MSSL-UCL (2013). CryoSat-2 L2 data are corrected for the media, geophysical, instrument and geometry corrections (ESA and MSSL-UCL, 2013). The on-board L2i ranges of the SARIn mode are also corrected for instrument and geometry corrections, i.e. they are provided at nadir locations. To have fully corrected ranges the media and geophysical corrections must be implemented.

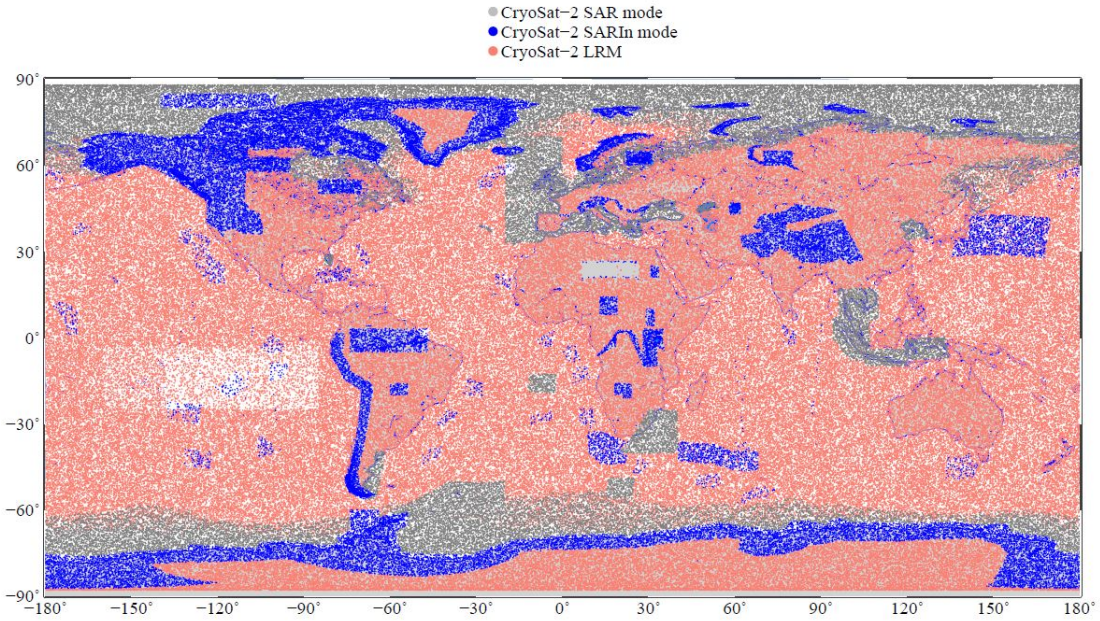

Figure 4.8: *CryoSat-2 coverage of all modes for 2012*

4.2.1.5 SARAL/Altika

Satellite for Argos and Altika (SARAL/Altika) is a follow-on mission to Envisat. Launched in February 2013, SARAL/Altika is operated by the Indian Space Research Organization (ISRO) and CNES (Schwatke et al., 2015). The main scientific objective of the mission is to provide data for oceanography purposes. For example to improve our knowledge of ocean meso-scale variability, to understand the oceanic component in the climate system, to study coastal dynamic process and to contribute to operational oceanography (Bronner et al., 2013). Secondary objectives are monitoring inland water bodies, sea ice and continental ice (Bronner et al., 2013).

SARAL/Altika has an orbit with 98.6° inclination. Its repeat cycle was 35 days until June 2016, with the same ground tracks as Envisat. Thereafter it has been moved to a drifting orbit due to technical issues. It can observe many inland water bodies. Altika is a 35.75 GHz Ka-band radar altimeter. Using a higher frequency is an advantage of this altimeter, because it reduces the footprint to around 2 km (equation (2.9)) that leads to better spatial resolution (Schwatke

et al., 2015). Also the effect of ionospheric disturbance is smaller at this frequency. However, Altika has a disadvantage because of sensitivity of Ka-band electromagnetic radiation to rainy and cloudy conditions (Bronner et al., 2013). Like RA-2 on-board the Envisat, Altika uses ocean, ice-1, ice-2 and sea-ice retrackers for range measurements (Ghosh et al., 2015).

The SARAL/Altika height measurements are referenced to an ellipsoid which is the same as that of Topex/Poseidon and geoid heights are calculated according to EGM96 geopotential model. We analyzed SARAL/Altika sgdr_t data from April 2013 to December 2014 (cycles 1–18) over the Danube river at different locations. These data are provided by AVISO (2016c).

4.2.2 In-situ gauge data

To validate the satellite derived water level variations of the study areas we used available in-situ gauge data for each object. These data are usually daily measurements so they have enough temporal resolution to assess the satellite altimetry result of water level measurements. The data are provided by different local agencies. Table 4.2 includes information about in-situ gauge data and agencies who provide the data.

Table 4.2: *In-situ gauge data*

Target	Time frame	Sampling	Reference height	Data provider
Neagh lake	2000–2014	15 min	Chart datum (Belfast)	RAC
Nasser lake	2000–2013	1 day	Geoid EGM96	AHDA
Urmia lake	2000–2012	1 day	Persian Gulf MSL	WARWA
Qinghai lake	2001–2009	1 day	Chinese National Datum	BHWR
	2010–2013			
Danube river	2000–2014	1 day	BMSL	HHFS

Neagh lake
A long water level time series (from 2000 to 2014) of the in-situ gauge, provided by Rivers Agency Coleraine (RAC, 2016), is available that covers the whole period of satellite measurements in our study. The temporal resolution of this data is 15 min. Usually the temporal sampling of in-situ gauge data is one day. For a given day, we used the mean of all 15 min measurement values to calculate sampling rate in day. In-situ gauge heights are referenced to chart datum in Belfast city (Iliffe et al., 2003).

Nasser lake
The national reference geodetic system in Egypt is WGS84 ellipsoid. The heights are referenced to a geoid derived from the EGM96 geopotential model (Dawood and Ismail, 2005). To establish this reference system two national control networks have been created by the Egyptian survey authority. The first (high accuracy) reference network consists of 30 stations that cover the entire territory of Egypt. The second geodetic control network is the national agricultural cadastral network established along the Nile river that is mainly used for agricultural purposes (Dawood and Ismail, 2005). The in-situ water level measurements are referenced to the EGM96 geoid model that are provided by Aswan High Dam Authority (AHADA, 2016).

Urmia lake
The reference for the physical height in Iran is Persian Gulf Mean Sea Level (PGMSL). National Cartography Center (http://www.ncc.org.ir), the national mapping authority, is responsible to calculate and to distribute the height for the entire area of Iran. The reference of the height system is a tide gauge network located along the coastline of Persian gulf. With daily measurements of the water level in this network and implementing the related corrections, e.g. tide correction, the PGMSL is estimated. The PGMSL height is distributed via leveling networks throughout Iran, e.g. to the Urmia region. The west Azarbaijan regional water authority (WARWA, 2012) provides in-situ gauge data of Urmia lake.

Qinghai lake
In-situ gauge networks of China are referenced to the Chinese national geodetic reference system. This system was created based on the Yellow sea datum in 1965 (Jiao et al., 2002). It was renewed in 1985 (Guo et al., 2004). The origin of the new system is located on Dagang tide gauge station in Qingdao city. Guo et al. (2004) calculated the vertical shift between 1985 national height datum and WGS84 ellipsoid. To estimate this shift (35.7 cm), they used data sets of 949 GPS/Leveling stations distributed over the country and the Earth gravity field models EGM96 and DQM99A. We received in-situ gauge data of Qinghai lake from Bureau of Hydrology and Water Resources (BHWR, 2016).

Danube river
We used in-situ gauge data from two stations of the Hungarian in-situ gauge network along the Danube river: Baja station, located at about 10 km away from the river intersection with the satellite ground tracks (track 0308 and 0616 from Envisat and SARAL respectively) and Dunaföldvár station, 3.5 km away from the intersection of the river and the Jason-2 ground tracks (track 0237). The in-situ gauge heights are referenced to the Hungarian national height datum, "Egységes Országos Vetület" (EOV) with respect to the Baltic Mean Sea Level (BMSL) (Völgyesi, 1997; Kiss et al., 2008). In-situ gauge data of Danube river in Hungary is provided by Hungarian Hydrological Forecasting Service (HHFS, 2016).

4.3 Biases among data sets

Since in-situ gauge data follow national policies they don't have the same elevation datum as the satellites elevation datum necessarily. So usually there is a bias between the water level from the satellites h_w (equation (2.14)) and from the in-situ gauge data that can range from a few decimeters to several meters for different satellites and different objects. The bias is defined as the difference between the mean water level from the satellite and from the in-situ gauge.

Furthermore, for a given satellite and a given object the water level derived from different retrackers has different biases with respect to the in-situ gauge data. Since we compare the result of each retracker with in-situ gauge relatively these biases don't play an important role in our analysis. However we removed these biases before calculating the RMS between retrackers derived water level and in-situ gauge data.

The satellite orbit height H is referenced to different ellipsoids for different altimetry missions. Therefore there is also a bias between water level time series derived from different altimeters. If these time series would be compared together or be merged to define a longer time series, it is necessary to remove inter-satellite biases. In this case water level from one of the altimeters is

considered as a reference in the comparison or merging process. Bosch et al. (2014) calculated and removed the bias between different altimeters to retrieve a long term data record of global and regional sea level changes. Tourian et al. (2016) studied water level variation of a number of rivers from different altimeters. They estimated and removed inter-satellite biases to merge water level from different altimeters.

In the case that there is no in-situ gauge data available and one uses a combination of different altimeters then one of the altimeters is considered as reference to estimate biases.

4.4 Methodology to derive water level variations

One can define water level variations of the inland water bodies from the altimeter measurements in two different ways:

- Water level from the on-board measured ranges
  In this way of defining the water level variations, the on-board range measurements are used. The on-board ranges have been extracted from time delay measurements which are referenced to a nominal (predesignated) gate in the waveforms. Usually these ranges have been provided in the L2 data files of each altimeter and they are ready to be used. Just they must be corrected due to media and geophysical effects such as dry and wet troposphere, ionosphere, solid earth and pole tides. These corrections are also included in L2 data files. Using the on-board ranges to derive the water level is easy and fast. It is a conventional way to derive the water level variations of deep oceans, but it is usually not an accurate method to monitor inland water bodies.
- Water level from retracking the measured waveforms
  To estimate the water level accurately, the measured time delay must be referenced to a retracking gate in the measured waveform. The retracking gate does not necessarily correspond to the nominal gate for a given waveform. Over inland water bodies the difference between the nominal and retracked gates can be too much. For example the retracked gate of the Envisat waveforms over Urmia lake varies from 20 to 100 while the nominal gate is located at 46.5. For further examples we point to figure 3.2. As it is clear from this figure, the retracked gates are located around 150 while the nominal gate for SARIn mode is 255. According to CryoSat-2 SARIn mode characteristics this difference (255−150) leads to about 50 m difference in the range measurements. Therefore the on-board ranges must be corrected due to not only the media and geophysical effects but also due to the difference between the nominal and retracked gates. So instead of on-board ranges we use the ranges which are derived from waveform retracking (so called retracked range) to derive the water level. The retracked range corrections are obtained from the waveform retracking algorithms described in chapter 3. In this method of the water level measurements we use levels L1b and L2 (L2i for CryoSat-2) to estimate the water level. This method is obviously not as fast as the first method but it is more accurate.

To estimate water level variations from the measured on-board ranges equation (2.14) would be as following:

$$h_w = H - (R + \sum \Delta R) - h_g \ , \tag{4.1}$$

in which $\sum \Delta R$ includes all of the corrections mentioned in table 4.3 and h_g is the geoid height with respect to an ellipsoid. The geoid height is provided in the altimetry data base for each

mission mostly from the EGM96 geoid model. In some cases, e.g. CryoSat-2 LRM for Qinghai lake, we used the geoid from EGM2008 model (Pavlis et al., 2012) instead of the geoid provided in the altimetry data base.

Table 4.3: *Range correction*

Correction	Mission				
	Envisat	ICESat	Jason-2	CryoSat-2	SARAL
Dry atmosphere	√	√	√	√	√
Wet atmosphere	√	√	√	√	√
Ionosphere	√	√	√	√	√
Solid earth tide	√	√	√	√	√
Geocentric pole tide	√	√	√	√	√
Saturation	–	√	–	–	–
Retracked	√	√	√	√	√

In the second way of the water level estimation, the retracked range correction ΔR_{ret} estimated from the waveform retracking (equation (3.1)) was added to the range correction. So equation (2.14) was modified as:

$$h_{\text{w}} = H - (R + \sum \Delta R + \Delta R_{\text{ret}}) - h_{\text{g}} \ , \tag{4.2}$$

to define the water level time series.

In this thesis we used both methods to define and analyze water level time series of the study areas and compared them with in-situ gauge data in order to assess their accuracy. Our methodology consists of the following steps:

1. Selecting all coverage data over the study areas.
   We defined a polygon over the border of each object. Based on the latitude and longitude of the polygon and satellite ground tracks we only selected the data which are inside the polygon.

2. Defining instantaneous water level time series.
   We defined a single-pass water level of the study areas from each satellite overpass, called instantaneous water level profile. Then a linear trend, $h_{\text{w}}(t_{\text{i}}) = a + bt_{\text{i}}$, was fitted to the instantaneous water level profile to detect and delete outliers at the confidence level of 95%. Each satellite overpass takes a few seconds. We consider only the mean water level and do not allow water level variations during the overpass. Therefore a linear trend would be sufficient to detect and delete outliers.

3. Merging all single-pass water levels to create a time series from all passes.

4. Fitting the following model including linear and quadratic as well as trigonometric terms.

$$h_{\text{w}}(t_{\text{i}}) = a + bt_{\text{i}} + ct_{\text{i}}^2 + d\sin\left(\frac{2\pi}{T}t_{\text{i}}\right) + e\cos\left(\frac{2\pi}{T}t_{\text{i}}\right) \ , \tag{4.3}$$

in which a, b, c, d and e are unknown parameters that are estimated by least squares adjustment. T is the annual period and h is the water height. This model (trend) can capture the permanent and periodic (seasonal) as well as the acceleration of water level variations (Roohi, 2015).

For lakes with no annual behavior we used a third degree polynomial to identify and delete outliers at the same confidence level.

$$h_w(t_i) = a + bt_i + ct_i^2 + dt_i^3 \tag{4.4}$$

5. Identifying and deleting outliers from the long time series.
   We used 95% confidence level to find the outliers. So the observation in the critical range $\alpha \in [-5\%, +5\%]$ were considered as the outliers and excluded from further processing. We used the least squares principle iteratively to fit the model to the satellite water level time series.

6. Removing a possible bias between the satellite and in-situ gauge water level time series.
   The bias is defined as the difference between the mean water level from the satellite and from the in-situ gauge.

7. Comparing the water level time series derived from the on-board ranges based on different on-board retrackers with available in-situ gauge data to find the most precise so called on-board water level estimator.

8. Comparing the water level time series derived from retracking the waveforms based on different retrackers with available in-situ gauge data to find the most precise retracked water level estimator.

9. Comparing the result of the most accurate on-board water level estimator with that of the most accurate retracked water level estimator to find the best scenario for water level monitoring.

We evaluated the performance of each satellite altimetry mission based on the RMS of water level with respect to the in-situ gauge data. The percentage or the number of valid observations (number of observation after removing the outliers), involved in defining the water level variations with our algorithm, were considered in this evaluation as well. The smaller RMS and the greater number of observations correspond to a better performance for a mission.

Chapter 5

Water level variations of inland water bodies from different altimeters

5.1 Lake water level variations

5.1.1 Neagh lake

We defined water level variations of this lake from analyzing the CryoSat-2 SAR mode, ICESat and Envisat data which is shown in figures 5.1 and 5.2 .

CryoSat-2 SAR mode
Neagh lake provides one of the few test scenarios for the CryoSat-2 SAR mode. We evaluated the performance of SAR altimetry in terms of the water level RMS together with other satellite missions against in-situ gauge data. To this end, first we derived the water level time series of the lake from on-board range measurements, i.e. using L2 SAR mode data.

Table 5.1: RMS(cm)/N *of water level and percentage of observations from different satellite missions and different retrackers (Neagh lake)*

mission	retracker	full-waveform	sub-waveform		
			first	mean-all	min-res
Envisat	Ice-1	19/61	–	–	–
Envisat	Ice-2	56/75	–	–	–
Envisat	Sea-ice	100/89	–	–	–
Envisat	Ocean	36/78	–	–	–
ICESat	On-board	**13/100**	–	–	–
CryoSat-2	GS	24/88	–	–	–
CryoSat-2	5β-parameters	22/92	64/94	34/92	33/92
CryoSat-2	OCOG	30/92	55/94	23/92	40/92
CryoSat-2	Threshold 10%	23/92	**16/92**	**15/92**	40/92
CryoSat-2	Threshold 20%	22/92	21/92	**18/97**	18/92
CryoSat-2	Threshold 50%	**16/92**	24/94	21/92	24/92
CryoSat-2	SAMOSA3	**17/92**	**15/80**	–	–

The geoid correction to the satellite derived height implies a shift of 1.45 m. So the water level from the satellite was shifted by 1.45 m to compare with in-situ gauge time series. An RMS of 24 cm was estimated for the water level of this lake from CryoSat-2 GS retracker. Different altimeters may use different geoid models but the geoid heights of all missions used in the thesis are referenced to EGM96 geopotential model.

Then we retracked the full- and sub-waveforms of SAR mode data with different retracking algorithms. The bias between retracked water level and in-situ gauge was removed in the validation process. The results of our analysis are summarized in table 5.1. The minimum RMS, 15 cm, was obtained with a threshold of 10% when we considered the mean retracked corrections from all of the detected sub-waveforms. The same retracker provides a 23 cm RMS in the case of the full-waveform retracking. The SAMOSA3 retracker yields an RMS of 15 cm if we retrack the first detected sub-waveform and 17 cm RMS for the full-waveform retracking. This retracker retrack well full-waveforms and the first sub-waveforms but over mean-all and mean-res sub-waveforms for most of the waveforms can not provide a proper range correction. For this reason we evaluated its performance only over the full-waveforms and the first sub-waveforms.

In the title of table 5.1 and similar tables (in chapter 5) in "RMS(cm)/N", RMS is the RMS of water level and N is the percentage of observation involved in the water level determination.

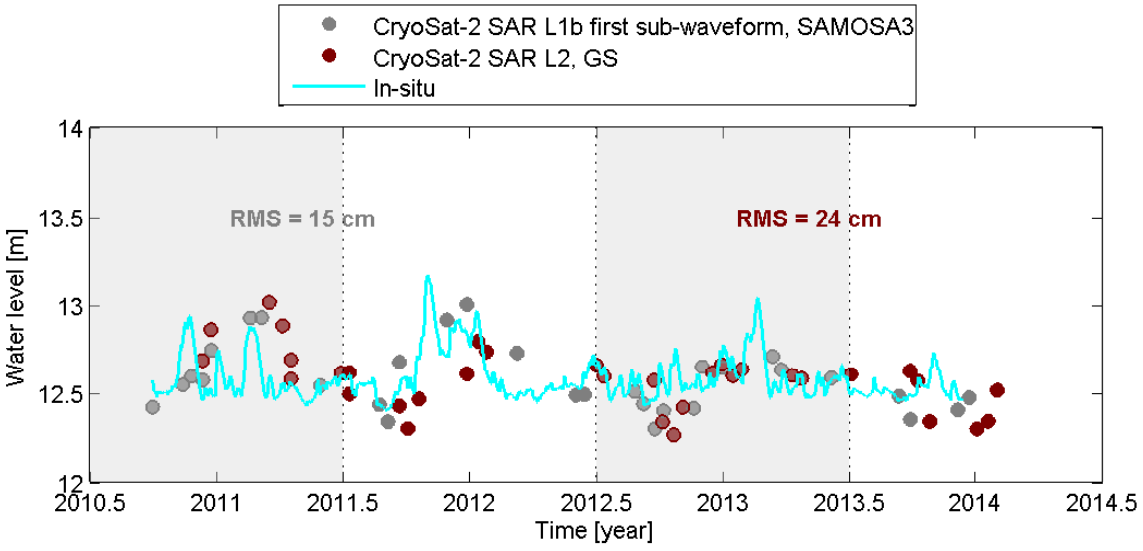

Figure 5.1: *Water level variations of Neagh lake from CryoSat-2 SAR mode and in-situ gauge data*

Envisat

We also defined water level variations from Envisat on-board retrackers (RA-2 GDR data). After removing the bias we compared the water level from each on-board retracker, i.e. ice-1, ice-2,

sea-ice and ocean with the in-situ gauge data to find the most accurate on-board retracker. The best result is obtained by the ice-1 retracker which provides a 19 cm RMS after removing a bias of 26 cm.

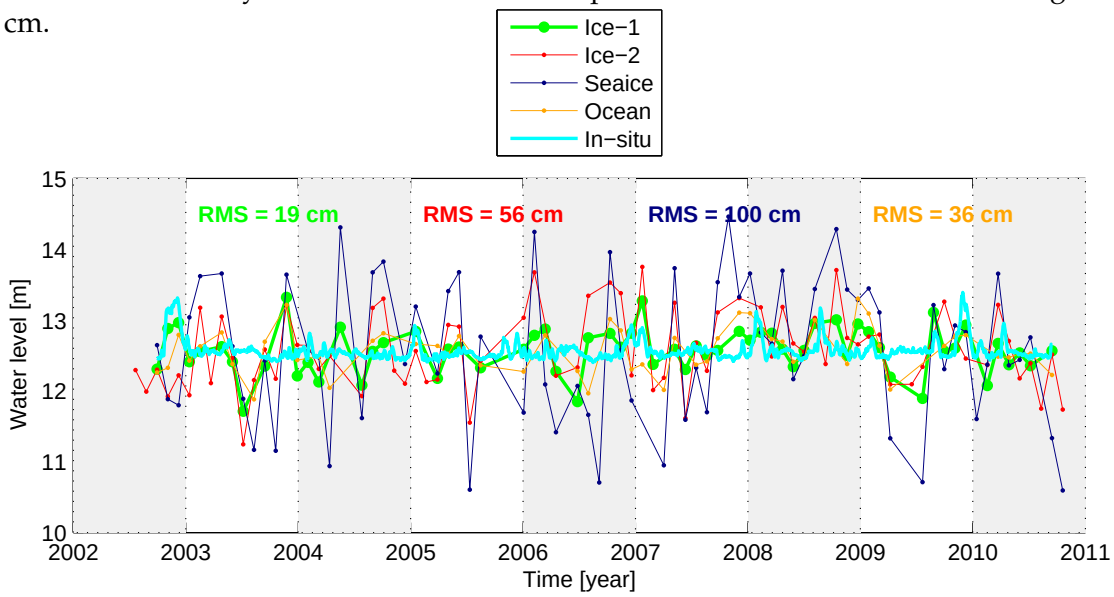

Figure 5.2: *Water level variations of Neagh lake from Envisat on-board retrackers and in-situ gauge data*

GLAS/ICESat

GLA14 and GLA01 data of the GLAS altimeter were also analyzed. After removing the bias (48 cm) with respect to the in-situ gauge data an RMS of 19 cm was obtained from the GLA14 data. After correcting the on-board range measurements due to saturation effects we derived the water level of the lake again. The RMS was improved to 13 cm by implementing the saturation correction.

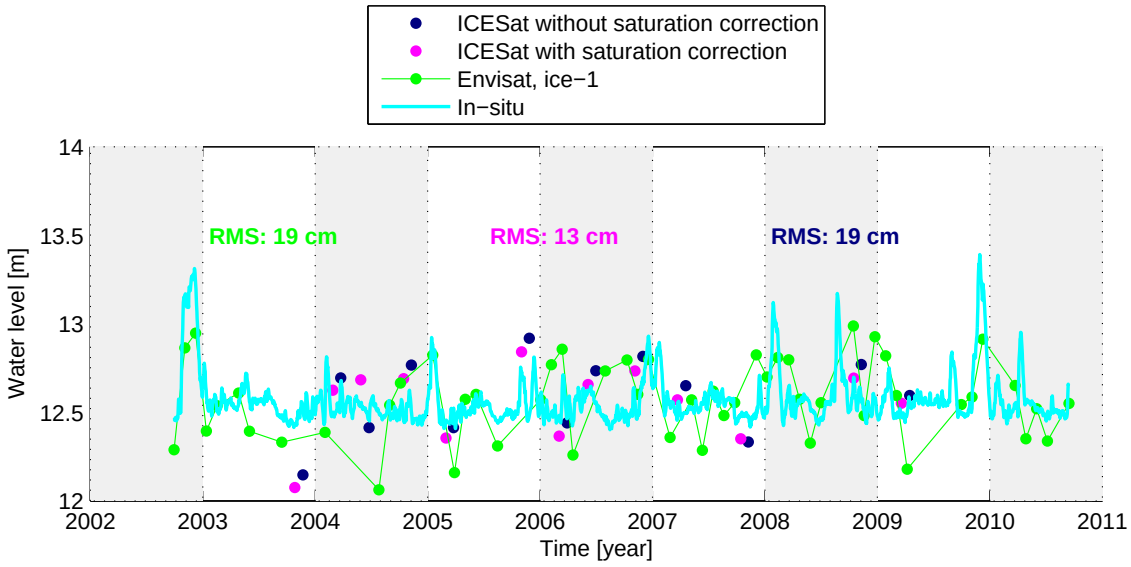

Figure 5.3: *Water level variations of Neagh lake from ICESat, Envisat and in-situ gauge data*

5.1.2 Nasser lake

CryoSat-2 SARIn mode

Nasser lake is one of our testing areas for the CryoSat-2 SARIn mode. This lake is a challenging object for satellite altimetry because of its special shape. According to figure 4.2 this river-like lake is a narrow and elongated (in the direction of the Northeast-Southwest) water body which has been created on the Nile river. The river's surrounding topography creates a very complex shape for the lake shoreline which exacerbates the satellite altimetry sampling over the lake surface. The main objective to select this lake was to assess the performance of the CryoSat-2 SARIn mode. We therefore analyzed water level variation derived from on-board range measurements and from post-processing of the SARIn waveforms. To this end, first we derived water level from L2 SARIn data. The lake water level derived from the GS retracker was compared with in-situ gauge data. After removing a 50 cm bias with respect to the in-situ gauge data an RMS of 32 cm was achieved.

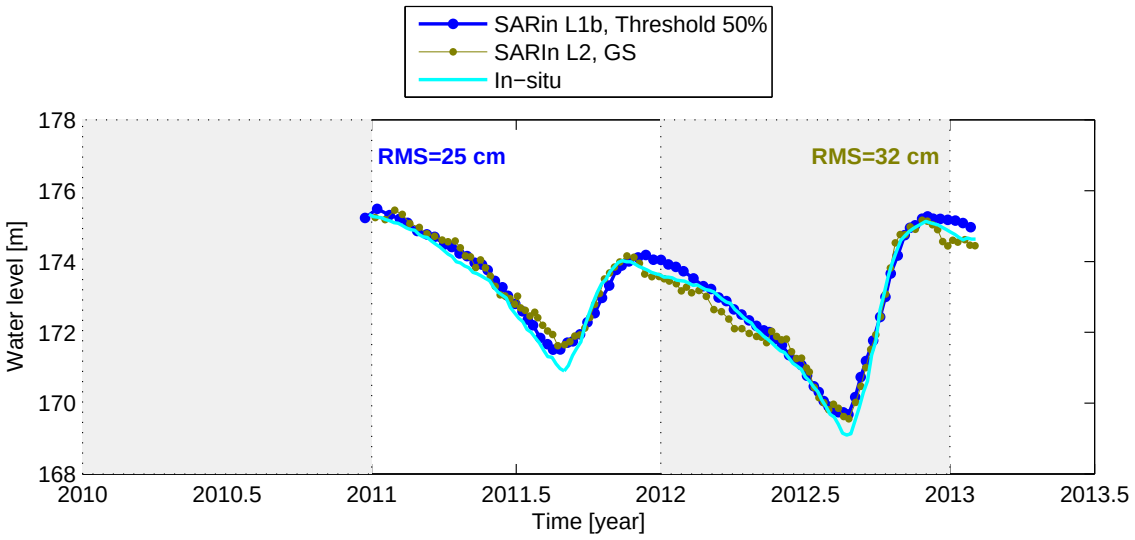

Figure 5.4: *Water level variations of Nasser lake from CryoSat-2 SARIn mode and in-situ gauge data*

Then we retracked the full- and sub-waveforms of this mode with different retracking algorithms. In the retracking we used the L1b and L2i data. The waveforms were extracted from L1b data and the remaining information, e.g. the ranges, was derived from L2i data that provided for the nadir locations. The results of this analysis are summarized in table 5.2. We use a moving average to define the water level from both L2 and L1b (with the combination of L2i) level data of CryoSat-2. The minimum RMS of 25 cm, after removing a 53 cm bias, is provided by the threshold 50% retracker when it retracks the full-waveforms. The RMS obtained from this scenario is 40 cm without using the moving average. The GS retracker has an RMS of 32 cm from the full-waveform retracking and an RMS of 44 cm for the original water level time series (not averaged). The retracked water level from the best SARIn waveform retracking scenario is plotted in figure 5.4.

Table 5.2: RMS (cm)/N *of water level and percentage of observations from different satellite missions and different retrackers (Nasser lake)*

mission	retracker	full-waveform	sub-waveform		
			first	mean-all	min-res
ICESat	On-board	31/100	–	–	–
Jason-2	Ice-1	54/100	–	–	–
Jason-2	Ocean	125/95	–	–	–
CryoSat-2	GS	**32/93**	–	–	–
CryoSat-2	5β-parameters	59/100	47/86	30/99	30/89
CryoSat-2	OCOG	136/99	47/86	33/86	48/90
CryoSat-2	Threshold 10%	74/99	37/100	**28/87**	34/90
CryoSat-2	Threshold 20%	44/96	38/86	**28/85**	39/90
CryoSat-2	Threshold 50%	**25/99**	46/85	**28/86**	42/90

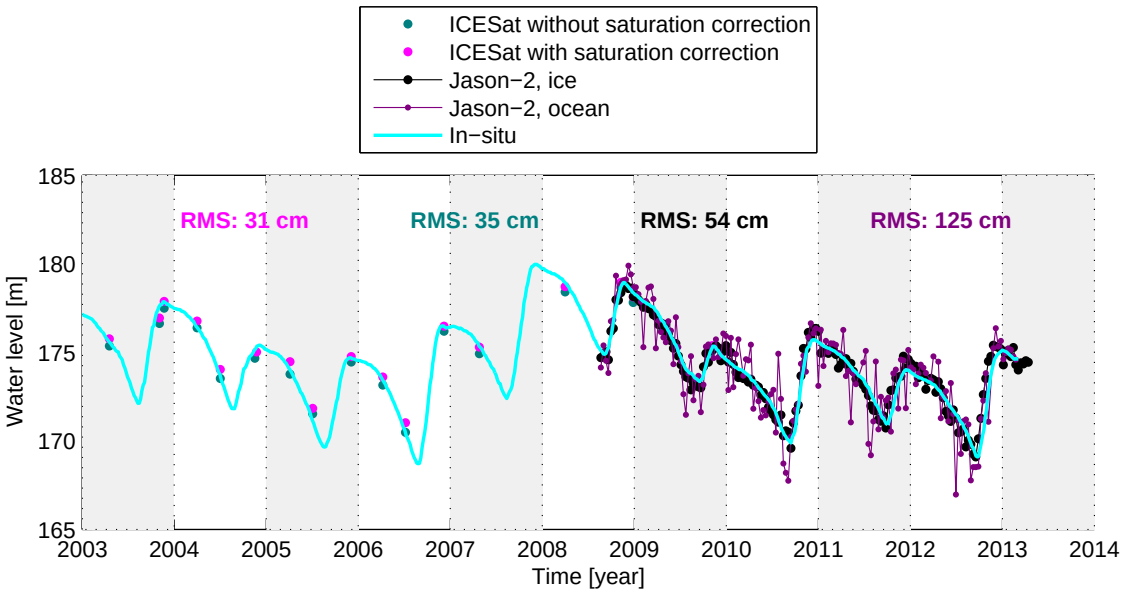

Figure 5.5: *Water level variations of Nasser lake from Jason-2, ICESat and in-situ gauge data*

ICESat

We also derived the water level of Nasser lake from GLA14 data of the ICESat mission. All available ICESat data across the lake, i.e. 19 GLAS laser transects, have been analyzed. After removing a bias of 31 cm between the satellite and in-situ gauge water level in the validation process, an RMS of 31 cm was achieved after implementing the saturation corrections. The RMS of water level without using the saturation correction is 35 cm after removing a 23 cm bias. Figure 5.5 shows the results of ICESat data analysis over Nasser lake.

Jason-2
Furthermore, the gdr-d data of the Poseidon3 altimeter mounted on the Jason-2 mission, have been analyzed from July 2008 to June 2014. Poseidon3 is using the ocean and ice1 retrackers operationally. The RMS of the water level from the ice1 retracker, after removing the bias (90 cm), is 54 cm relative to in-situ gauge. The ocean retracker has an RMS of 125 cm. Figure 5.5 includes the result of Jason-2 water level estimation for Nasser lake.

5.1.3 Urmia lake

Envisat
We analyzed the GDR and SGDR RA-2 data of Envisat mission from May 2002 to April 2012. Envisat covers Urmia lake via two tracks: track 371 (ascending) and track 178 (descending). From the GDR data we derived water level using on-board range measurements (from ice-1, ice-2, sea ice and ocean) for ascending and descending track separately. We found out that there is no bias or systematic error between the result of ascending and descending tracks for the on-board retrackers. An RMS of 38 cm was obtained from comparison of the ascending and descending track derived water level. Then we combined the ascending and descending water level into a unified time series. Figure 5.6 (upper panel) shows the water level from the ascending and descending tracks separately. The lower panel of this figure represents the unified time series.

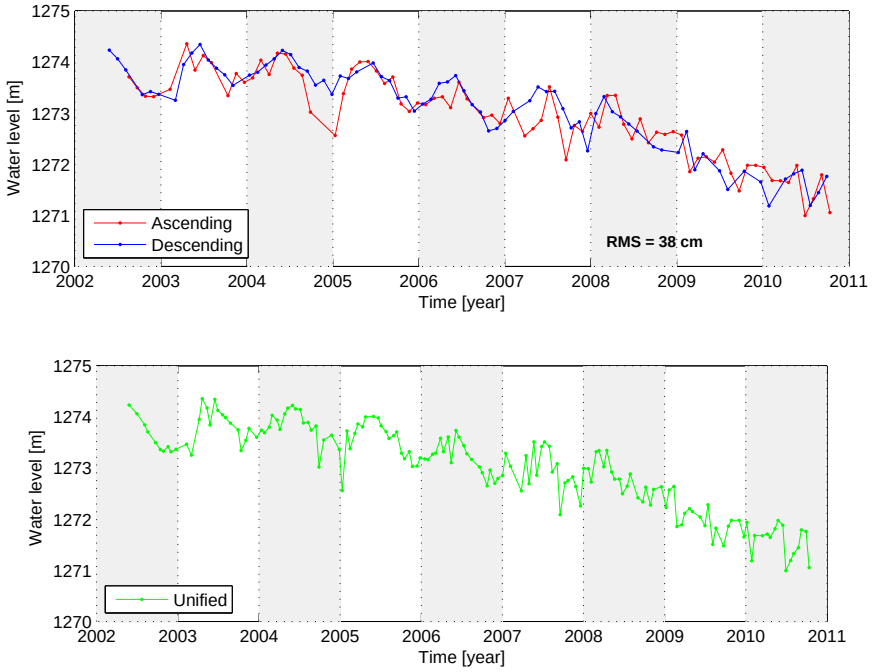

Figure 5.6: *Unified water level time series of Urmia lake from the ascending and descending tracks of Envisat based on the ice-1 on-board retracker*

We validated all unified water level time series against available in-situ gauge data. Figure 5.7 summarizes the result of on-board retracker assessment in terms of RMS with respect to the

in-situ gauge data. The minimum RMS, 26 cm, belongs to ice-1 retracker after removing a 16 cm bias.

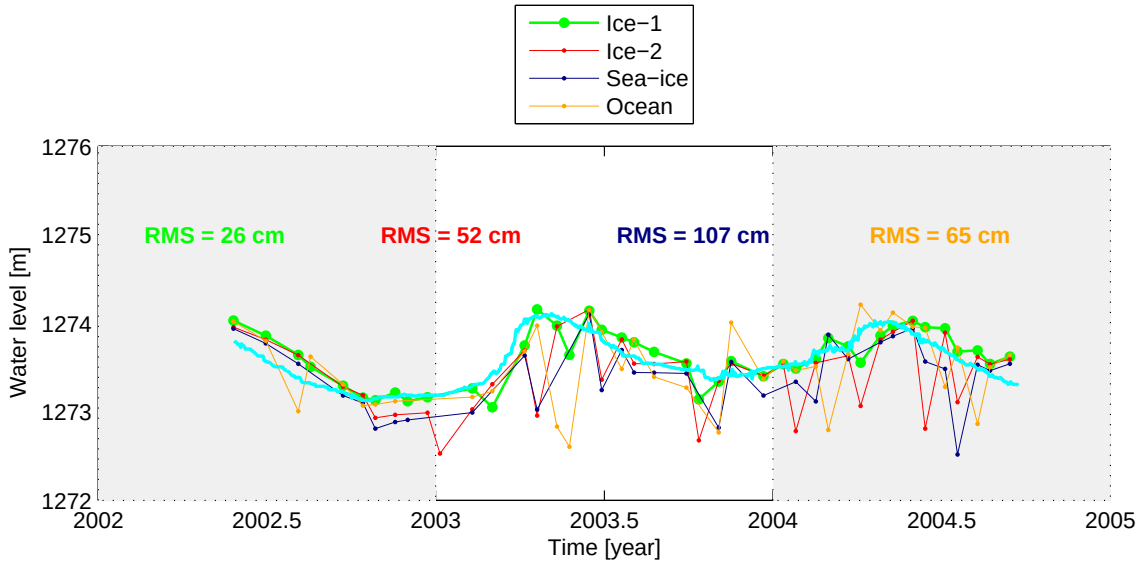

Figure 5.7: *Water level variations of Urmia lake from Envisat on-board retrackers and in-situ gauge data*

We then applied our retracking algorithms on full- and sub-waveforms, i.e. using SGDR data for ascending and descending tracks separately. Then the retracked water levels from both tracks have been combined to construct one time series for the lake. The results of these analyses are summarized in table 5.3. The minimum RMS is 18 cm, after removing a 1.9 m bias, if we retrack the first detected sub-waveforms. So we have 8 cm improvement in water level estimation if we retrack the waveform instead of using on-board range measurements. Figure 5.8 compares the water level from the best on-board retracker and from the best scenario according to our algorithm.

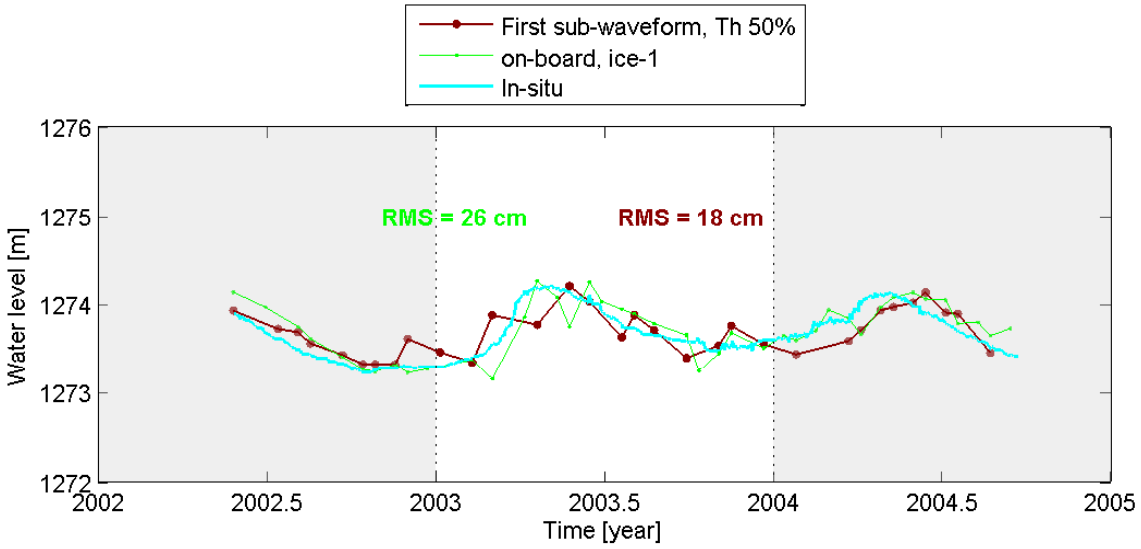

Figure 5.8: *Water level variations of Urmia lake from Envisat waveform retracking and in-situ gauge data*

Table 5.3: RMS (cm)/N *of water level and percentage of observations from different retrackers based on Envisat data (Urmia lake)*

retracker	full-waveform	sub-waveform		
		first	mean-all	min-res
Ice-1	26/84	–	–	–
Ice-2	52/85	–	–	–
Sea-ice	107/91	–	–	–
Ocean	65/88	–	–	–
5β-parameters	172/85	22/84	36/78	38/76
OCOG	41/83	22/95	36/76	25/80
Threshold 10%	23/87	24/81	26/86	25/84
Threshold 20%	23/80	24/76	26/87	28/86
Threshold 50%	22/95	**18/86**	22/88	29/84

CryoSat-2 LRM

We also used data from CryoSat-2 LRM on-board retracker from May 2010 to end of 2013. An RMS of 32 cm, after removing a 57 cm bias, was achieved from this mode of CryoSat-2 relative to in-situ gauge data. It must be noted that this RMS is only based on 6 measurements that is statistically not convincing to assess the CryoSat-2 LRM.

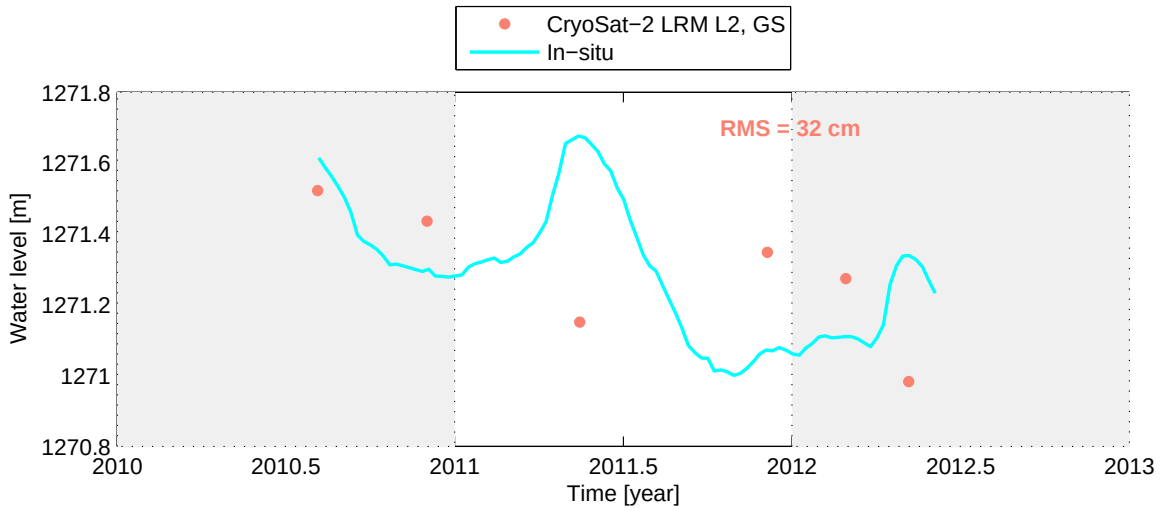

Figure 5.9: *Water level variations of Urmia lake from CryoSat-2* LRM *on-board retrackers and in-situ gauge data*

5.1.4 Qinghai lake

CryoSat-2 LRM
Qinghai lake is observed by different altimetry missions. We study the water level variations from CryoSat-2 LRM, Envisat and ICESat missions. Our main interest was to assess the capability of CryoSat-2 LRM for inland altimetry.

We derived the water level from the on-board range measurements of CryoSat-2 mission based on the GS retracker. The time series comparison (in figure 5.10) with in-situ gauge data leads to an RMS of 26 cm after removing a 51 cm bias.

We also retracked the water level by post-processing full- and sub-waveforms with different retracking algorithms. The retracked water level from all scenarios were compared with the in-situ gauge data to find the best retracking scenario. After removing the bias (1.52 m), the minimum RMS, 15 cm, belongs to the threshold retracker with different threshold values if we retrack all of the sub-waveforms in a given waveform. In the retracking process only the 5β-parameters model can retrack the full-waveforms and provide reliable and precise estimate of the lake water level. The RMS of water level is 20 cm from this retracker relative to in-situ gauge data.

Qinghai lake, located on the Tibetan Plateau at an altitude of 3193 m (Zhang et al., 2011a), is covered with snow and ice during the cold seasons, i.e. from October to April (Zhang et al., 2014). The snow and ice coverage can affect the performance of the retrackers. It is worth to mention that the β-parameters retracker has been designed to retrack waveforms over continental ice sheets, so it is expected that it works well over such an icy lake. Figure 5.10 compares the water level from the on-board range measurements of CryoSat-2 with the best retracking scenario, i.e. mean-all sub-waveform retracked with threshold 10%.

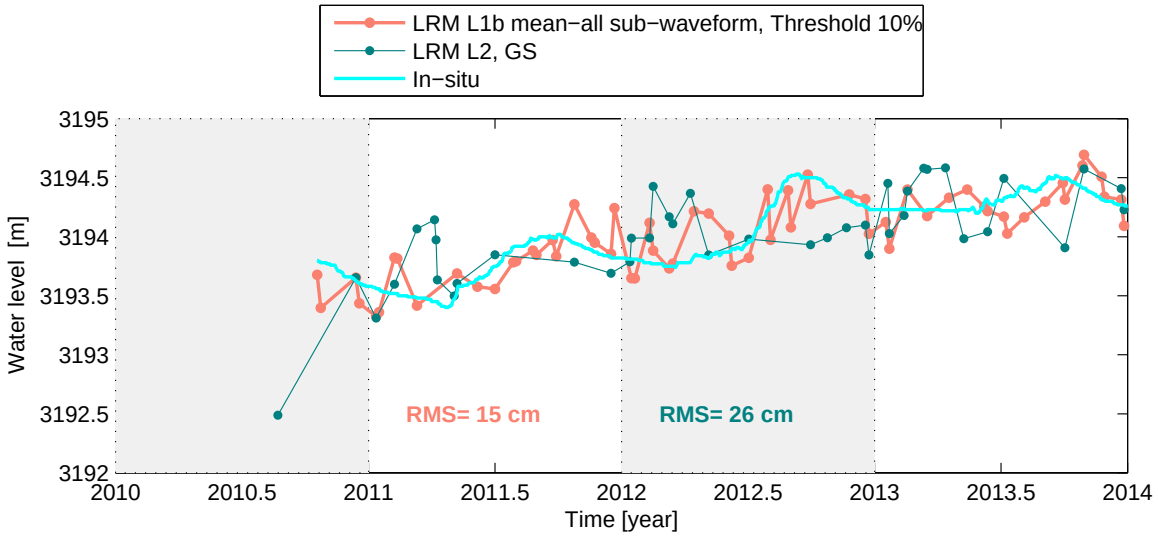

Figure 5.10: *Water level variations of Qinghai lake from CryoSat-2* LRM *and in-situ gauge data*

Table 5.4: RMS (cm)/N *of water level and percentage of observations from different retrackers based on CryoSat-2* LRM *data (Qinghai lake)*

retracker	full-waveform	sub-waveform		
		first	mean-all	min-res
GS	26/78	–	–	–
5β-parameters	**20/81**	18/86	54/63	70/68
OCOG	150/97	19/85	46/71	70/57
Threshold 10%	178/98	**15/71**	**15/75**	41/79
Threshold 20%	182/94	**18/86**	**15/75**	42/67
Threshold 50%	192/97	18/88	**15/73**	45/62

Envisat

The RA-2 SGDR and GDR data of the Envisat mission have been analyzed too. An ascending track (track 240) and a descending track (track 276) have been selected over the lake. We derived the water level of the lake from the on-board range measurements, i.e. GDR data, for the ascending and descending tracks separately for each of the on-board retrackers. We found that there is no bias or systematic error between the water level from these two tracks. We obtained an RMS of 19 cm from comparison of the ascending and descending track water level time series (figure 5.11 upper panel). After removing outliers, the ascending and descending water level time series were combined to define a unique water level time series based on each on-board retracker. The on-board water level time series were compared with the in-situ gauge data. We found that the ice-1 retracker (after correcting a 2.1 m bias) provides the water level with minimum RMS, 10 cm. Figure 5.12 shows the performance of all on-board retrackers of Envisat.

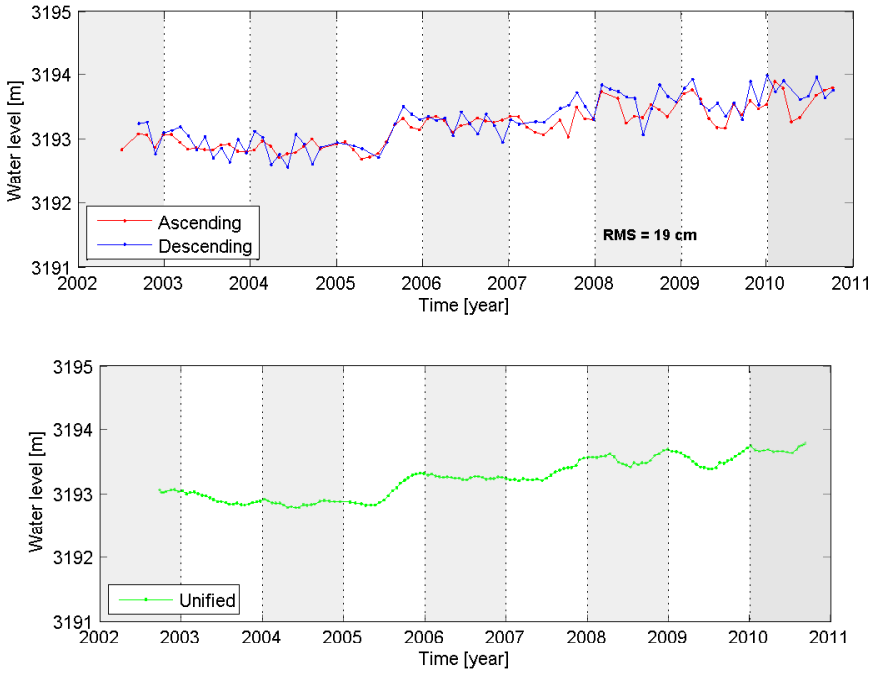

Figure 5.11: *Unified water level time series of Qinghai lake from the ascending and descending tracks of Envisat based on the ice-1 on-board retracker*

Furthermore, the waveforms included in the SGDR data were considered as full- and sub-waveform and retracked with different retrackers (table 3.1). We retracked the waveform of ascending and descending tracks separately. The retracked ascending and descending water level time series after outliers rejection were combined to create a single time series. After the validation of all scenarios we found that the 5β-parameters and OCOG retrackers provide the minimum RMS of 11 cm if we retrack the first sub-waveforms in a given waveform. The bias of this scenario is 1.95 m before calculating the RMS. The result of the Envisat waveform retracking are summarized in table 5.5. Figure 5.13 compares the water level from the best on-board and post-processing retrackers for Envisat.

Table 5.5: RMS (cm)/N *of water level and percentage of observations from different retrackers based on Envisat data (Qinghai lake)*

retracker	full-waveform	sub-waveform		
		first	mean-all	min-res
Ice-1	**10/90**	–	–	–
Ice-2	17/88	–	–	–
Sea-ice	15/77	–	–	–
Ocean	22/87	–	–	–
5β-parameters	110/70	**11/86**	28/68	47/67
OCOG	26/92	**11/73**	28/73	54/89
Threshold 10%	16/98	13/93	15/95	24/75
Threshold 20%	18/100	14/92	14/94	23/65
Threshold 50%	13/65	13/94	16/83	24/92

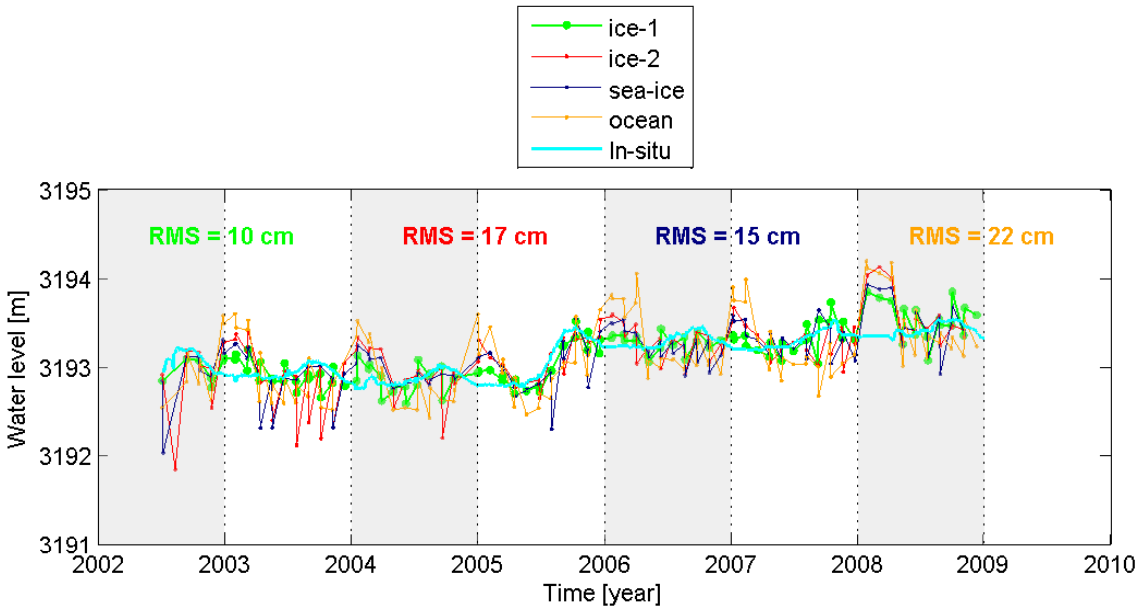

Figure 5.12: *Water level variations of Qinghai lake from Envisat on-board retrackers and in-situ gauge data*

ICESat

Besides CryoSat-2 and Envisat we analyzed GLAS GLA14 data of the ICESat mission. To this end, we selected all available laser campaigns of ICESat, i.e. 17 transects, across the lake. The result of ICESat data analysis are shown in figure 5.13. Without using the saturation correction we achieved 7 cm RMS for the water level with respect to the in-situ gauge data. If we correct the ranges due to the saturation effect the RMS would improve to 6 cm. A bias of 1.1 m was

removed before calculating the RMS. Figure 5.13 shows the performance of Envisat and ICESat missions to determine water level variations of Qinghai lake.

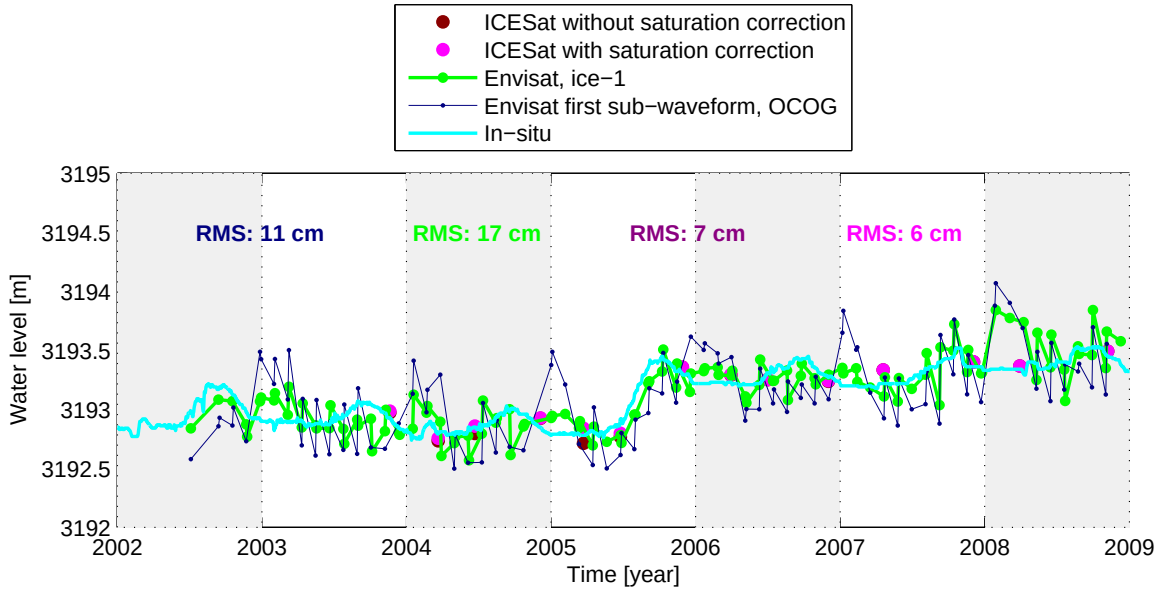

Figure 5.13: *Water level variations of Qinghai lake from Envisat, ICESat and in-situ gauge data*

5.2 River water level variations

5.2.1 Danube river

Three sections of the Danube river shown with red numbered triangles on figure 4.5 have been studied from Envisat, SARAL and Jason-2 altimetry missions. Two of these sections (1 and 2) are close to each other. The distance between these two sections is about 4 km where Envisat and SARAL cross the river. The river width at these locations is about 500 m and 450 m respectively. Section 3, with a 530 m width, is crossed by Jason-2; it is 72 km away from the other sections.

Envisat: track 0308
At location 1 (the southernmost red triangle on figure 4.5) the river width is about 500 m but the satellite tracks are not perpendicular to the river and intersect the river at steep angles. In each pass, the satellite measures a profile about 1500 m over the river. According to equation (2.9) the footprint size of Envisat here is about 2000 m with along-track spacing of about 300 m (Sulistioadi et al., 2015). So the footprints overlap and there are about 3–4 observations for each satellite over pass.

At this cross section, we analyzed the GDR and SGDR data of Envisat (track 0308). First, the water level of the river was defined from on-board range measurements according to the ocean, ice-1, ice-2 and sea-ice retrackers. The water level derived from each on-board retracker was validated against the in-situ gauge data of Baja station. After removing biases range from 15 cm to 77 cm we found that the ice-1, ice-2 and sea-ice retrackers with an RMS of about 48 –49 cm are showing the same performance, better than the ocean retracker with 52 cm RMS.

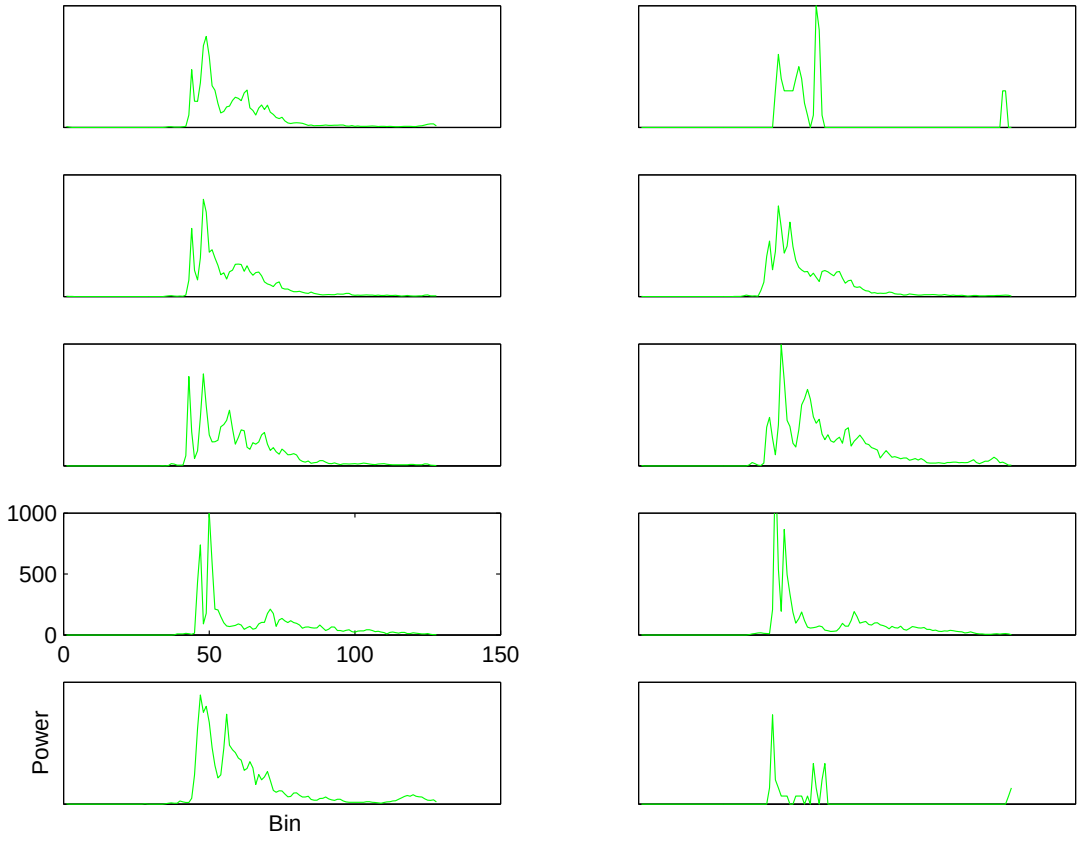

Figure 5.14: *Envisat waveform variations over Danube river, 20 January 2009*

Then we retracked the full and sub-waveforms, the results of which, are included in table 5.6. This table also shows the comparison between the results of the best on-board retracker, i.e. ice-1, and that of the post processed waveforms. The minimum RMS of 47 cm is obtained from the sub-waveform (the first and min-res sub-waveform) retracked by threshold 20% retracker, after removing a bias of 2.76 m. As one can see from this table, except for 5β-parameters all retrackers have a smaller RMS in sub-waveform than in the full-waveform retracking. Envisat waveforms over narrow rivers like the Danube are highly contaminated, i.e. the waveforms have multiple-peaks. As an example, a number of Envisat multi-peak waveforms were plotted in figure 5.14. Therefore one can expect that for such corrupted waveforms the sub-waveform outperforms the full-waveform in the retracking process.

Table 5.6: RMS (cm)/N *of water level and percentage of observations from different retrackers based based on Envisat data, track 0308 (Danube river)*

retracker	full-waveform	sub-waveform		
		first	mean-all	min-res
Ice-1	**48/98**	–	–	–
Ice-2	49/96	–	–	–
Sea-ice	48/97	–	–	–
Ocean	52/95	–	–	–
5β-parameters	**47/98**	48/98	63/98	58/98
OCOG	94/100	48/97	54/98	48/98
Threshold 10%	93/99	49/97	49/97	49/96
Threshold 20%	95/100	**47/98**	48/97	**47/98**
Threshold 50%	98/97	49/96	49/98	50/97

SARAL: track 0616

At the same location of this river we analyzed SARAL/Altika 40 Hz SGDR data from track 0616. SARAL has the same ground track as Envisat. The footprint size of SARAL at this location is about 2000 m, equation(2.9), with an along-track spacing of about 170 m (Saikrishnaveni et al., 2016). So the footprint overlap. Like Envisat, SARAL senses a 1500 m profile of the river in each satellite pass. Therefore, there are about 7–9 observations over the river per pass.

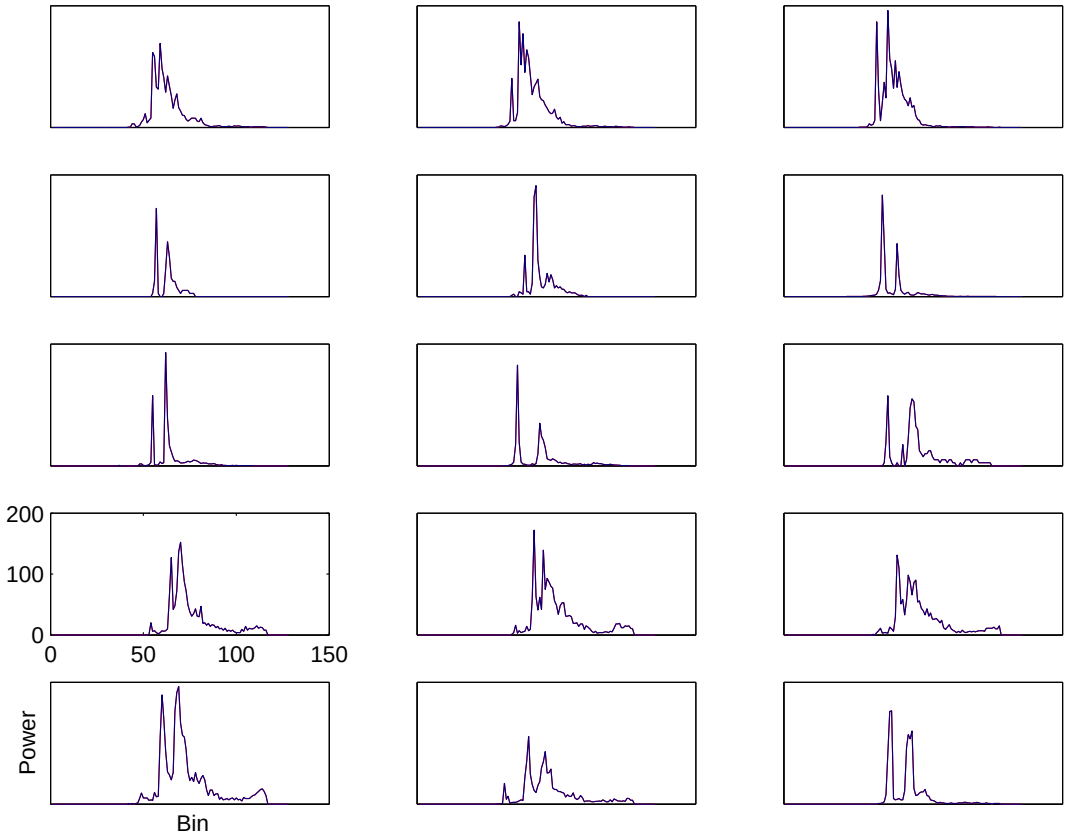

Figure 5.15: *SARAL (track 0616) waveform variations over Danube river, 25 July 2013*

The water level was first derived from the 4 on-board retrackers and compared with the in-situ gauge data. After removing a bias of 20– 70 cm we found that ice-1 has a minimum RMS of 55 cm among the on-board retrackers. We retracked the water level of the river from full- and sub-waveform retracking. Table 5.7 includes the results of the SARAL waveform retracking in terms of water level RMS with respect to the in-situ gauge data. Threshold 10% and 20%, after removing a bias of 2.75 m, have the minimum RMS of 54 cm if we retrack the first detected sub-waveforms. Threshold 10% has the same RMS if we consider all of the sub-waveforms in a given waveform. According to this table the sub-waveform retracking outperforms the full-waveform retracking almost for all of the retrackers but minimal improvement relative to ice-1. Analyzing the waveform of SARAL over this river section shows that most of the waveforms are multi-peaks that leads to a better performance for the sub-waveform retracking than that of the full-waveform retracking. Figure 5.15 represents a number of multi-peak waveforms over this section of Danube river. We plotted the water level of the river at this location from Envisat and SARAL data in figure 5.16.

Table 5.7: RMS (cm)/N *of water level and percentage of observations from different retrackers based on* SARAL *data, track 0616 (Danube river)*

retracker	full-waveform	sub-waveform		
		first	mean-all	min-res
Ice-1	**55/94**	–	–	–
Ice-2	60/95	–	–	–
Sea-ice	59/96	–	–	–
Ocean	76/66	–	–	–
5β-parameters	57/94	55/93	57/94	58/93
OCOG	84/93	55/92	57/94	57/94
Threshold 10%	86/94	**54/94**	**54/94**	57/92
Threshold 20%	86/92	**54/94**	55/93	57/94
Threshold 50%	80/94	56/93	56/92	58/94

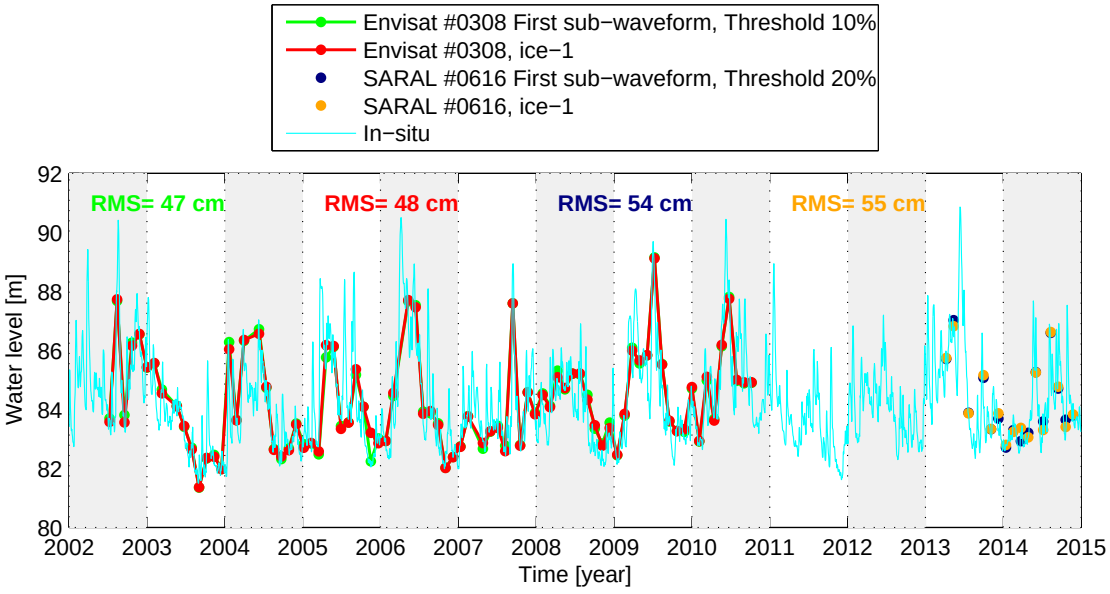

Figure 5.16: *Water level variations of Danube river from Envisat,* SARAL *and in-situ gauge data*

SARAL: track 0657

At the second location, about 3.5 km away from the first location, the water level of the river was only derived from the 40 Hz SGDR data of SARAL/Altika (track 0657). SARAL, with a footprint size of about 2000 m and 170 m along-track spacing measures a 700 m profile of the river in each pass. With overlapping of the footprints, there are about 4 observation in each satellite over pass.

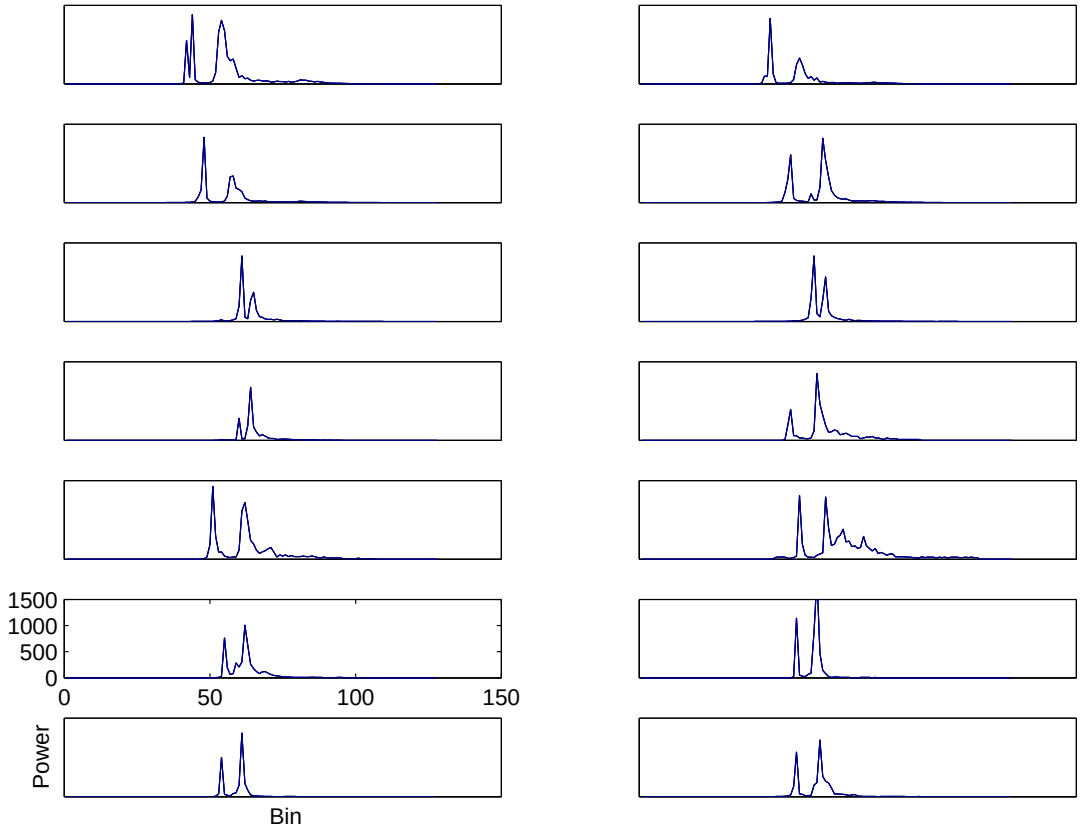

Figure 5.17: SARAL *(track 0657) waveform variations over Danube river, 22 June 2013*

Table 5.8: RMS (cm)/N *of water level and percentage of observations from retrackers based on* SARAL *data, track 0657 (Danube river)*

retracker	full-waveform	sub-waveform		
		first	mean-all	min-res
Ice-1	48/93	–	–	–
Ice-2	**46/94**	–	–	–
Sea-ice	49/92	–	–	–
Ocean	76/63	–	–	–
5β-parameters	68/94	51/94	50/94	53/94
OCOG	78/93	51/93	50/93	54/92
Threshold 10%	80/92	48/94	**46/94**	**41/94**
Threshold 20%	71/93	48/92	47/93	49/93
Threshold 50%	73/94	52/94	50/94	56/94

Four water level time series derived from the SARAL on-board retrackers have been compared with the in-situ gauge data from Baja station located at 8.5 km distance from the satellite ground tracks. The minimum RMS, 46 cm, from the on-board retracker is obtained from the ice-2 retracker. The ice-1 and sea-ice have the same RMS of 49 cm. The on-board retracker have biases of 23 cm–1.39 m but they have been eliminated before calculating the RMS.

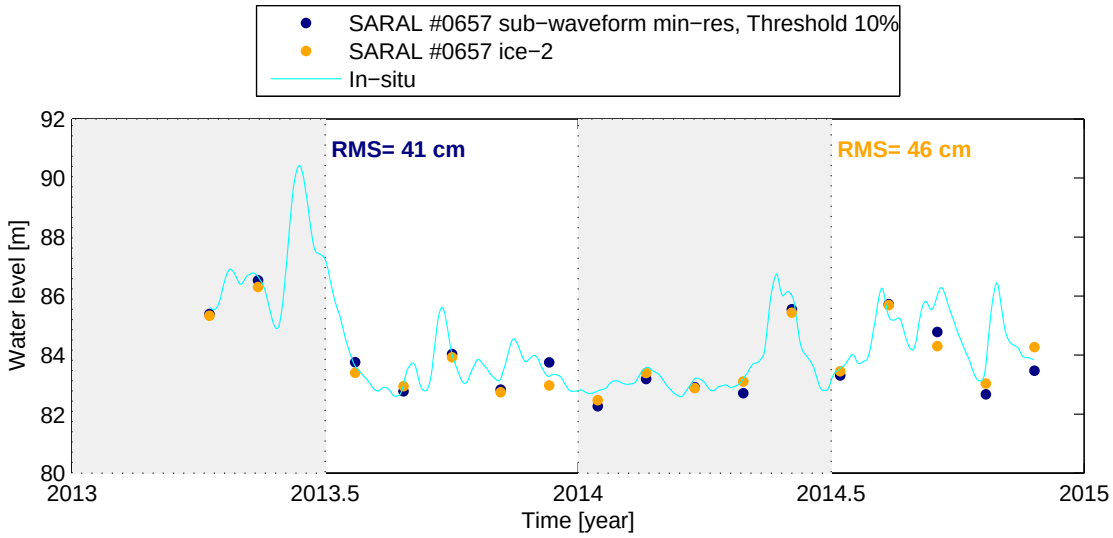

Figure 5.18: *Water level variations of Danube river from* SARAL *and in-situ gauge data*

At this location we defined the water level variations from retracking the waveforms with the retracking algorithms mentioned in table 3.1. The retracked water level from each algorithm was compared with the in-situ gauge data. The result of these comparisons are summarized in table 5.8. After removing a 2.7 m bias, we have found that the sub-waveforms with the mini-

mum residual retracked by threshold 10% provides the minimum RMS 41 cm. From this table one can see that the sub-waveform outperforms the full-waveform in the retracking process because the majority of the waveforms are multi-peaks (for instance figure 5.17). This table also shows that the results of sub-waveform retracking are somewhat better than that of the on-board retracking algorithms. Figure 5.18 compares the best on-board retracker with the best post processing retracking scenario.

Jason-2: track 0237
At the third location (shown on figure 4.5) 20 Hz sgdr_d data of Jason-2 mission were analyzed. Jason-2 with a footprint size of 3300 m (according to equation (2.9)) and along-track spacing of about 300 m (Jacobs et al., 2010) senses a 750 m profile of the river. Indeed the footprints overly each other and there are 2-3 observations per pass.

The Poseidon-3 altimeter carried by Jason-2 satellite operationally uses ice-1 and ocean retrackers to do on-board measurements. At this location of Danube river we used the on-board ranges from only the ice-1 retracker because the ocean retracker did not provide qualified ranges over the river. In the sgdr_d data base of this mission there are not ranges from the ocean retracker for most of the epochs. So we excluded this on-board retracker from further data analysis. The water level of the river derived from ice-1 retracker has an RMS of 50 cm with respect to in-situ gauge data of Dunaföldvár station (after removing a bias of 1.9 m).

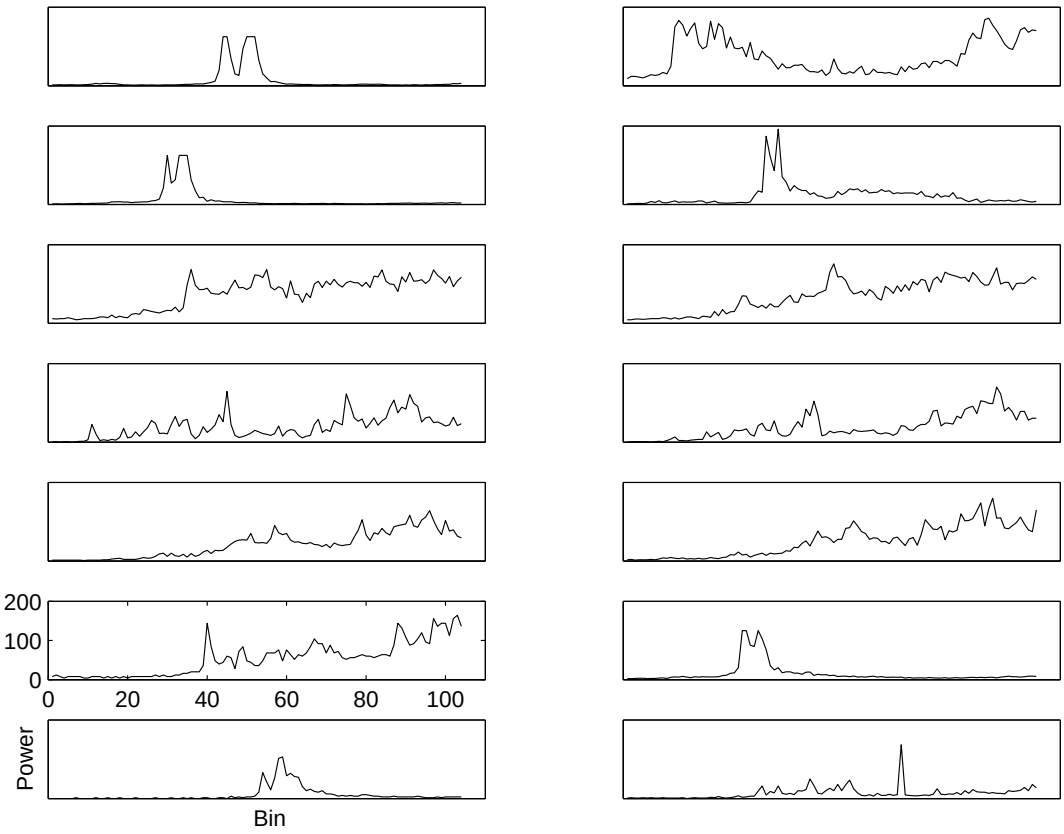

Figure 5.19: *Jason-2 (track 0237) waveform variations over Danube river, 19 March 2010*

Table 5.9: RMS (cm)/N *of water level and percentage of observations from different retrackers based on Jason-2 sgdr-d data, track 0237 (Danube river)*

retracker	full-waveform	sub-waveform		
		first	mean-all	min-res
Ice-1	50/81	–	–	–
5β-parameters	92/85	89/87	68/86	67/85
OCOG	138/84	89/87	59/85	58/85
Threshold 10%	108/72	88/87	**49/86**	57/85
Threshold 20%	109/72	90/88	52/86	59/89
Threshold 50%	93/85	87/86	53/86	54/89

At the same location of the river we retracked the waveforms of this mission to study the water level variations and to compare with those derived from the on-board range measurements. The retracking results are summarized in table 5.9. According to this table we arrive at a 49 cm RMS if we retrack all of the sub-waveforms in a given waveform with threshold 10% retracker, after deleting a 4.7 m bias. From this table one can find that the RMS from the sub-waveform retracking is smaller than that of the full-waveform retracking but marginally better than that of the ice-1. Since the waveforms are mostly corrupted (for example figure 5.19) one can expect a better performance for the sub-waveform retracking than the full-waveform retracking. Figure 5.20 shows the retracked water level from mean-all sub-waveform retracked with the threshold 10%. The water level from the ice-1 on-board retracker is also included in this figure.

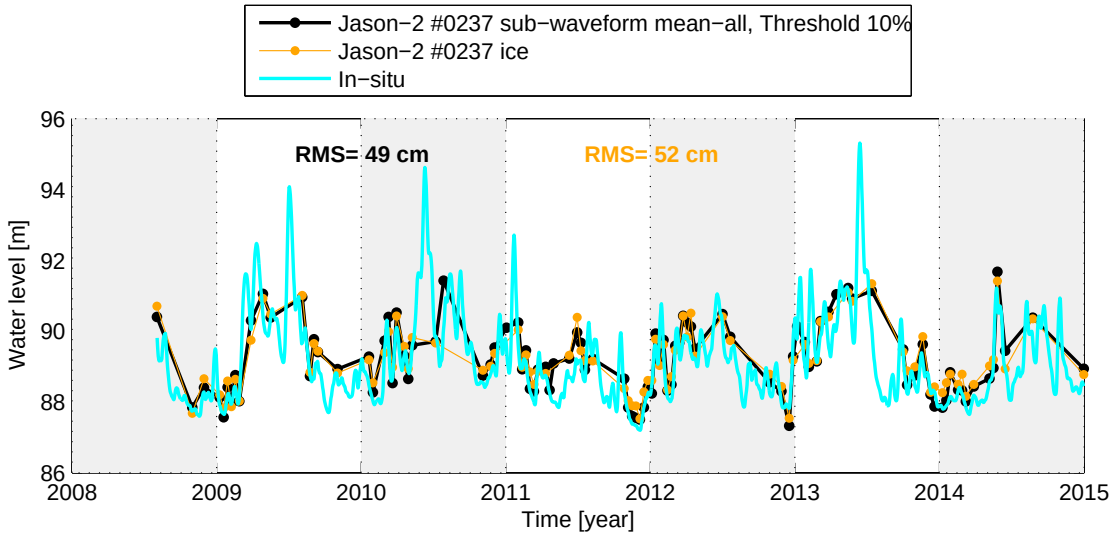

Figure 5.20: *Water level variations of Danube river from Jason-2 and in-situ gauge data*

According to figures 5.14, 5.15, 5.17 and 5.19 waveforms are highly contaminated over the river. To keep more valid observations, we retrack all of the waveforms (for all missions) and retrieved water level. If a number of waveforms do not lead to a valid water height then in the outliers rejection the outlier heights are deleted from the water level time series.

Chapter 6

Discussion, summary and conclusion

6.1 Discussion

6.1.1 Neagh lake

Over Neagh lake we analyzed the water level from the missions CryoSat-2 (SAR mode), Envisat and ICESat. The numerical results of our analysis were summarized in table 5.1.

CryoSat-2 SAR mode
The water level RMS from the CryoSat-2 SAR mode on-board retracker, i.e. GS retracker, is 24 cm. In the case of waveform retracking, the RMS would be 15 cm which is achieved from, e.g. a threshold 10% retracker, if we retrack all of the meaningful sub-waveforms inside a given SAR waveform. The number of valid observations involved in the estimation process from the on-board retracker is 88% but from our retracking scenarios, e.g. from mean-all sub-waveform retracked by threshold 10%, is 92%. Therefore several of our retracking scenarios outperform the on-board retracker for the CryoSat-2 SAR mode, because it provides the smaller RMS using higher percentage of observations involved in the water level estimation.

If we compare the results from the sub-waveform retracking scenarios in table 5.1 we find that the mean-all sub-waveform scenarios provide the smaller RMS using almost the same percentage of observations. Therefore they are showing a better performance than the other scenarios. The first sub-waveforms retracked with SAMOSA3 algorithm has the minimum RMS, i.e. 15 cm, but it only involves 88% of observations to estimate the water level. According to table 5.1 the RMS of water level obtained from the min-res sub-waveform scenarios are higher than that of mean-all sub-waveform scenarios.

Selecting a proper sub-waveform in a given waveform to be retracked in the min-res sub-waveform scenarios depends on the model that we used for outlier detection. From figures 5.1 and 5.2 one can see that the water level of the lake has not a regular behavior. Therefore the model shown in equation (4.4) can not reflect the real behavior of the water level that affects on the optimized sub-waveform selection. From such a model the selected sub-waveforms are not necessarily optimized, which can lead to a higher RMS with respect to the mean-all sub-waveform scenarios. Selecting an optimized model to reflect the real behavior of the water level of a given target can itself be a subject for investigation that needs extra analysis and it is not an objective for us in this research.

Table 5.1 shows, except than OCOG retracker all retrackers are showing better performance than the on-board retracker for CryoSat-2 SAR mode. They have the smaller RMS and higher percentage of observations than that of the on-board retracker. According to this table, for

CryoSat-2, several of our post-processing retracking scenarios fulfill the objective mentioned in the introduction, i.e. by retracking we have estimated more accurate water level with a higher percentage of observations than what we can get from the on-board retracker. We have found several better post-processing scenarios than on-board scenarios but among them the mean-all sub-waveforms retracked with threshold 10% is the best retracking scenario to retrieve the water level variations of Neagh lake from the CryoSat-2 SAR mode measurements.

Envisat
Figure 5.2 and table 5.1 represent the results of the Envisat data analysis for all of the RA-2 on-board retrackers. They show that the ice-1 retracker follows the water level of the lake well, with a 19 cm RMS. That is the best on-board retracker for Envisat over this lake. It keeps only 61% of the Envisat observations inside the estimation process which is less than the CryoSat-2 SAR mode retracking scenarios do. However, a 19 cm RMS is a good performance for the Envisat on-board retrackers over such a small and shallow lake. One can easily and quickly derive the water level from this retracker using the RA-2 GDR data. Our results of Envisat data analysis are consistent with previous studies, e.g. (Frappart et al., 2006) and (Lee et al., 2011), that discussed the performance of Envisat ice-1 retracker over inland water bodies.

ICESat
Analysis of the ICESat GLAS data also shows a small RMS of 13 cm when we implement the waveform saturation correction. But the weak point of GLAS/ICESat derived water level is undersampling. Furthermore, due to laser characteristics, the performance of this mission depends on the weather condition. It only sensed the lake 3 times per year which is insufficient temporal resolution to reflect the real behavior of the lake water level variations. Undersampling status of ICESat was due to the failure of the first on-board laser system just a short time after the launch. After this failure the mission design team decided to activate alternately the two other laser systems which operated only three 33 days per year to increase the lifetime of the mission. From figure 5.3 one can find that the waveform saturation correction improves the quality of water level measurements over this lake. Regardless of the undersampling problem, under clear atmospheric conditions it can provide an RMS of a few centimeters.

6.1.2 Nasser lake

CryoSat-2 SARIn mode
A lake with such a complex river-like shape is a difficult object for satellite altimetry to sense accurately, but retracking techniques help to estimate the water level of the lake with a 25 cm RMS. The results of the CryoSat-2 SARIn mode data analysis in table 5.2 show that the on-board retracker, i.e. GS retracker, performs relatively well. With a 32 cm RMS it outperforms the Jason-2 and ICESat on-board retrackers. Retracking the SARIn mode waveforms leads to better results. The full-waveform retracked with the threshold 50% provides an RMS of 25 cm which is a promising result for the CryoSat-2 SARIn mode over such a difficult target. It is the best retracking scenario for the full-waveform retracking. The internal comparison of the sub-waveform retracking scenarios indicates that retracking the mean-all sub-waveform scenarios with an RMS of 28 cm have better performance than the first sub-waveform and the min-res sub-waveform scenarios. There is a small difference (less than 5) between the percentage of valid observations involved to estimate the water level from the sub-waveform retracking scenarios. According to table 5.2 all retrackers (post-processing) except than the threshold 50% have better

results in the sub-waveform retracking (especially for the mean-all sub-waveform) than in the full-waveform retracking.

Jason-2
Jason-2 data analysis from the on-board retrackers over this lake shows that the ice-1 retracker performance (54 cm RMS) is much better than the ocean retracker. The ocean retracker has been designed to retrack the waveform over the ocean not over the inland water bodies. So it is usual that it can not retrack waveforms over a difficult object like Nasser lake.

ICESat
ICESat data analysis summarized in figure 5.5, indicates a smaller RMS with respect to the CryoSat-2 and Jason-2 on-board retrackers. However, the water level derived from these two missions is more qualified than that of the ICESat mission due to their sampling behavior. From figure 5.5 one can see the difference in sampling behavior between Jason-2 and ICESat missions. According to table 2.2 the repeat cycle of ICESat is 91 days. Furthermore the laser operation periods were controlled (decreased) deliberately to extend the lifetime which exacerbates the time resolution of this mission. There are only three water level measurements during a year. But Jason-2 with a 10 days repeat cycle covers the lake with sufficient temporal resolution.

Kleinherenbrink et al. (2014) studied water level variations of Nasser lake from SARIn mode data of CryoSat-2. They obtained an RMS of 30 cm for CryoSat-2 water level time series with respect to the water level derived from Jason-2. They evaluated the CryoSat-2 results against Jason-2. Although the temporal resolution of Jason-2 is better than that of CryoSat-2 over such a lake, Jason-2 derived water level is not a proper reference to evaluate the CryoSat-2 performance. It is better to do the evaluation against in-situ gauge data.

6.1.3 Urmia lake

We run our retracking algorithms over Envisat and CryoSat-2 LRM data to study water level variations of Urmia lake.
Envisat
The internal validation of Envisat results shows that the water level obtained from the ascending and descending tracks are consistent and there is no bias and systematic error between them. Figure 5.7 and table 5.3 summarized the on-board retrackers ability to reflect the water level behavior of this lake. According to the internal validation of the on-board retrackers the ice-1 retracker, with an RMS of 26 cm, performances better than the others.

Urmia lake is a proper object to highlight the necessity and effectiveness of waveform retracking. Without waveform retracking we achieved the water level plotted in figure 6.1 . According to this figure the water level obtained from the descending track diverged after 2008 which can not represent real water level behavior. This divergence issue is caused by signals reflected back from the land when the satellite is entering over the lake during the descending tracks. Figure 6.3 shows that the satellite is passing close to lake shoreline (descending tracks). Therefore there are complex responses to the radar pulses in this part of the lake that have led to such a time series in figure 6.1. If we only use on-board retracker we can not have a qualified water level even after the effort to remove the outliers. To escape from this divergence in the water level time series, we must exclude the whole upper part of the descending track that is not a

proper solution to have a qualified water level time series, because there are several valid measurements that belong to the water surface and it is better to involved them in the estimation process.

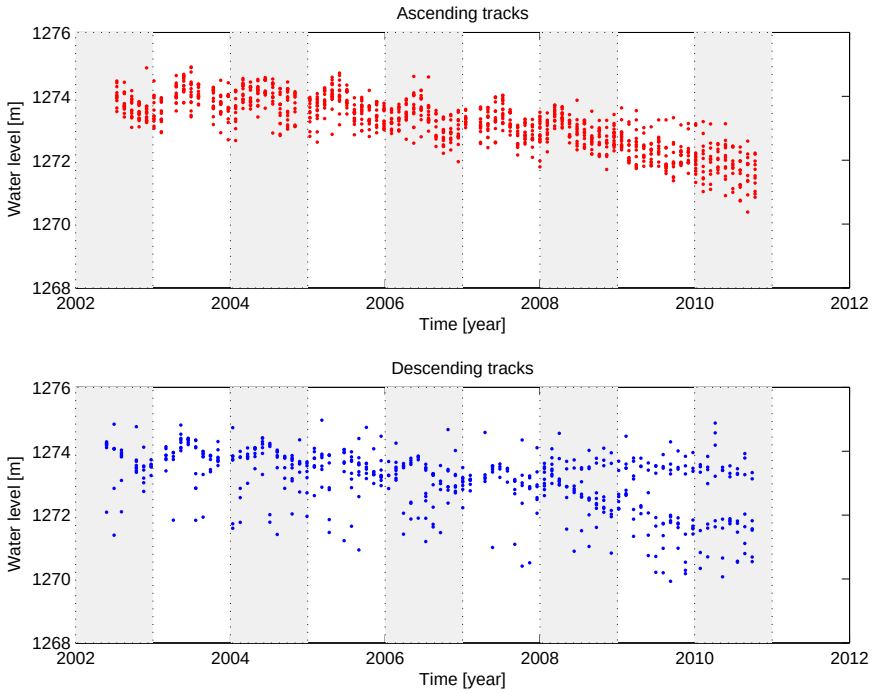

Figure 6.1: *Water level time series before the waveform retracking (Urmia lake)*

But retracking algorithm helps to solve this problem and to retrieve more valid observations over the lake surface. Waveform retracking leads to correction of many of the outlier-like water level measurements in figure 6.1 and to hold them inside the water level estimation process. Figure 6.2 represent the water level of the lake after the retracking. After the retracking, the separated water level from the ascending and descending tracks have been combined into a united water level time series for the lake. We run different retracking scenarios to define the water level of this lake. The first sub-waveform scenarios are showing better performance than the other scenarios. According to table 5.3 the first sub-waveform retracked with the threshold 50% is the best retracking scenario which has the minimum RMS of 18 cm. The threshold 50% with an RMS of 22 cm is showing a good performance to retrack the full-waveform and the mean-all sub-waveform over this lake.

CryoSat-2

The results of the CryoSat-2 LRM on-board retracker shown in figure 5.9 indicates apparently a poor performance for the CryoSat-2 but this can not reflect the real ability of the CryoSat-2, because they are just 6 measurements. After 2008 the lake started drying up and after 2010 the major southern part of the lake has completely been dried up. The unusual behavior (figure 6.1) in the water level time series of this lake (derived from Envisat) also relates to drying up of the lake.

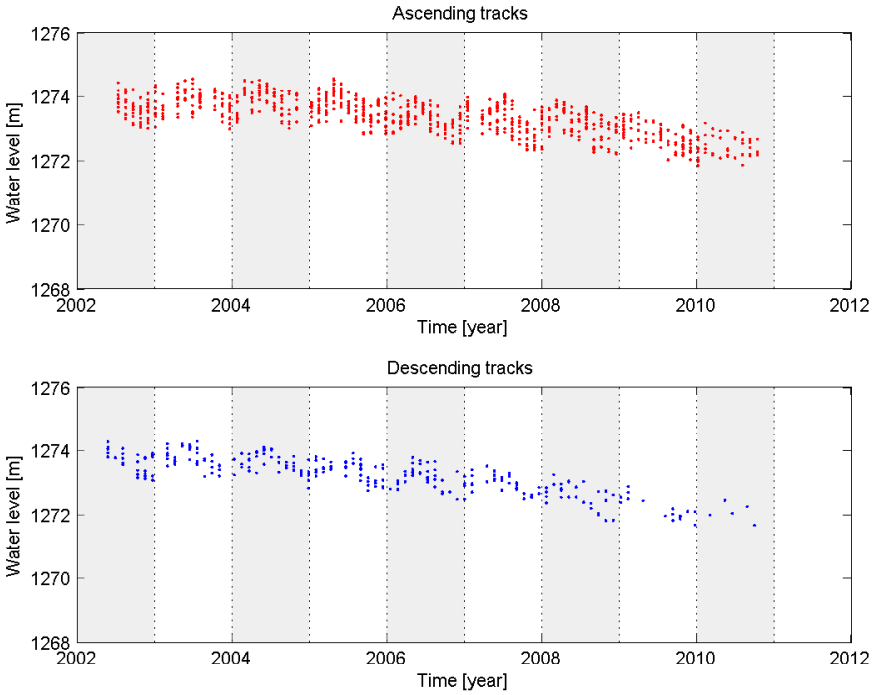

Figure 6.2: *Water level time series after the waveform retracking (Urmia lake)*

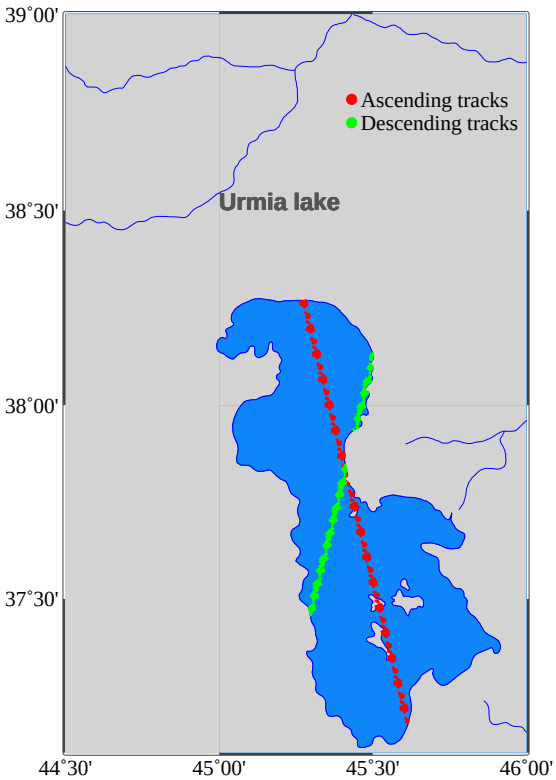

Figure 6.3: *Envisat sub-satellite points over Urmia lake from cycle 6 to cycle 113*

6.1.4 Qinghai lake

We evaluated the performance of CryoSat-2 LRM mode, Envisat and ICESat missions for water level monitoring of this lake with different retracking scenarios.

CryoSat-2 LRM mode

For the CryoSat-2 LRM, all retrackers (except than 5β-parameters) have an RMS higher than 100 cm in water level determination. The 5β-parameters retracker with an RMS of 20 cm is showing better performance than the on-board retracker, i.e. GS, retracker which has an RMS of 26 cm. Over this lake the sub-waveform retracking scenarios provide more precise water level than the full-waveform retracking scenarios would do. The first sub-waveform retracked by all of the retrackers has an RMS from 15 cm to 19 cm , i.e. better than the results of the on-board retracker. The threshold retracker is providing the smallest RMS with respect to the other retrackers for both the first and mean-all sub-waveforms. The mean-all sub-waveforms retracked with the threshold retracker (with different threshold values) are the best retracking scenarios to study water level of this lake from the CryoSat-2 LRM. The percentage of observations involved in water level determination for these scenarios are a little bit smaller (less than 5%) than that of the on-board retracker. This small difference in the percentage of observations does not play an important role. The smaller RMS is more important.

Envisat

We also implemented our retracking algorithms to analyze Envisat data. The results of the on-board retrackers summarized in figure 5.12 represent a good performance for them. Internal comparison between the on-board retracker with in-situ gauge data shows that the ice-1 retracker with an RMS of 10 cm has the best performance. A 10 cm RMS is a promising result for the on-board retracker, ice-1, because one can simply and quickly define the water level time series of the lake from this retracker. Several previously studies such as Frappart et al. (2006) and Lee et al. (2011) confirmed the performance of this retracker to monitor inland water bodies.

Figure 6.4 shows that there is about 50 to 70 cm anomaly (highlighted in this figure) between the water level derived from the on-board retrackers and from the in-situ gauge data early 2008 . The in-situ gauge represents almost a fixed level for water while all of the on-board retrackers are consistency showing different levels. This anomaly is due to freezing of the lake surface during the cold seasons. According to figure 6.4 one can see this issue (more or less) at the begin and end of each year. One can see this behavior for the water level from CryoSat-2 LRM but not as much as that from Envisat. As Zhang et al. (2011a) investigated, Qinghai lake is covered with ice from October to April. The ice coverage can affect on the altimeter's sampling. Remote sensing satellite image analysis would be very helpful to distinguish water from ice and snow in time and space. So one can use different retrackers for ice (or snow) and water surfaces.

We also retracked the waveforms of Envisat over this lake. The results, summarized in table 5.5, show that threshold 50% has the minimum RMS, 13 cm, when it retracks the full-waveforms. But it involves only 65% of the observations to determine the water level. All of the first sub-waveform retracking scenarios are showing a good performance with an RMS of 11 –14 cm. The mean-all sub-waveforms retracked with the threshold retracker with an RMS of 15 cm are also alternative scenarios for the lake.

For both missions, i.e. CryoSat-2 and Envisat the sub-waveform retracking with 11 cm–18 cm RMS outperforms the full-waveform retracking. The results of the sub-waveform retracking

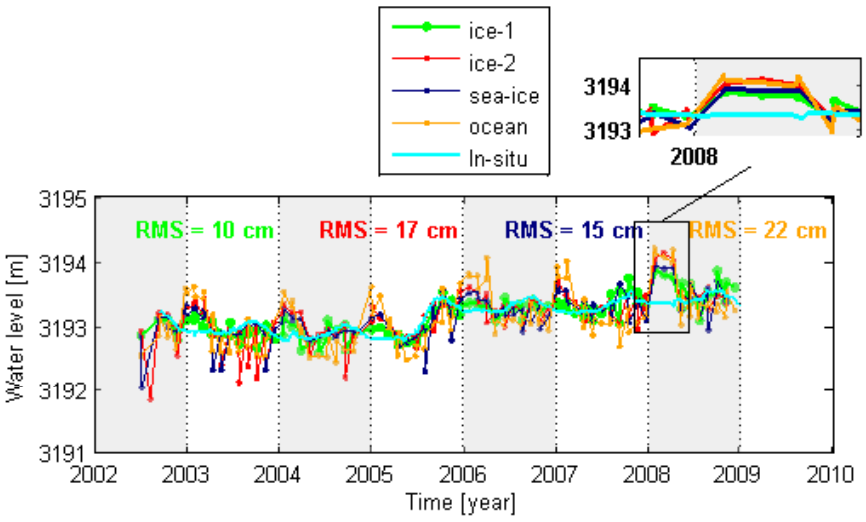

Figure 6.4: *Water level variations of Qinghai lake from Envisat on-board retrackers and in-situ gauge data*

(especially for the first and the mean-all sub-waveforms retracked with the threshold retracker) are consistent for both missions.

ICESat

The smallest RMS of the water level of Qinghai lake belongs to GLAS/ICESat mission. The water level RMS after implementing the saturation correction is 6 cm. That is the smallest RMS among all of the scenarios from all satellite missions used in the thesis over all study areas. The small RMS for GLAS/ICESat relates to its small footprint. Conventional and SAR altimeters have footprints in order of kilometers. But the footprint of ICESat is about 70 to 90 m which causes almost homogeneous responses from the illuminated surface. So the laser waveforms are hardly contaminated like SAR and conventional altimeter waveforms. Therefore the extracted ranges from the laser waveforms are more accurate especially if we apply the waveform saturation corrections. However providing only a small RMS in water level monitoring is not enough for an altimeter. The altimeter sampling behavior is also very important. ICESat, with the smallest RMS, has only three measurements per year that can not retrieve real change of water level of the lake. Figure 5.13 compares the performance of Envisat and ICESat missions in terms of the water level RMS.

6.1.5 Danube river

We have defined the water level of Danube river at three different sections from three different satellites to evaluate the performance of the satellites based on different retracking algorithms. It can also be a kind of evaluation for our retracking algorithms over rivers as well. The river widths at these locations are less than 1000 m. So it is a very challenging object for satellite

altimetry to monitor precisely. In fact over the wider rivers the performance of these altimeters would be better. In section 1, marked on figure 4.5, the water level was determined from Envisat and SARAL.

Envisat
The results of the Envisat data analysis are summarized in table 5.6 and figure 5.16. We compared the water level derived from the Envisat on-board retrackers with in-situ gauge. The ice-1 retracker with an RMS of 48 cm has the minimum RMS among the on-board retrackers.

The retracked water level accuracies are also included in table 5.6. The minimum RMS, 47 cm, belongs to the 5β-parameters retracker when it retracks the full-waveforms. The other retrackers have higher RMSes, about 95 cm, with the same percentage of observations. According to this table the sub-waveform retracking outperforms the full-waveform retracking (except for 5β-parameters retracker). Over a narrow river like Danube the Envisat with a footprint of about 2 km^2 has highly contaminated waveforms. The first sub-waveform scenarios show the same performance. The threshold retracker has almost the same results over all of the three kind of sub-waveform retracking scenarios.

SARAL/Altika
The results of the water level defined from the SARAL/Altika data over the same location (location 1) of this river are included in table 5.7 and figure 5.16. The internal comparison of the SARAL/Altika on-board retrackers shows that the ice-1 retracker is the best on-board retracker to determine the water level of the river. The 5β-parameters retracker has the minimum RMS of 57 cm if it retracks the full-waveforms, the same results as that of Envisat. All of the retrackers but the 5β-parameters have better performance over the sub-waveforms than over the full-waveforms. The best retracking scenarios are the first and mean-all sub-waveforms retracked by threshold 10% and 20% retrackers. The ice-1 retracker can also be the alternative option to define the water level of the river in this section.

If we compare the Envisat and SARAL/Altika results, 47 cm vs 54 cm RMS, we see that the performance of Envisat is better than SARAL/Altika.

At the second location shown on figure 4.5 (the river width is 540 m) we only analyzed the SARAL/Altika data. Table 5.8 and figure 5.18 represent this analysis. We have found that the ice-2 with an RMS of 46 cm is the best on-board retracker.

The numerical results of the waveform retracking from our algorithms indicate that the sub-waveform retracking scenarios are showing better performance than that of the full-waveform and that of the on-board retracking scenarios. The minimum RMS 41 cm belongs to the threshold 10% if it retracks the min-res sub-waveforms. The threshold 20% and 10% retrackers over the mean-all sub-waveforms have the same performance as the ice-2 retracker over the full-waveforms.

Jason-2
At the third location (figure 4.5) where the Danube river is 590 m wide, we run our retracking algorithms over the Jason-2 data. We found that the ice-1 algorithm with an RMS of 50 cm is the best on-board retracker. The results of the Jason-2 data analysis, shown in table 5.9, confirms that the sub-waveform retracking scenarios outperform the full-waveform retracking scenarios especially the mean-all sub-waveforms retracked with the threshold retracker. Figure 5.20 shows that the mean-all sub-waveforms retracked with threshold 10% is the best retracking scenario to retrieve the water level of the river.

The results of the retracking with our algorithms over three sections of Danube river show that the sub-waveform retracking scenarios provide the smaller RMS than the full-waveform waveform retracking scenarios. For altimeter satellites with a footprint of 2–3 km^2 over a narrow river like Danube with a width of 500–600 m, waveforms are highly contaminated. Figures 5.14, 5.15, 5.17 and 5.19 represent a number of these waveforms from different missions for three different sections of the river. Over such multi-peak waveforms, the sub-waveform leads to better results than the full-waveform in the retracking process.

6.2 Summary

A good quality of water level measurement is necessary to study climate change and hydrological cycle. In this thesis we quantified the quality of the water level estimated from satellite altimetry missions. We used two different types of altimeters: pulse-limited altimeters, e.g. Envisat, Jason-2, CryoSat-2 LRM, SARAL and beam-limited altimeters, e.g. ICESat, CryoSat-2 SAR and SARIn modes. We used on-board range measurements and ranges estimated from pot-processing the waveforms (waveform retracking) of these altimeters.

In the retracking a number of empirical and physical retracking algorithm have been employed. Waveforms have been considered as full and sub-waveforms in the retracking process. Three different strategies (the first, mean-all and min-res sub-waveforms) were used in the sub-waveform retracking. So we defined different retracking scenarios for each altimeter and each water body based on retracking algorithms and full and sub-waveforms.

We selected lakes Neagh, Nasser, Urmia and Qinghai, with different shapes, and sizes approximately from 400 km^2 to 2200 km^2, in different countries. Moreover we derived water level variations at different locations of Danube river in Hungary with the width of less than 600 m.

Every object was sensed at least by two satellites. The water level of each object was estimated from the on-board retrackers and from the post-processing waveforms with retrackers mentioned in table 3.1. These water level time series were validated against available in-situ gauge data to assess the accuracy of each altimeter satellite and retracking scenario for a given object.

It is worth to mention that for a given satellite altimeter there was a bias (shift) between the water level from the satellite and from the in-situ gauge data, because the in-situ gauge are usually referenced to a national or local elevation datum. The bias was defined as the difference between the mean water level form the satellite and in-situ gauge. There was also a bias between the water level obtained from different altimeter satellites, because altimeters use different elevation datum (different reference ellipsoids) in their measurements. Moreover for a given object and a given altimeter may exist a bias between the water level estimated from different retracking scenarios. These biases do not play an important role in our analysis because we compare the water defined from the satellite measurement with in-situ gauge data relatively. To that end, biases have been removed before the validation process.

Since the biases have been removed, instead of the *accuracy* we use the *precision* in our assessment. The precision is equivalent to the RMS between the water level from the satellite and from the in-situ gauge data. For a given altimeter, the smaller RMS the more precise the retracking scenario. The number of observations (observations-outliers) involved in estimating the water level of a given object is also important. Therefore we used both criteria, i.e. the water level

RMS and number of observations N involved in the estimation process, to evaluate the performance of each retracking scenario and consequently to assess the performance of each satellite altimetry mission.

6.3 Conclusion

Based on our analysis which includes different altimeters, retracking algorithms and waveforms (full and sub) we conclude that:

1. Waveform retracking is necessary to derive a qualified water level of inland water bodies from satellite altimetry data.
2. Waveform retracking leads to increase the number of valid observations in water level determination.
3. The quality of water level determination depends on the altimeter type, the retracking algorithm, shape and size of inland water bodies.
4. Results of waveform retracking (post-processing waveform) are more precise than those of on-board retrackers.
5. Over small or complex shape inland water bodies the sub-waveform retracking has better performance than the full-waveform retracking.
6. Ice coverage affects the performance of the retrackers in the full and sub-waveform retracking.
7. The threshold retracker has the best performance for pulse-limited and Doppler beam-limited altimeters.
8. The mean-all sub-waveform retracking provides more precise water level than that the first and min-res sub-waveforms do for small and complex shape lakes for all altimeter types.
9. Over narrow rivers the first and the mean-all sub-waveform retracking have almost the same performance.
10. The first sub-waveform retracking also leads to a precise water level and it can be used as an alternative of mean-all retracking scenario.
11. Since the min-res sub-waveform retracking depends on the models used to delete outliers, it is better to use the mean-all and the first sub-waveform retracking in water level determination. However it has a good performance over a few of study areas.
12. Doppler beam-limited (SAR) altimeters have better performance than pulse-limited altimeters.
13. For an inland water bodies without in-situ gauge data the mean-all sub-waveforms and full-waveforms retracked by the threshold retracker is recommended respectively.

14. A possible bias between water level from satellites and from in-situ gauge data must be removed before evaluation process.

Bibliography

Abshire, JB, Sun, X, Riris, H, Sirota, JM et al. (2005). Geoscience Laser Atimeter System (GLAS) on the ICESat mission: On-orbit measurement performance. *Geophysical Research Letters*, **32**(21):n/a. doi:10.1029/2005GL024028. L21S02.

Abulaitijiang, A, Andersen, OB and Stenseng, L (2015). Coastal sea level from inland CryoSat-2 interferometric SAR altimetry. *Geophys Res Lett*, **42**(6):1841–1847. doi:10.1002/2015GL063131.

AHADA (2016). Aswan High Dam Authority, Nasser lake in-situ gauge data. http://www.water-technology.net/projects/aswan-high-dam-nile-sudan-egypt, Last visit October 2016.

Altés, AB, Cornara, FP and Renard, M (2010). *Next Generation Gravity Mission (NGGM): Mission analysis report*. Tech. rep., NGGM-DEM-TEC-TNO-01, Deimos.

Anzenhofer, M, Shum, CK and Rentsch, M (1999). *Coastal altimetry and applications*. Tech. rep., Report No, 464, Ohio State University.

Asem, A, Mohebbi, F and Ahmadi, R (2012). Drought in Urmia lake, the largest natural habitat of brine shrimp Artemia. *World Aquaculture*, **43**(1):36–38.

AVISO (2016a). Jason-2 data. http://www.aviso.altimetry.fr/en/data.html, Last visit October 2016.

——— (2016b). RADAR characteristics. http://www.aviso.altimetry.fr/en, Last visit October 2016.

——— (2016c). SARAL data. http://www.aviso.altimetry.fr/en/data.html, Last visit October 2016.

Baghdadi, N, Lemarquand, N, Abdallah, H and Bailly, JS (2011). The relevance of GLAS/ICESat elevation data for the monitoring of river networks. *Remote Sensing*, **3**(4):708. doi:10.3390/rs3040708.

Barton, DK (1988). Modern radar system analysis. *Norwood, MA, Artech House, 1988, 607 p*, **1**.

Beckley, BD, Zelensky, NP, Holmes, SA, Lemoine, FG et al. (2010). Assessment of the Jason-2 extension to the Topex/Poseidon, Jason-1 sea-surface height time series for global mean sea level monitoring. *Marine Geodesy*, **33**(sup1):447–471. doi:10.1080/01490419.2010.491029.

Benveniste, J, Baker, S, Bombaci, O, Zeli, C et al. (2002). Envisat RA-2/MWR Product Handbook. *Frascati, Italy: Europea Space Agency*, (1.2).

BHWR (2016). Bureau of Hydrology and Water Resources , Qinghai lake in-situ gauge data. http://www.agrw.ir, Last visit, October 2016.

Biancamaria, S, Andreadis, KM, Durand, M, Clark, EA et al. (2010). Preliminary characterization of SWOT hydrology error budget and global capabilities. *Selected Topics in Applied Earth Observations and Remote Sensing, IEEE Journal of*, **3**(1):6–19. doi:10.1109/JSTARS.2009.2034614.

Biancamaria, S, Durand, M, Andreadis, K, Bates, P et al. (2011). Assimilation of virtual wide swath altimetry to improve arctic river modeling. *Remote Sensing of Environment*, **115**(2):373 – 381. doi:10.1016/j.rse.2010.09.008.

Biancamaria, S, Lettenmaier, DP and Pavelsky, TM (2016). The SWOT mission and its capabilities for land hydrology. *Surveys in Geophysics*, **37**(2):307–337. doi:10.1007/s10712-015-9346-y.

Birkinshaw, SJ, O'Donnell, GM, Moore, P, Kilsby, CG et al. (2010). Using satellite altimetry data to augment flow estimation techniques on the mekong river. *Hydrological Processes*, **24**(26):3811–3825. doi:10.1002/hyp.7811.

Bock, H, Jäggi, A, Švehla, D, Beutler, G et al. (2007). Precise orbit determination for the GOCE satellite using GPS. *Advances in Space Research*, **39**(10):1638–1647. doi:10.1016/j.asr.2007.02.053.

Bosch, W, Dettmering, D and Schwatke, C (2014). Multi-mission cross-calibration of satellite altimeters: Constructing a long-term data record for global and regional sea level change studies. *Remote Sensing*, **6**(3):2255. doi:10.3390/rs6032255.

Bouzinac, C (2012). CryoSat product handbook. ESA, UCL, *URL https://earth esa int/documents/10174/125272/CryoSat_Product_Handbook*.

Brenner, A, Zwally, H, Bentley, C, Csatho, B et al. (2003). Geoscience laser atimeter system algorithm theoretical basis document: Derivation of range and range distributions from laser pulse waveform analysis for surface elevation, rougrough, slope and vegetation height. *Algorithm Theoretical Basis Documents (ATBD)*, **99**.

Bronner, E, Guillot, A, Picot, N and Noubel, J (2013). SARAL/Altika products handbook. *No CNES:* SALP-MU-M-OP-*15984*-CN.

Brown, G (1977). The average impulse response of a rough surface and its applications. *Antennas and Propagation, IEEE Transactions on*, **25**(1):67–74. doi:10.1109/TAP.1977.1141536.

Callahan, PS, Morris, CS and Hsiao, SV (1994). Comparison of Topex/Poseidon σ_0 and significant wave height distributions to Geosat. *J Geophys Res*, **99**(C12):25,015–25,024. doi:10.1029/94JC01759.

Cartwright, DE and Tayler, RJ (1971). New computations of the tide-generating potential. *Geophysical Journal International*, **23**(1):45–73. doi:10.1111/j.1365-246X.1971.tb01803.x.

Chelton, DB, Walsh, EJ and Macarthur, JL (1989). Pulse compression and sea level tracking in satellite altimetry. *Journal of Atmospheric and Oceanic Technology*, **6**(3):407–438. doi:10.1175/1520-0426(1989).

Crétaux, JF, Abarca-del Río, R, Bergé-Nguyen, M, Arsen, A et al. (2016). Lake volume monitoring from space. *Surveys in Geophysics*, **37**(2):269–305. doi:10.1007/s10712-016-9362-6.

Davis, CH (1995). Growth of the Greenland ice sheet: a performance assessment of altimeter retracking algorithms. *Geoscience and Remote Sensing, IEEE Transactions*, **33**(5):1108–1116.

doi:10.1109/36.469474.

——— (1997). A robust threshold retracking algorithm for measuring ice-sheet surface elevation change from satellite radar altimeters. *Geoscience and Remote Sensing*, IEEE *Transactions*, **35**(4):974–979. doi:10.1109/36.602540.

Dawood, G and Ismail, SS (2005). Enhancing the integrity of the national geodetic data bases in Egypt. In: *Proceeding of* FIG *Working Week*.

Dejong, C (1991). GPS: Satellite orbits and atmospheric effects. NASA *S*TI*/Recon Technical Report N*, **92**:14,097.

Deng, X (2003). *Improvement of geodetic parameter estimation in coastal regions from satellite radar altimetry*. Ph.D. thesis, Curtin University of Technology.

Dinardo, S and Benveniste, J (2013). *Guidelines for the* SAR *(Delay-Doppler) L1b processing*. Tech. rep., XCRY-GSEG-EOPS-TN-14-0042, issue 2.3, 29/05/2013, ESA-ESRIN, http://wiki.services.eoportal.org/tiki-download_wiki_attachment.php, attId=2540.

Dubey, AK, Gupta, P, Dutta, S and Kumar, B (2014). Evaluation of satellite-altimetry-derived river stage variation for the braided Brahmaputra river. *International Journal of Remote Sensing*, **35**(23):7815–7827. doi:10.1080/01431161.2014.978033.

Dumont, J, Rosmorduc, V, Picot, N, Desai, S et al. (2009). OSTM/Jason-2 products handbook. CNES:SALP-MU-M-OP-*15815*-CN,EUMETSAT*:* EUM/OPS-JAS/MAN*/08/0041*, JPL*:* OSTM-*29-1237*,NOAA/NESDIS*: Polar Series*/OSTM, **400**:1.

Ebaid, HM and Ismail, SS (2010). Lake Nasser evaporation reduction study. *Journal of Advanced Research*, **1**(4):315–322. doi:10.1016/j.asej.2013.01.004.

El Gammal, EA, Salem, SM and El Gammal, AEA (2010). Change detection studies on the world's biggest artificial lake (lake Nasser, Egypt). *The Egyptian Journal of Remote Sensing and Space Science*, **13**(2):89–99. doi:10.1016/j.ejrs.2010.08.001.

Elsawwaf, M, Willems, P, Pagano, A and Berlamont, J (2010). Evaporation estimates from Nasser lake, Egypt, based on three floating station data and bowen ratio energy budget. *Theoretical and applied climatology*, **100**(3-4):439–465. doi:10.1007/s00704-009-0168-z.

ESA, and MSSL-UCL (2013). *CryoSat product handbook*. Tech. rep., https://earth.esa.int/web/guest/missions/esa-operational-eo-missions/CryoSat.

ESA and CNES (2016). RADAR altimetry basic principle. http://www.altimetry.info, Last visit October 2016.

Fenoglio, ML, Fehlau, M, Ferri, L, Becker, M et al. (2010). Coastal sea surface heights from improved altimeter data in the Mediterranean sea. *Gravity, geoid and Earth observation, Springer Berlin Heidelberg*, pp. 253–261. doi:10.1007/978-3-642-10634-7_33.

Fenoglio-Marc, L, Dinardo, S, Scharroo, R, Roland, A et al. (2015). The German Bight: A validation of CryoSat-2 altimeter data in SAR mode. *Advances in Space Research*, **55**(11):2641 – 2656. doi:10.1016/j.asr.2015.02.014.

Fernandes, MJ, Lá¡zaro, C, Nunes, AL and Scharroo, R (2014). Atmospheric corrections for altimetry studies over inland water. *Remote Sensing*, **6**(6):4952. doi:10.3390/rs6064952.

Frappart, F, Calmant, S, Cauhopé, M, Seyler, F et al. (2006). Preliminary results of Envisat RA-2-derived water levels validation over the Amazon basin. *Remote Sensing of Environment*, **100**(2):252–264. doi:10.1016/j.rse.2005.10.027.

Fu, L, Alsdorf, D, Morrow, R, Rodriguez, E et al. (2012). SWOT: the Surface Water and Ocean Topography mission. *JPL publication*, pp. 12–05.

Fu, LL, Alsdorf, D, Rodriguez, E, Morrow, R et al. (2009). The Surface Water and Ocean Topography (SWOT) mission: spaceborne radar interferometry for oceanographic and hydrological applications. *Proceedings of* OCEANOBS, **9**:21–25.

Fu, LL and Cazenave, A (2001). *Satellite altimetry and earth sciences a hand book of techniques and applications*. Academic press, San Diego, California.

Galin, N, Wingham, D, Cullen, R, Fornari, M et al. (2013). Calibration of the CryoSat-2 interferometer and measurement of across-track ocean slope. *Geoscience and Remote Sensing*, IEEE *Transactions*, **51**(1):57–72. doi:10.1109/TGRS.2012.2200298.

Gaultier, L, Ubelmann, C and Fu, LL (2016). The challenge of using future SWOT data for oceanic field reconstruction. *Journal of Atmospheric and Oceanic Technology*, **33**(1):119–126. doi:10.1175/JTECH-D-15-0160.1.

Gavin, H (2011). The Levenberg-Marquardt method for nonlinear least squares curve-fitting problems. *Department of Civil and Environmental Engineering, Duke University*, pp. 1–15.

Ghosh, S, Thakur, PK, Garg, V, Nandy, S et al. (2015). SARAL/Altika waveform analysis to monitor inland water levels: A case study of Maithon reservoir, Jharkhand, India. *Marine Geodesy*, **38**(sup1):597–613. doi:10.1080/01490419.2015.1039680.

Guo, H, Jiao, W and Yang, Y (2004). The systematic difference and its distribution between the 1985 national height datum and the global quasigeoid. *Acta Geodaetica et Cartographica Sinica*, **33**(2):100–104.

Guo, JY, Chang, XT, Gao, YG, Sun, J et al. (2009). Lake level variations monitored with satellite altimetry waveform retracking. *Selected Topics in Applied Earth Observations and Remote Sensing,* IEEE *Journal of*, **2**(2):80–86. doi:10.1109/JSTARS.2009.2021673.

Guo, JY, Gao, YG, Chang, XT and Hwang, CW (2010a). Optimized threshold algorithm of Envisat waveform retracking over coastal sea. *Chinese Journal of Geophysics*, **53**(2):231–239. doi:10.1002/cjg2.1490.

Guo, JY, Hwang, CW, Chang, XT and Liu, Y (2006). Improved threshold retracker for satellite altimeter waveform retracking over coastal sea. *Progress in Natural Science*, **16**(7):732–738. doi:10.1080/10020070612330061.

Haas, R and Schuh, H (1996). Determination of frequency dependent Love and Shida numbers from VLBI data. *Geophys Res Lett*, **23**(12):1509–1512. doi:10.1029/96GL00903.

Harris, AR and Mason, IM (1989). Lake area measurement using AVHRR a case study. *International Journal of Remote Sensing*, **10**(4-5):885–895. doi:10.1080/01431168908903928.

Hayne, G (1980). Radar altimeter mean return waveforms from near-normal-incidence ocean surface scattering. IEEE *Transactions on Antennas and Propagation*, **28**(5):687–692. doi:10.1109/TAP.1980.1142398.

Hayne, G, Hancock, D, Purdy, C and Callahan, P (1994). The corrections for significant wave height and attitude effects in the Topex radar altimeter. *Journal of Geophysical Research: Oceans*, **99**(C12):24,941–24,955. doi:10.1029/94JC01777.

HHFS (2016). Hungarian Hydrological Forecasting Service, Danube river in-situ gauge data. http://ddvizig.hu/en, Last visit, October 2016.

Hopfield, HS (1971). Tropospheric effect on electromagnetically measured range: Prediction from surface weather data. *Radio Science*, **6**(3):357–367. doi:10.1029/RS006i003p00357.

Hwang, C, Peng, MF, Ning, J, Luo, J et al. (2005). Lake level variations in China from Topex/-Poseidon altimetry: data quality assessment and links to precipitation and ENSO. *Geophysical Journal International*, **161**(1):1–11. doi:10.1111/j.1365-246X.2005.02518.x.

Iliffe, JC, Ziebart, M, Cross, PA, Forsberg, R et al. (2003). OSGM02: A new model for converting GPS-derived heights to local height datums in great Britain and Ireland. *Survey Review*, **37**(290):276–293. doi:10.1179/sre.2003.37.290.276.

Jacobs, G, Broome, R, Leben, R, Russell, L et al. (2010). *Jason-2 Validation Test Report (VTR): Validation of Sea Surface Height Anomaly Precision and Accuracy for Mesoscale Applications*. Tech. rep., DTIC Document.

Jäggi, A, Hugentobler, U, Bock, H and Beutler, G (2007). Precise orbit determination for GRACE using undifferenced or doubly differenced GPS data. *Advances in Space Research*, **39**(10):1612 – 1619. doi:10.1016/j.asr.2007.03.012.

Jain, M, Andersen, OB, Dall, J and Stenseng, L (2015). Sea surface height determination in the Arctic using CryoSat-2 SAR data from primary peak empirical retrackers. *Advances in Space Research*, **55**(1):40–50. doi:10.1016/j.asr.2014.09.006.

Jensen, JR (1999). Angle measurement with a phase monopulse radar altimeter. IEEE *Transactions on Antennas and Propagation*, **47**(4):715–724. doi:10.1109/8.768812.

Jiao, W, Wei, Z, Ma, X, Sun, Z et al. (2002). The origin vertical shift of national height datum 1985 with respect to the geoidal surface. *Acta Geodaetica et Cartographica Sinica*, **31**(3):196–200.

Kang, Z, Tapley, B, Bettadpur, S, Ries, J et al. (2006). Precise orbit determination for the GRACE mission using only GPS data. *Journal of Geodesy*, **80**(6):322–331. doi:10.1007/s00190-006-0073-5.

Kaula, WM (1966). *Theory of satellite geodesy: applications of satellites to geodesy*. Courier Dover Publications.

Kiss, T, Fiala, K and Sipos, G (2008). Alterations of channel parameters in response to river regulation works since 1840 on the lower Tisza river (Hungary). *Geomorphology*, **98**(12):96 – 110. doi:10.1016/j.geomorph.2007.02.027. The Geomorphological and Palaeohydrological Response of Fluvial Systems to Climatic, Human and Tectonic Controls.

Kleinherenbrink, M, Ditmar, PG and Lindenbergh, RC (2014). Retracking CryoSat data in the SARIn mode and robust lake level extraction. *Remote Sensing of Environment*, **152**:38–50. doi:10.1016/j.rse.2014.05.014.

Kleinherenbrink, M, Lindenbergh, R and Ditmar, P (2015). Monitoring of lake level changes on the Tibetan Plateau and Tian Shan by retracking CryoSat SARIn waveforms. *Journal of Hydrology*, **521**:119–131. doi:10.1016/j.jhydrol.2014.11.063.

Kouraev, AV, Zakharova, EA, Samain, O, Mognard, NM et al. (2004). Ob river discharge from Topex/Poseidon satellite altimetry (1992–2002). *Remote Sensing of Environment*, **93**(1â2):238 – 245. doi:10.1016/j.rse.2004.07.007.

Kruizinga, GLH (1997). *Validation and applications of satellite radar altimetry*. University of Texas at Austin.

Laxon, S (1994). Sea ice altimeter processing scheme at the EODC. *International Journal of Remote Sensing*, **15**(4):915–924. doi:10.1080/01431169408954124.

Le Traon, P, Dibarboure, G and Ducet, N (2001). Use of a high-resolution model to analyze the mapping capabilities of multiple-altimeter missions. *Journal of Atmospheric and Oceanic Technology*, **18**(7):1277–1288. doi:10.1175/1520-0426(2001)018<1277:UOAHRM>2.0.CO;2.

Lebedev, SA and Kostianoy, AG (2005). Satellite altimetry of the Caspian sea. *Sea, Moscow*, **366**. doi:10.1016/j.rse.2015.10.023.

Lee, H, Shum, CK, Tseng, KH, Jun, YG et al. (2011). Present-day lake level variation from Envisat altimetry over the Northeastern Qinghai-Tibetan Plateau: links with precipitation and temperature. *Terrestrial, Atmospheric and Oceanic Sciences*, **22**(2):169–175. doi: 141.58.124.38.

Legresy, B and Remy, F (1997). Surface characteristics of the Antarctic ice sheet and altimetric observations. *J of Glacio*, **43**(144):265–275.

Leuliette, EW, Nerem, RS and Mitchum, GT (2004). Calibration of Topex/Poseidon and Jason altimeter data to construct a continuous record of mean sea level change. *Marine Geodesy*, **27**(1-2):79–94. doi:10.1080/01490410490465193.

Li, XY, Xu, HY, Sun, YL, Zhang, DS et al. (2007). Lake-level change and water balance analysis at lake Qinghai, west China during recent decades. *Water Resources Management*, **21**(9):1505–1516. doi:10.1007/s11269-006-9096-1.

Longman, IM (1966). Computation of Love numbers and load deformation coefficients for a model earth. *Geophysical Journal International*, **11**(1):133–137. doi:10.1111/j.1365-246X.1966.tb03495.x.

Maillard, P, Bercher, N and Calmant, S (2015). New processing approaches on the retrieval of water levels in Envisat and SARAL radar altimetry over rivers: A case study of the São Francisco river, Brazil. *Remote Sensing of Environment*, **156**:226 – 241. doi:10.1016/j.rse.2014.09.027.

Martin, TV, Zwally, HJ, Brenner, AC and Bindschadler, RA (1983). Analysis and retracking of continental ice sheet radar altimeter waveforms. *Journal of Geophysical Research: Oceans*, **88**(C3):1608–1616. doi:10.1029/JC088iC03p01608.

Michailovsky, C, McEnnis, S, Berry, P, Smith, R et al. (2012). River monitoring from satellite radar altimetry in the Zambezi river basin. *Hydrology and Earth System Sciences*, **16**(7):2181–2192. doi:doi:10.5194/hess-16-2181-2012.

Mohamed, H (2013). Evaporation estimation for lake Nasser based on remote sensing technology. *Ain Shams Engineering Journal*, **4**(4):593–604. doi:10.1016/j.asej.2013.01.004.

Montenbruck, O, van Helleputte, T, Kroes, R and Gill, E (2005). Reduced dynamic orbit determination using GPS code and carrier measurements. *Aerospace Science and Technology*,

9(3):261–271.

Moreira, A, Prats-Iraola, P, Younis, M, Krieger, G et al. (2013). A tutorial on synthetic aperture radar. *Geoscience and Remote Sensing Magazine,* IEEE, **1**(1):6–43. doi:10.1109/MGRS.2013.2248301.

Morris, CS and Gill, SK (1994). Evaluation of the Topex/Poseidon altimeter system over the Great lakes. *J Geophys Res*, **99**(C12):24,527–24,539. doi:10.1029/94JC01642.

NASA (2016). RADAR characteristics. http://www.nasa.gov/mission_ pages/ICESat, Last visit October 2016.

Nerem, RS, Chambers, DP, Choe, C and Mitchum, GT (2010). Estimating mean sea level change from the Topex and Jason-2 altimeter missions. *Marine Geodesy*, **33**(sup1):435–446. doi:10.1080/01490419.2010.491031.

Nielsen, K, Andersen, OB, Jain, M and Heidi, V (2014). *Lotus: State of the art review of* SAR *mode over land*. Tech. rep., Vesion 3, 07/05/2014, DTU Space, Denmark.

Nielsen, K, Stenseng, L, Andersen, OB, Villadsen, H et al. (2015). Validation of CryoSat-2 SAR mode based lake levels. *Remote Sensing of Environment*, **171**:162 – 170. doi:10.1016/j.rse.2015.10.023.

NSIDC (2016). NASA Distributed Active Archive Center (DAAC) at NSIDC. https://nsidc.org/data/ICESat/data.html, Last visit October 2016.

Pascual, A, Faugãre, Y, Larnicol, G and Le Traon, PY (2006). Improved description of the ocean mesoscale variability by combining four satellite altimeters. *Geophys Res Lett*, **33**(2):n/a–n/a. doi:10.1029/2005GL024633.

Pavlis, NK, Holmes, SA, Kenyon, SC and Factor, JK (2012). The development and evaluation of the Earth Gravitational Model 2008 (EGM2008). *J Geophys Res*, **117**(B4):n/a–n/a.

Pengra, B, Chander, A, Litswa, E, Giese, K et al. (2012). The drying of Iran's lake Urmia and its environmental consequences. UNEP-GRID, *Sioux Falls,* UNEP *Global Environmental Alert Service (*GEAS*)*.

Press, WH, Teukolsky, SA, Vetterling, WT and Flannery, BP (1996). *Numerical recipes in Fortran 77 and Fortran 90*. Cambridge University Press Cambridge.

RAC (2016). Rivers Agency Coleraine, Neagh lake in-situ gauge data. https://www.dardni.gov.uk/rivers-agency, Last visit, October 2016.

Raney, R (1998). The delay/Doppler radar altimeter. *Geoscience and Remote Sensing,* IEEE *Transactions*, **36**(5):1578–1588. doi:10.1109/36.718861.

Ray, C, Martin-Puig, C, Clarizia, MP, Ruffini, G et al. (2015). SAR altimeter backscattered waveform model. IEEE *Transactions on Geoscience and Remote Sensing*, **53**(2):911–919. doi:10.1109/TGRS.2014.2330423.

Reubelt, T, Sneeuw, N and Sharifi, M (2010). Future mission design options for spatio-temporal geopotential recovery. In: *Gravity, Geoid and Earth Observation*, pp. 163–170. Springer.

Rezvantalab, S and Amrollahi, MH (2011). Investigation of recent changes in Urmia salt lake. *International Journal of Chemical and Environmental Engineering*, **2**(3).

Ričko, M, Birkett, CM, Carton, JA and Crétaux, JF (2012). Intercomparison and validation of continental water level products derived from satellite radar altimetry. *Journal of Applied Remote Sensing*, **6**(1):061,710–061,710. doi:10.1117/1.JRS.6.061710.

Rodriguez, E (1988). Altimetry for non-Gaussian oceans: Height biases and estimation of parameters. *J Geophys Res*, **93**(C11):14,107–14,120. doi:10.1029/JC093iC11p14107.

Roohi, SH (2015). *Capability of pulse-limited satellite radar altimetry to monitor inland water bodies*. Master's thesis, Institute of Geodesy, University of Stuttgart, Url: http://elib.uni-stuttgart.de/opus/volltexte/2015/10160/.

Rosmorduc, V, Benveniste, J, Bronner, E, Dinardo, S et al. (2011). *Radar altimetry tutorial*. ESA and CNES.

Saastamoinen, J (1972). Atmospheric correction for the troposphere and stratosphere in radio ranging satellites. *The use of artificial satellites for geodesy*, pp. 247–251.

Saikrishnaveni, A, Chowdary, VM, Dutta, D, Sharma, JR et al. (2016). SARAL/ Altika altimetry data for monitoring of inland water body: a case study of Mayurakshi reservoir, India. *Journal of the Indian Society of Remote Sensing*, **44**(5):797–802. doi:10.1007/s12524-015-0535-4.

Salisbury, JW, Wald, A and D'aria, DM (1994). Thermal-infrared remote sensing and Kirchhoff's law: 1. laboratory measurements. *Journal of Geophysical Research: Solid Earth*, **99**(B6):11,897–11,911. doi:10.1029/93JB03600.

Santos, SJ, Calmant, S, Seyler, F, Rotunno, FOC et al. (2010). Water levels in the Amazon basin derived from the ERS-2 and Envisat radar altimetry missions. *Remote Sensing of Environment*, **114**(10):2160–2181. doi:10.1016/j.rse.2010.04.020.

Scherneck, HG (1991). A parametrized solid earth tide model and ocean tide loading effects for global geodetic baseline measurements. *Geophysical Journal International*, **106**(3):677–694. doi:10.1111/j.1365-246X.1991.tb06339.x.

Schutz, BE, Zwally, HJ, Shuman, CA, Hancock, D et al. (2005). Overview of the ICESat mission. *Geophys Res Lett*, **32**(21):n/a. doi:doi:10.1029/2005GL024009.

Schwatke, C, Dettmering, D, Börgens, E and Bosch, W (2015). Potential of SARAL/Altika for inland water applications. *Marine Geodesy*, **38**(sup1):626–643. doi:10.1080/01490419.2015.1008710.

Seeber, G (2003). *Satellite geodesy: foundations, methods, and applications*. Walter de Gruyter.

Shiklomanov, AI, Lammers, RB and Vörösmarty, CJ (2002). Widespread decline in hydrological monitoring threatens Pan-Arctic research. *Eos, Transactions American Geophysical Union*, **83**(2):13–17. doi:10.1029/2002EO000007.

Shum, CK, Woodworth, PL, Andersen, OB, Egbert, GD et al. (1997). Accuracy assessment of recent ocean tide models. *J Geophys Res*, **102**(C11):25,173–25,194.

Smith, EK and Weintraub, S (1953). The constants in the equation for atmospheric refractive index at radio frequencies. *Proceedings of the IRE*, **41**(8):1035–1037. doi:10.1109/JRPROC.1953.274297.

Sommerwerk, N, Hein, T, Schneider-Jakoby, M, Baumgartner, C et al. (2009). The Danube river basin. *Rivers of Europe*, pp. 59–112.

Srokosz, M, Caparrini, M, Dinardo, S and Lucas, B (2015). *Development of* SAR *altimetry mode studies and applications over ocean, coastal zones and inland water (*SAMOSA*)*. Tech. rep., Report No, 20698/07/1-LG, ESA/ESRIN.

Sulistioadi, Y, Tseng, KH, Shum, C, Hidayat, H et al. (2015). Satellite radar altimetry for monitoring small rivers and lakes in Indonesia. *Hydrology and Earth System Sciences*, **19**(1):341–359. doi:10.5194/hess-19-341-2015.

Tavernier, G, Fagard, H, Feissel-Vernier, M, Lemoine, F et al. (2005). The international DORIS service. *Advances in Space Research*, **36**(3):333 – 341. doi:10.1016/j.asr.2005.03.102. Satellite Dynamics in the Era of Interdisciplinary Space Geodesy.

Tourian, M, Tarpanelli, A, Elmi, O, Qin, T et al. (2016). Spatiotemporal densification of river water level time series by multimission satellite altimetry. *Water Resources Research*. doi:10.1002/2015WR017654.

Tourian, MJ (2012). *Controls on satellite altimetry over inland water surfaces for hydrological purposes*. Master's thesis, Institute of Geodesy, University of Stuttgart, Url: http://elib.uni-stuttgart.de/handle/11682/3896.

Tourian, MJ, Elmi, O, Chen, Q, Devaraju, B et al. (2015). A spaceborne multisensor approach to monitor the desiccation of lake Urmia in Iran. *Remote Sensing of Environment*, **156**(0):349–360. doi:10.1016/j.rse.2014.10.006.

Tseng, KH, Shum, CK, Yi, Y, Emery, WJ et al. (2014). The improved retrieval of coastal sea surface heights by retracking modified radar altimetry waveforms. *Geoscience and Remote Sensing,* IEEE *Transactions on*, **52**(2):991–1001. doi:10.1109/TGRS.2013.2246572.

Tseng, KH, Shum, CK, Yi, YC, Fok, HS et al. (2013). Envisat altimetry radar waveform retracking of quasi-specular echoes over the ice-covered Qinghai lake. *Terrestrial, Atmospheric and Oceanic Sciences*, **24**(4I):615–627. doi:10.3319/TAO.2012.12.03.01(TibXS).

Vignudelli, S, Kostianoy, AG, Cipollini, P and Benveniste, J (2011). *Coastal altimetry*. Springer-Verlag Berlin Heidelberg. doi:10.1007/978-3-642-12796-0.

Villadsen, H, Andersen, OB, Stenseng, L, Nielsen, K et al. (2015). CryoSat-2 altimetry for river level monitoring - evaluation in the Ganges-Brahmaputra river basin. *Remote Sensing of Environment*, **168**:80 – 89. doi:10.1016/j.rse.2015.05.025.

Völgyesi, L (1997). Transformation of hungarian unified national and Gauss-Krüger projection system into WGS-84. *Reports on Geodesy, Warsaw University of Technology*, **27**(4):281–294.

Wagner, C (1990). A prograde Geosat exact repeat mission. NASA STI/*Recon Technical Report* N, **91**.

Wahr, JM (1985). Deformation induced by polar motion. *J Geophys Res*, **90**(B11):9363–9368. doi:10.1029/JB090iB11p09363.

WARWA (2012). West Azarbaijan Rigional Water Authrity, Urmia lake in-situ gauge data. http://www.agrw.ir/.

Willis, P, Boucher, C, a Fagard, H and Altamimi, Z (2005). Geodetic applications of the DORIS system at the French institut géographique national. *Comptes Rendus Geoscience*, **337**(7):653 – 662. doi:10.1016/j.crte.2005.03.002.

Willis, P and Ries, JC (2005). Defining a DORIS core network for Jason-1 precise orbit determination based on ITRF2000: methods and realization. *Journal of Geodesy*, **79**(6):370–378. doi:10.1007/s00190-005-0475-9.

Wingham, D, Francis, C, Baker, S, Bouzinac, C et al. (2006). CryoSat: A mission to determine the fluctuations in Earth's land and marine ice fields. *Advances in Space Research*, **37**(4):841–871. doi:10.1016/j.asr.2005.07.027.

Wingham, D, Rapley, C and Griffiths, H (1986). New techniques in satellite altimeter tracking systems. In: *ESA Proceedings of the 1986 International Geoscience and Remote Sensing Symposium (IGARSS'86) on Remote Sensing: Today's Solutions for Tomorrow's Information Needs*, vol. 3. IGARSS86 Symposium, Zürich, 8-11 September 1986, ESA SP-254 (pp 1339-1344).

Wolff, C (1998). RADAR tutorial. http://www.radartutorial.eu, Last visit October 2016.

Wu, B, Bibo, P, Zhu, Y and Hsu, H (2001). Determination of Love numbers using satellite laser ranging. *Journal of the Geodetic Society of Japan*, **47**(1):174–180. doi:10.11366/sokuchi1954.47.174.

Yang, Y, Hwang, CW, Hsu, HJ, Dongchen, E et al. (2012). A subwaveform threshold retracker for ERS-1 altimetry: A case study in the Antarctic ocean. *Computers Geosciences*, **41**(0):88–98. doi:10.1016/j.cageo.2011.08.017.

Zhang, G, Xie, H, Duan, S, Tian, M et al. (2011a). Water level variation of lake Qinghai from satellite and in situ measurements under climate change. *Journal of Applied Remote Sensing*, **5**(1):053,532–053,532–15. doi:10.1117/1.3601363.

Zhang, G, Xie, H, Kang, S, Yi, D et al. (2011b). Monitoring lake level changes on the Tibetan Plateau using ICESat altimetry data (2003–2009). *Remote Sensing of Environment*, **115**(7):1733–1742. doi:10.1016/j.rse.2011.03.005.

Zhang, G, Yao, T, Xie, H, Qin, J et al. (2014). Estimating surface temperature changes of lakes in the Tibetan Plateau using MODIS LST data. *J Geophys Res Atmos*, **119**(14):8552–8567. doi:10.1002/2014JD021615.

Zhu, W, Jia, S and Lv, A (2014). Monitoring the fluctuation of lake Qinghai using multi-source remote sensing data. *Remote Sensing*, **6**(11):10,457–10,482. doi:10.3390/rs61110457.

Zoran, M (2003). Environmental changes monitoring by remote sensing for Danube river delta, Romania. doi:10.1117/12.462943.

Zwally, H, Schutz, B, Abdalati, W, Abshire, J et al. (2002). ICESat's laser measurements of polar ice, atmosphere, ocean, and land. *Journal of Geodynamics*, **34**(3-4):405 – 445. doi:10.1016/S0264-3707(02)00042-X.

Appendix A

SAMOSA3 retracker algorithm

Transmitted signal
A SAR altimeter sends a burst of N_b chirp pulses to the Earth's surface. A single chirp pulse can be written as (Ray et al., 2015):

$$\chi(t) = \begin{cases} e^{i2\pi(f_c + \frac{1}{2}st)t} & \text{if} \quad -\frac{\tau_p}{2} \leq t \leq \frac{\tau_p}{2} \\ 0 & \text{otherwise} \end{cases} , \tag{A.1}$$

in which f_c is the center frequency, s is the chirp slope and τ_p is the chirp pulse duration.

The transmitted burst of pulses can be written as (Ray et al., 2015):

$$S_T(t) = \sum_{m=1-N_b/2}^{N_b/2} \chi(t - m/\text{PRF} + r(t)/c) \ , \tag{A.2}$$

where N_b is the number of pulses in a burst, c is the speed of light and r is the presumed distance between the radar and water surface.
Reflected signal
The reflected signal has a delay of $r(t)/c$, so the signal at a scattering point at time t is (Ray et al., 2015):

$$S_P(t) = S_T(t - r(t)/c) \ . \tag{A.3}$$

The received signal is delayed further $r(t)/c$, so the signal received at $t + r(t)/c$ is the same (apart from amplitude) as the signal at the scattering point at time t (Ray et al., 2015):

$$S_R(t + r(t)/c) = S_P(t) = S_T(t - r(t)/c) \ . \tag{A.4}$$

Deramping
After receiving the reflected signal, it is multiplied with the complex conjugate of a delayed copy of the transmitted signal. This is called deramping, because it removes the frequency ramp of the chirp signal. So we have:

$$D(t) = S_R(t + r(t)/c) S_T^*(t - r(t)/c) \ . \tag{A.5}$$

The range of the scatterer can be encoded as the frequency of the deramped signal (Ray et al., 2015):

$$D(t) = S_T(t - r(t)/c - \tau_d) S_T^*(t - r(t)/c) = \sum_{m=1-N_b/2}^{N_b/2} \chi(t - m/\text{PRF} - \tau_d) \chi^*(t - m/\text{PRF}) \ . \tag{A.6}$$

Discrete sampling
The previously defined product is sampled by an analog to digital converter. The n-th sample of the m-th pulse happens at time $t_{n,m}$ (Ray et al., 2015):

$$t_{n,m} = \frac{m}{\mathrm{PRF}} + \frac{n}{f_\mathrm{s}} \ , \tag{A.7}$$

in which f_s is the sampling rate, n and m are the number of bin and pulse respectively. So the deramped signal for sample n and m is:

$$\begin{aligned} D_{n,m} = D(t_{n,m}) = \chi(\tau_n - \tau_\mathrm{d})\chi^*(\tau_n) = \mathrm{e}^{i2\pi(f_\mathrm{c}(\tau_n-\tau_\mathrm{d})+\frac{1}{2}s(\tau_n-\tau_\mathrm{d})^2)}\mathrm{e}^{-i2\pi(f_\mathrm{c}\tau_n+\frac{1}{2}s\tau_n^2)}\ldots \\ = \mathrm{e}^{i2\pi(-f_\mathrm{c}\tau_\mathrm{d}-s\tau_n\tau_\mathrm{d}+\frac{1}{2}s\tau_\mathrm{d}^2)} \ , \end{aligned} \tag{A.8}$$

in which $\tau_\mu = N_\mathrm{p}/f_\mathrm{s}$, $\tau_\mathrm{n} = n/f_\mathrm{s}$ and N_p is the number of sample per pulse. By defining $\tau_\mathrm{d} = \tau_\mathrm{s} - \mu t_{n,m}$ and neglecting the minor terms (contribution less than a quarter of a cycle in phase) one arrive at the following equation (Ray et al., 2015):

$$D_{n,m} \approx \mathrm{e}^{i\phi_0}\mathrm{e}^{-i2\pi s\tau_\mathrm{s}n/f_\mathrm{s}}\mathrm{e}^{i2\pi f_\mathrm{c}\mu m/\mathrm{PRF}} \ , \tag{A.9}$$

where $\phi_0 = 2\pi(\frac{1}{2}s\tau_\mathrm{s}^2 - f_\mathrm{c}\tau_\mathrm{s})$. The term $\mathrm{e}^{i\phi_0}$ is a unit value which is independent of indexes n and m. So it has no contribution in constructing the waveform and it can be ignored.

Doppler correction
According to Ray et al. (2015) the Doppler correction factor would be $\mathrm{e}^{i2\pi f_\mathrm{c}(2v_\mathrm{r}/c)(m/\mathrm{PRF})}$. By multiplying $D_{n,m}$ with this factor we receive:

$$\hat{D}_{n,m} = \mathrm{e}^{i2\pi f_\mathrm{c}\frac{2v_\mathrm{r}}{c}\frac{m}{\mathrm{PRF}}}D_{n,m} = \mathrm{e}^{-i2\pi s\tau_\mathrm{s}\frac{n}{f_\mathrm{s}}}\mathrm{e}^{i2\pi\frac{x}{Lx}\frac{m}{N_\mathrm{b}}} \ , \tag{A.10}$$

in which $L_x = \frac{cH\mathrm{PRF}}{2v_\mathrm{t}f_\mathrm{c}N_\mathrm{b}}$. The parameters v_r and v_t are radial and tangential velocity of the satellite.

Along-track FFT or SAR processing
To do SAR processing, a given burst in along-track direction is being focused into N_b narrow beams via fast Fourier transformation across the different pulses in this burst. So sample n of beam l is calculated as (Ray et al., 2015):

$$\begin{aligned} \tilde{D}_{n,l} = \sum_{m=1-N_\mathrm{b}/2}^{N_\mathrm{b}/2} w_\mathrm{m}\hat{D}_{n,m}\mathrm{e}^{-i2\pi lm/N_\mathrm{b}} = \mathrm{e}^{-i2\pi s\tau_\mathrm{s}\frac{n}{f_\mathrm{s}}}\sum_{m=1-N_\mathrm{b}/2}^{N_\mathrm{b}/2} w_\mathrm{m}\mathrm{e}^{i2\pi(\frac{x}{Lx}-l)m/N_\mathrm{b}}\ldots \\ = \mathrm{e}^{-i2\pi s\tau_\mathrm{s}\frac{n}{f_\mathrm{s}}}N_\mathrm{b}\gamma_{N_\mathrm{b}}(\frac{x}{Lx} - l) \ , \end{aligned} \tag{A.11}$$

where w_m is the window function to be used in FFT.

Range cell migration correction
A given scattering cell is sensed several times. To have the same radar range for this cell, all of the ranges measured from this cell need to be corrected (Nielsen et al., 2014). This correction called range cell migration correction. According to Ray et al. (2015) this correction is $\mathrm{e}^{i2\pi s\alpha L_x^2 l^2 n/(Hcf_\mathrm{s})}$. So the corrected beam is:

$$C_{n,l} = \mathrm{e}^{i2\pi s\frac{\alpha L_x^2 l^2 n}{Hcf_\mathrm{s}}}\tilde{D}_{n,l} = N_\mathrm{b}\gamma_{N_\mathrm{b}}(u)\mathrm{e}^{-i2\pi k_l n/N_\mathrm{p}} \ , \tag{A.12}$$

in which:

$$u = \frac{x}{L_x} - l \ , \tag{A.13}$$

$$k_l = \frac{L_x^2}{L_y^2}(u^2 + 2lu) + \frac{y^2}{L_y^2} - \frac{z}{L_z} \ , \tag{A.14}$$

$$L_y = \sqrt{\frac{cH}{\alpha s \tau_u}} \quad L_z = \frac{c}{2s\tau_u} \ . \tag{A.15}$$

Along-track IFFT

In this step the inverse fast Fourier transformation is performed over each beam. So the range k of beam l after this transformation is (Ray et al., 2015):

$$\tilde{C}_{k,l} = \frac{1}{N_p} \sum_{n=1-N_p/2}^{N_p/2} w_m C_{n,l} e^{i2\pi nk/N_p} = N_b \gamma_{N_b}(u) \gamma_{N_p}(k - k_l) \ . \tag{A.16}$$

SAR waveform

The total backscattered power received by the radar is the sum of the power of all scatterers inside the footprint of the radar. So the total power in cell (k, l) is (Ray et al., 2015):

$$P_{k,l} = \int_{-\infty}^{+\infty} dz p(z) \int_{-\infty}^{+\infty} dx \int_{-\infty}^{+\infty} dy \frac{\lambda_0^2 G^2(x,y)\sigma_0(x,y)}{4\pi r^4} \left|\tilde{C}_{k,l}\right|^2 \ , \tag{A.17}$$

where $p(z)$ is the height probability density function for the point inside the footprint (Rodriguez, 1988), G is the antenna power gain and σ_0 is the normalized radar cross section. For simplification we define the following function:

$$\Gamma(x,y) = G^2(x,y)\sigma_0(x,y) \ . \tag{A.18}$$

Based on the definition of odd and even function, $\Gamma_e(x,y) = \Gamma(x,y) + \Gamma(x,-y)$ and $\Gamma_o(x,y) = \Gamma(x,y) - \Gamma(x,-y)$, we can rewrite Γ:

$$\Gamma(x,y) = \frac{1}{2}\Gamma_e(x,y) + \frac{1}{2}\Gamma_o(x,y) \ . \tag{A.19}$$

So if we integrate y over $\left|\tilde{C}_{k,l}\right|^2 / r^4$ the odd part will be zero then:

$$\int_{-\infty}^{+\infty} dy \Gamma(x,y) \frac{\left|\tilde{C}_{k,l}\right|^2}{r^4} = \int_{-\infty}^{+\infty} dy \Gamma_e(x,y) \frac{\left|\tilde{C}_{k,l}\right|^2}{r^4} = \int_{0}^{+\infty} dy \Gamma_e(x,y) \frac{\left|\tilde{C}_{k,l}\right|^2}{r^4} \ . \tag{A.20}$$

Therefore the power can be written as (Ray et al., 2015):

$$P_{k,l} = \int_{-\infty}^{+\infty} dz p(z) \int_{-\infty}^{+\infty} dx \int_{0}^{+\infty} dy \frac{\lambda_0^2 \Gamma_e(x,y)}{4\pi r^4} \left|\tilde{C}_{k,l}\right|^2 \ . \tag{A.21}$$

Since $1/r^4$ is nearly constant over the footprint we can write: $1/r^4 = 1/H^4$ (H is the satellite height). So the power function would be (Ray et al., 2015):

$$P_{k,l} \approx \frac{\lambda_0^2}{4\pi h^4} \int_{-\infty}^{+\infty} dz p(z) \Gamma_{k,l}(z) \int_{-\infty}^{+\infty} dx \int_{0}^{\infty} dy \left|\tilde{C}_{k,l}\right|^2 \ , \tag{A.22}$$

with

$$\Gamma_{k,l}(z) = \begin{cases} \Gamma_e(L_x l, Ly\sqrt{(k + z/L_z)}) & \text{if } z > -L_z k \\ \\ \Gamma_e(L_x l, 0) & \text{if } z < -L_z k \end{cases} . \tag{A.23}$$

$\Gamma_{k,l}(z)$ can be written as a linear combination of (Ray et al., 2015):

$$\Gamma_{k,l}(z) \approx B_{k,l}(1 + T_{k,l} z/L_z) \ , \tag{A.24}$$

with the following definition for $B_{k,l}$ and $T_{k,l}$:

$$B_{k,l} = \int_{-\infty}^{+\infty} dz \frac{e^{-z^2/2\sigma^2}}{\sqrt{2\pi}\sigma} \Gamma_{k,l}(z) \ , \tag{A.25}$$

$$T_{k,l} = \frac{L_z}{B_{k,l}\sigma^2} \int_{-\infty}^{+\infty} dz \frac{e^{-z^2/2\sigma^2}}{\sqrt{2\pi}\sigma} z\Gamma_{k,l}(z) \ . \tag{A.26}$$

So if we write $P_{k,l}$ based on $B_{k,l}$ and $T_{k,l}$ we have:

$$P_{k,l} = KB_{k,l}\sqrt{g_l}\left[(1 + T_{k,l}k_{\text{off}})f_0(g_l k) + T_{k,l}g_l\sigma_s^2 f_1(g_l K) + \lambda_s \frac{g_l^3\sigma_s^3}{6}\Big(3f_1(g_l k) + f_3(g_l k)\Big)\right] \ , \tag{A.27}$$

in which:

$$K = \frac{\lambda_0^2 N_b^2 L_x L_y}{4\pi H^4}\sqrt{2\pi}A_g^2\sigma_g^2, \quad \sigma_s = \frac{\sigma_z}{L_z} \ , \tag{A.28}$$

A_g and σ_g are parameters related to Gaussian height probability density function and

$$k_{\text{off}} = \frac{\mu_z - z_{\text{EM}}}{L_z} \ , \tag{A.29}$$

$$g_l = \left[\sigma_g^2 + (2\sigma_g l L_x^2/L_y^2)^2 + \sigma_s^2\right]^{-1/2} \ , \tag{A.30}$$

$$f_n(\xi) = \int_0^{+\infty} dv (v^2 - \xi)^n e^{-(v^2-\xi)^2/2} \ . \tag{A.31}$$

In equation (A.27) the third term is very small, so it can be ignored (Ray et al., 2015), leading to:

$$P_{k,l} = KB_{k,l}\sqrt{g_l}\left[(1 + T_{k,l}k_{\text{off}})f_0(g_l k) + T_{k,l}g_l\sigma_s^2 f_1(g_l k)\right] \ . \tag{A.32}$$

According to Ray et al. (2015) if the on-board tracking system is working correctly then $|T_{k,l}k_{\text{off}}|$ is small and it can be ignored:

$$P_{k,l} = KB_{k,l}\sqrt{g_l}\left[f_0(g_l k) + T_{k,l}g_l\sigma_s^2 f_1(g_l k)\right] \ . \tag{A.33}$$

This function is modified as following in Srokosz et al. (2015):

$$W_{k,l} = P_u\left(\alpha_p^2\sqrt{2\pi}\right)\sqrt{g_l}\Gamma_{k,l}(0)\left\{f_0(g_l k) + \frac{\sigma_z}{L_\Gamma}g_l\frac{\sigma_z}{L_z}T_k f_1(g_l k)\right\} \ , \tag{A.34}$$

in which:

$$f_0(\xi) = \int_0^{+\infty} \mathrm{e}^{\frac{-1}{2}(\xi-\nu^2)^2} d\nu = \frac{\pi}{2\sqrt{2}} \left(\frac{1}{4}\xi^2\right)^{1/4} \left[\mathrm{I}^{\mathrm{SC}}_{\frac{-1}{4}}\left(\frac{1}{4}\xi^2\right) + \mathrm{sign}(\xi)\mathrm{I}^{\mathrm{SC}}_{\frac{1}{4}}\left(\frac{1}{4}\xi^2\right) \right] , \tag{A.35}$$

$$\begin{aligned} f(\xi) = \int_0^{+\infty} \mathrm{e}^{-\frac{1}{2}(\xi-\nu^2)^2} (\xi-\nu^2) d\nu = \frac{\pi}{2\sqrt{2}} \left(\frac{1}{4}\xi^2\right)^{\frac{3}{4}} \Bigg[& \mathrm{I}^{\mathrm{SC}}_{\frac{1}{4}}\left(\frac{1}{4}\xi^2\right) - \mathrm{I}^{\mathrm{SC}}_{-\frac{3}{4}}\left(\frac{1}{4}\xi^2\right) \ldots \\ & + \mathrm{sign}(\xi) \left(\mathrm{I}^{\mathrm{SC}}_{-\frac{1}{4}}\left(\frac{1}{4}\xi^2\right) - \mathrm{I}^{\mathrm{SC}}_{-\frac{3}{4}}\left(\frac{1}{4}\xi^2\right) \right) \Bigg] , \end{aligned} \tag{A.36}$$

where $\mathrm{I}^{\mathrm{SC}}_{\nu}$ is the spherical modified Bessel function of the first kind and order ν which is defined as: $\mathrm{I}^{\mathrm{SC}}_{\nu}(z) = \mathrm{e}^{-|z|}\mathrm{I}_{\nu}(z)$. In equation (A.34) k is the range bin, l the Doppler frequency index, σ_z is the surface roughness and P_u is waveform amplitude. The rest of the parameters will be defined in the following (Srokosz et al., 2015):

$$g_l = \frac{1}{\sqrt{\alpha_{\mathrm{p}}^2 + 4\alpha_{\mathrm{p}}^2 \left(\frac{L_x}{L_y}\right)^4 (l - l_{\mathrm{s}})^2 + \left(\frac{H_{\mathrm{S}}}{4L_Z}\right)^2}} , \tag{A.37}$$

$$L_x = \frac{cH}{2V_{\mathrm{S}} f_c T_{\mathrm{b}}}, \;\; L_y = \sqrt{\frac{cH}{\alpha B_{\mathrm{r}}}}, \;\; L_z = \frac{c}{2B_{\mathrm{r}}}, \;\; L_\Gamma = \frac{\alpha}{2H\alpha_y}, \;\; l_{\mathrm{s}} = \frac{sH}{\alpha L_x} , \tag{A.38}$$

$$s = \mp \left(\frac{a^2 - b^2}{2R_{\mathrm{e}}^2}\right) \sin(2\theta_{\mathrm{plat}}) - \left(-\frac{H_{\mathrm{rate}}}{V_{\mathrm{S}}}\right) , \begin{cases} - & \text{for ascending} \\ + & \text{for descending} \end{cases} , \tag{A.39}$$

$$T_k = \begin{cases} \left(1 + \frac{\nu}{H^2\alpha_y}\right) - \frac{y_{\mathrm{p}}}{L_y\sqrt{k}} \tanh(2\alpha_y y_{\mathrm{p}} L_y \sqrt{k}) & \text{for } k > 0 \\ \left(1 + \frac{\nu}{H^2\alpha_y}\right) - 2\alpha_y y_{\mathrm{p}}^2 & \text{for } k \leq 0 \end{cases} , \tag{A.40}$$

$$\Gamma_{k,l}(0) = \exp\left[-\alpha_y y_{\mathrm{p}}^2 - \alpha_x (x_l - x_{\mathrm{p}})^2 - \frac{x_l^2 \nu}{H^2} - (\alpha_y + \frac{\nu}{H^2}) y_k^2 \right] \cosh(2\alpha_y y_{\mathrm{p}} y_k) , \tag{A.41}$$

in which:

$$y_k = \begin{cases} L_y\sqrt{k} & \text{if } k > 0 \\ 0 & \text{otherwise} \end{cases} , \tag{A.42}$$

$$x_l = L_x l, \;\; \alpha_x = sh_x \frac{8ln(2)}{H^2\theta_x^2}, \;\; \alpha_y = sh_y \frac{8ln(2)}{H^2\theta_y^2}, \;\; x_{\mathrm{p}} = H\theta_{\mathrm{pitch}}, \;\; y_{\mathrm{p}} = -H\theta_{\mathrm{roll}}, \;\; \nu = \frac{1}{\mathrm{MMS}} . \tag{A.43}$$

Table A.1: *Universal and sensor parameters used in* SAMOSA3 *retracker (Srokosz et al., 2015)*

Parameter	Description	Unit
c	speed of light	$\mathrm{m\,s^{-1}}$
a	equatorial Earth radius	m
b	polar Earth radius	m
f_c	central frequency	Hz
B_r	received bandwidth	Hz
G_0	antenna gain	dB
θ_x	along-track 3 dB beamwidth	rad
θ_y	across-track 3 dB beamwidth	rad
θ_pitch	pitch angle	rad
θ_roll	roll angle	rad
PRF	pulse repetition frequency	Hz
τ_u	useful pulse length	s
N_b	number of echoes per burst	-
H	spacecraft altitude	m
H_S	significant wave height	m
H_rate	spacecraft altitude rate	$\mathrm{m\,s^{-1}}$
V_S	spacecraft velocity	$\mathrm{m\,s^{-1}}$
θ_plat	ground cell latitude	rad
N_p	number of waveform sample	-
sh_x	antenna shape factor along-track for misalignment of the focal point	-
sh_y	antenna shape factor across-track for misalignment of the focal point	-
T_b	burst length	s
α	Earth curvature effect	-
MMS	mean square slopes of the surface	$\mathrm{rad^{-2}}$

Appendix B

Future satellite altimetry

B.1 SWOT

Studying recently global changes by space borne technologies has become a main concern for scientists. Water level variation of inland water bodies is an indicator for the global climate changes. An accurate statistic information of water level variations is very important in this respect.

In-situ gauge networks traditionally are used to provide information of surface water storage and river discharge only for a small part of the inland water bodies. These networks with daily (usually) sampling have enough temporal resolution to monitor inland water bodies but their spatial coverage are not enough. They are not homogeneously distributed along rivers and around lakes across the world. They follow national policy and there is not a unified in-situ gauge data base to be openly accessible where they are needed. Moreover many countries don't share their in-situ gauge data while the water resources and flood risk management of downstream countries dependent on Hydrological information of upstream countries.

Previous satellite altimetry missions could solve partially the problem of water level monitoring over the oceans and a part of inland water bodies, e.g. large lakes. Advances in the radar systems and data processing methodologies provide this possibility for the current satellite altimetry missions to sense small inland water bodies. However due to the temporal and spatial sampling, e.g. a 369 day repeat cycle for CryoSat-2, the current nadir altimetry missions can also not provide global coverage (or they can poorly observe inland water bodies in a global scale) for monitoring rivers and lakes especially in higher latitude regions. Conventional (nadir) altimeters only measure a one-dimensional profile of water level along the satellite track that is not enough to provide an accurate statistic information of water level variations in the global scale.

With a combination of data from several nadir altimeters one can obtain more information about inland water bodies but still the spatial resolution is too coarse. They can only monitor a 15% of global water level variations (Biancamaria et al., 2011) i.e, there is a large gap in data sets which is a big obstacle for hydrological and climate researches. A part of poorly coverage of the previous and current altimetry missions relates to the orbital geometry and measurement modes (type of the radar system). To provide a global coverage with enough spatial and temporal resolution geometry of the orbit and radar characteristics must be considered for new generation of satellite altimetry missions.

Surface Water and Ocean Topography (SWOT) satellite mission addresses weak points of past and current satellite altimetry mission in both spatial and time samplings. This mission will retrieve a large amount of data over inland water bodies at scales that have never been provided. As a cooperation between NASA and CNES, SWOT mission brings US and French oceanographers and hydrologist as well as international partners together to design a new generation of satellite altimetry (with a global coverage) to observe fine details of the ocean's surface topography, and to measure how water bodies change over time.

SWOT is a Ka-band Radar Interferometer (KaRIN) that contains two Ka-band SAR antennas at opposite ends of a 10 m boom with both antennae transmitting and receiving the radar pulses along both sides of the along track direction. The orbit height is about 891 km with a 21 days repeat cycle (Gaultier et al., 2016). Looking angles are limited to 1°– 4° that provides a 120 km wide swath. With a 200 MHz bandwidth achieving the cross track ground resolutions varying from about 10 m in the far swath to about 60 m in the near swath (Biancamaria et al., 2016) is possible. A resolution of about 2 m in the along track direction is obtained by means of synthetic aperture processing.

This mission includes two phases. The first phase is a fast sampling phase with three months lifetime that is dedicated to validation and calibration. The second phase is a nominal phase that covers the whole lifetime of this mission. The lifetime is supposed to be 3 years. The orbit height in both phases is approximately 891 km. Figure B.1 illustrates the conceptual view of the SWOT system. Oceanography and hydrology are two main applications of the SWOT mission. Since we study water level variation of inland water bodies in this research the hydrological aspect of SWOT will be considered.

B.2 SWOT orbit design for hydrological applications

According to Fu et al. (2009) and Fu et al. (2012) the most important SWOT hydrological science questions are:

- What is the spatial and temporal variability in the world's terrestrial surface water storage and discharge? How can we predict these variations more accurately?
- How much water is stored on a floodplain and subsequently exchanged with its main channel?
- What policy implications would freely available water storage have for water management?

Finding the proper answer to these questions leads to the following requirements for a SWOT mission:

- All lakes greater than 250 m $\times$ 250 m must be measured with a temporal resolution of at least 10 days and a vertical precision of at least 10 cm.
- In order to observe most of the lakes and rivers, the SWOT measurements must be made to at least 74° latitude.
- In order to observe global fluvial processes, rivers with widths greater than 50 –100 m must be measured. The vertical precision of water surface elevation measurements must be at least 10 cm and river slope must be measured to within 1 cm/km.

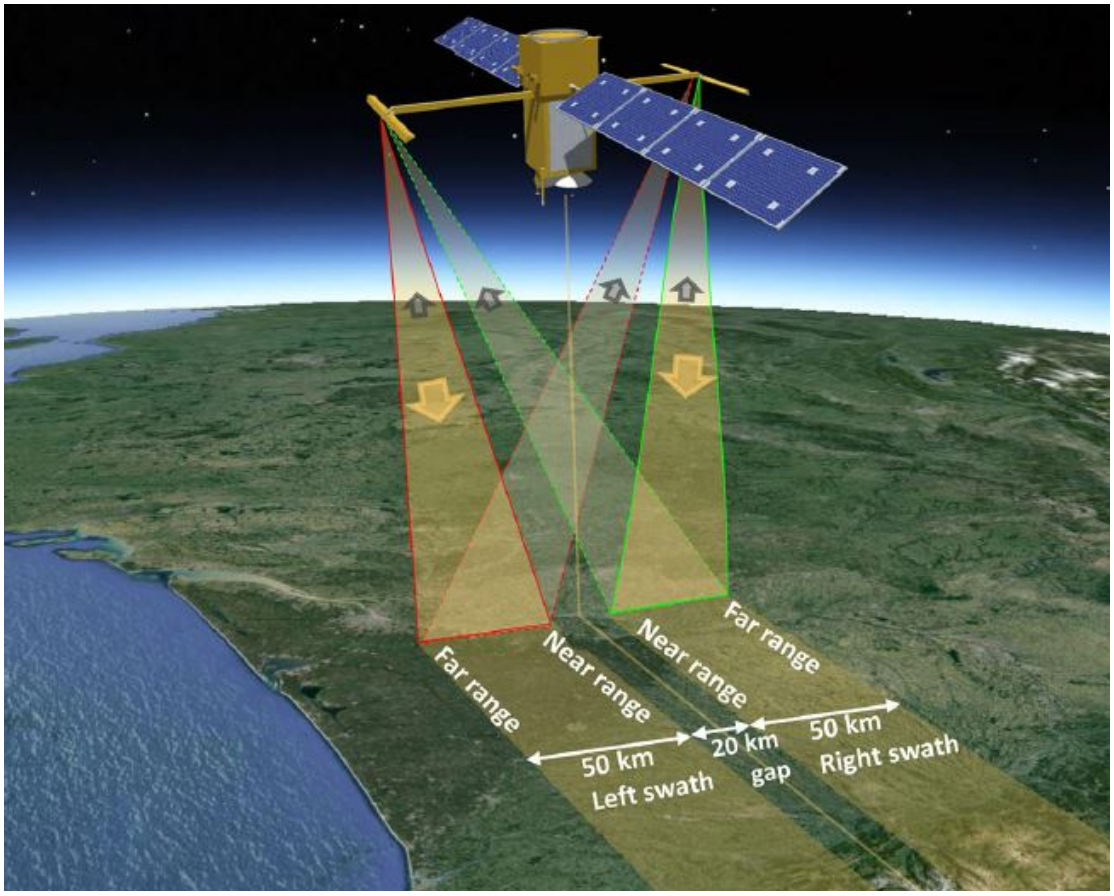

Figure B.1: *Schematic representative of* SWOT *satellite mission with its principal payloads (Biancamaria et al., 2016)*

It is clear that fulfilling these requirements as a main part of SWOT mission's goal strongly depends on orbital geometry and the radar system. A careful repeat orbit design plays an important role in sampling the earth' surface from space by satellites. Choosing the optimized repeat orbit is a key element for successful establishment of a mission. Achieving the mission goal without considering the suitable geometry for satellite orbit is not possible. If satellite mission interests in Hydrological applications, it must be able to monitor water bodies such as lakes and rivers with sufficient spatial and temporal resolution. Current satellite altimetry with their own configurations can not provide enough spatial and temporal coverage over most of the small inland water bodies especially in the arctic region.

B.2.1 Repeat orbit

A repeat orbit mode β/α occurs if the satellite performs β revolutions with respect to its ascending node in α nodal days. β and α are co-prime integer numbers, i.e. they should not have a common factor. One can write $\beta/\alpha = I + N/\alpha$. I the integer part and N is fractional part. Geometrically the β/α ratio means commensurability, i.e. the satellite returns over the same point on its ground track after β revolutions and α nodal days. There are many perturbing force that affect on the satellite repeat orbit. Here we consider only the effect of the earth oblateness on the repeat orbit, called J_2 effect, that is the largest gravitational perturbing force. So we have following equations (Kaula, 1966):

$$\frac{\beta}{\alpha} = \frac{\dot{M} + \dot{\omega}}{\omega_e - \dot{\Omega}} = \frac{T_\Lambda}{T_u} \quad , \tag{B.1}$$

in which:

$$\dot{\Omega} = -\frac{3}{2} n J_2 \left(\frac{R_e}{a}\right)^2 \cos i (1-e^2)^{-2} \quad , \tag{B.2}$$

$$\dot{\omega} = -\frac{3}{4} n J_2 \left(\frac{R_e}{a}\right)^2 (1 - 5\cos^2 i)(1-e^2)^{-2} \quad , \tag{B.3}$$

$$\dot{M} = n - \frac{3}{4} n J_2 \left(\frac{R_e}{a}\right)^2 (1 - 3\cos^2 i)(1-e^2)^{-\frac{3}{2}} \quad , \tag{B.4}$$

and $T_u = \frac{2\pi}{\dot{\omega}+\dot{M}}$, $T_\Lambda = \frac{2\pi}{\omega_e - \dot{\Omega}}$.

If equations (B.2)–(B.4) are substituted in equation (B.1) for a circular orbit, i.e. e=0, we come up with the following equation:

$$\frac{\beta}{\alpha} = \frac{n}{\omega_e} \left\{ 1 - \frac{3}{2} J_2 \left(\frac{R_e}{a}\right)^2 (4\cos^2 i - \frac{\beta}{\alpha}\cos i - 1) \right\}^{-1} \quad . \tag{B.5}$$

This equation describes the relationship between satellite mean motion, n, semi-major axis, a, inclination angle, i, number of revolution, β and repeat cycle, α. In this equation $J_2 = -C_{20}$, ω_e is the angular velocity of the earth and R_e is the earth radius.

B.2.2 Sub-cycle

As mentioned in chapter one the sub-cycle as the time interval between two neighboring tracks, i.e. two ascending or two descending. The sub-cycle is an interesting parameter to measure how fast an orbit reduces the large gap at an arbitrary parallel, e.g. equator, when only ascending or descending tracks are considered. Envisat has a 35 days repeat orbit with 16 days sub-cycle. Figure B.3 shows all ascending ground tracks of Envisat after 16 days at the equator. Sentinel-3 and SWOT have 27 and 21 days repeat orbit with 4 and 10 days sub-cycles respectively. For hydrological purposes an orbit with shorter sub-cycles is preferred because during a short time an altimeter can provide more observations over a given inland water body. As an example figure 2.2 (left panel) shows that Envisat every 16 days (sub-cycle) measures Issykul lake (located in Kyrgyzstan) whereas it's repeat cycle is 35 days. Therefore we have more altimetry data over such a lake that is interesting for hydrologists. Another advantage of an orbit with shorter sub-cycle is related to flood management. During the flood seasons we need measurements with more temporal resolution to control flooded area. An altimeter with a shorter sub-cycle orbit can capture flood events. Therefore the short sub-cycle could be an advantage in repeat orbit design for satellite altimetry mission in hydrological applications. Figure B.2 shows the coverage of SWOT (only nadir) and Envisat over Issykul lake during the sub-cycle.

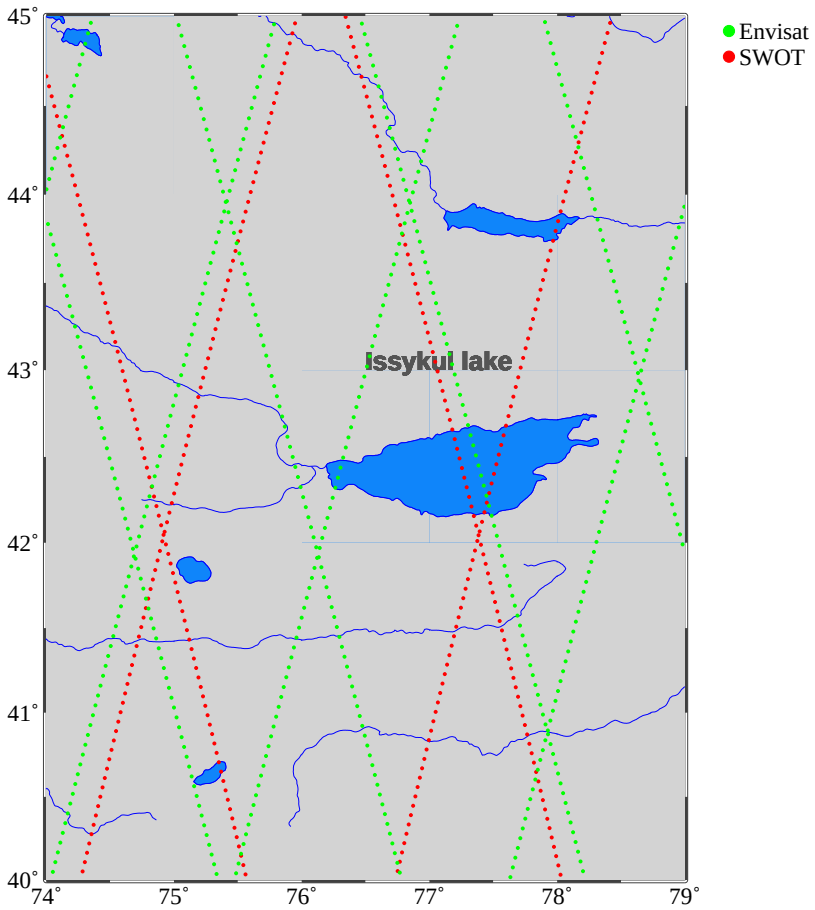

Figure B.2: SWOT *(nadir) and Envisat coverages over and around Issykul lake after 10 and 16 days (sub-cycle) respectively*

B.2.3 Coverage pattern

A coverage pattern shows the ascending or descending ground track density along an arbitrary parallel. It is a useful graphical tool to represent relationship between spatial and temporal sampling. If we consider a repeat mode β/α, we can analytically compute the ground track density along an arbitrary parallel. The ground track interval after one day, $2\frac{\pi}{\beta}\alpha$, is called fundamental interval. A fine interval, s_i, is the angular distance between two neighboring ascending nodes after β revolutions, $s_i = 2\pi/\beta$. Each repeat orbit has a special coverage pattern

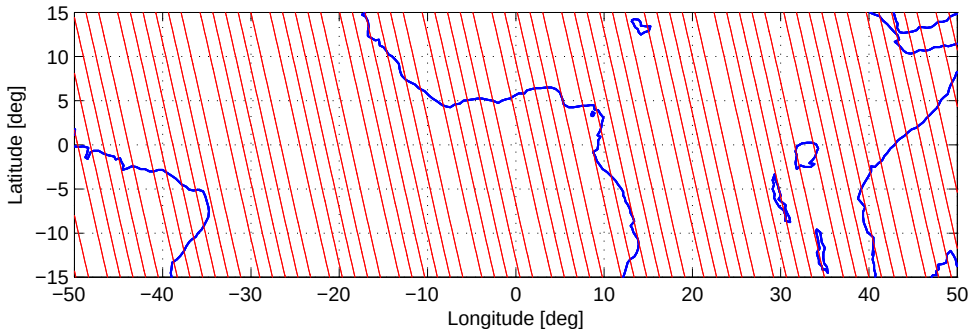

Figure B.3: *Coverage pattern of Envisat during the sub-cycle time (β=501 and α=35)*

for example figures B.3–B.5 show different equatorial coverage patterns for Envisat, Sentinel-3 and SWOT respectively during the sub-cycle.

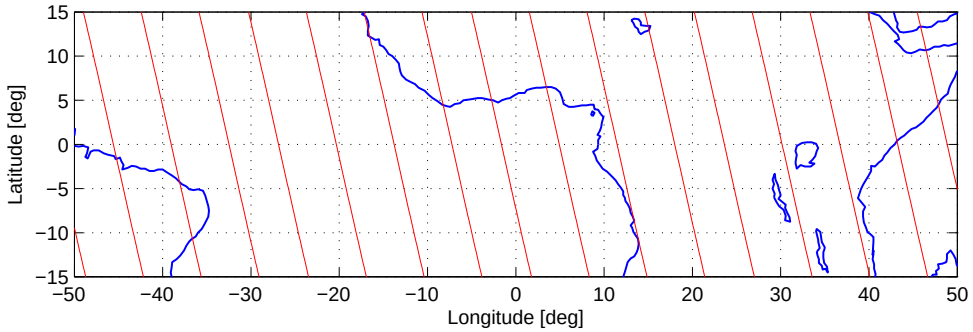

Figure B.4: *Coverage pattern of Sentinel-3 during the sub-cycle (β=385 and α=27)*

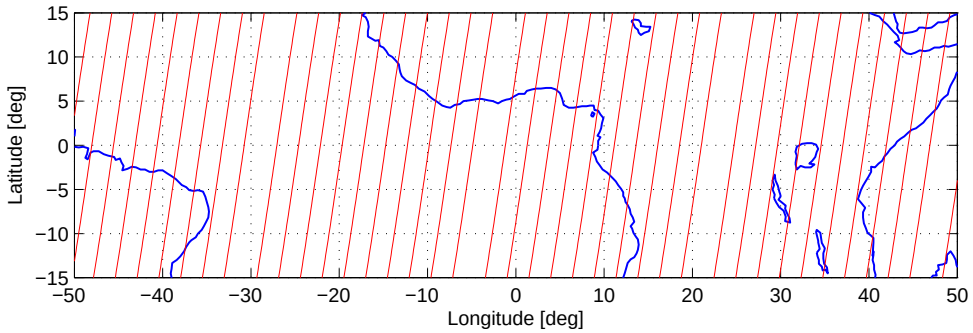

Figure B.5: *Coverage pattern of SWOT during the sub-cycle (β=292 and α=21)*

B.2.4 Gap evolution

To analyze the spatial and temporal resolution a so-called gap evolution graph is used. This graph shows how fast an orbit samples the large gap(Altés et al., 2010). Figure B.6 indicates that after 10 days the maximum and minimum gap width are getting closer to each other, i.e. after this time satellite provides a global homogeneous coverage.

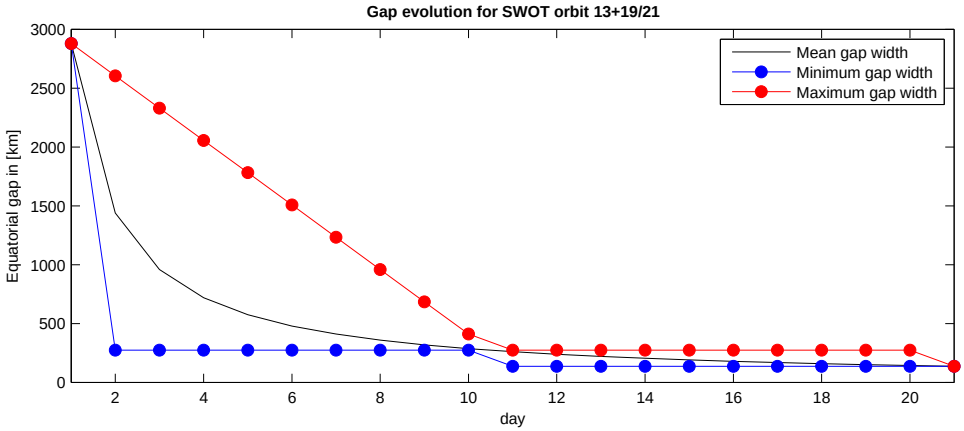

Figure B.6: *Gap evolution graph for a skipping orbit (SWOT), β=292 and α=21*

But for the orbit shown in figure B.7 the maximum and minimum gap width converge after 21 days, i.e. after its repeat cycle. So the orbit shown in figure B.6 is faster than the orbit in figure B.7 to sample the gap (to measure again an object). For a given orbit only being fast (in sampling the gap) is not enough, we must consider its spatial resolution too. For an orbit the higher temporal sampling corresponds to the shorter repeat orbit period and the sparser ground tracks, i.e. satellite only observes the larger inland water bodies. On the other hand the higher spatial resolution needs a longer repeat orbit period that does not satisfy hydrology purposes. Orbits can be classified as drifting orbits and skipping orbits (Altés et al., 2010). In the

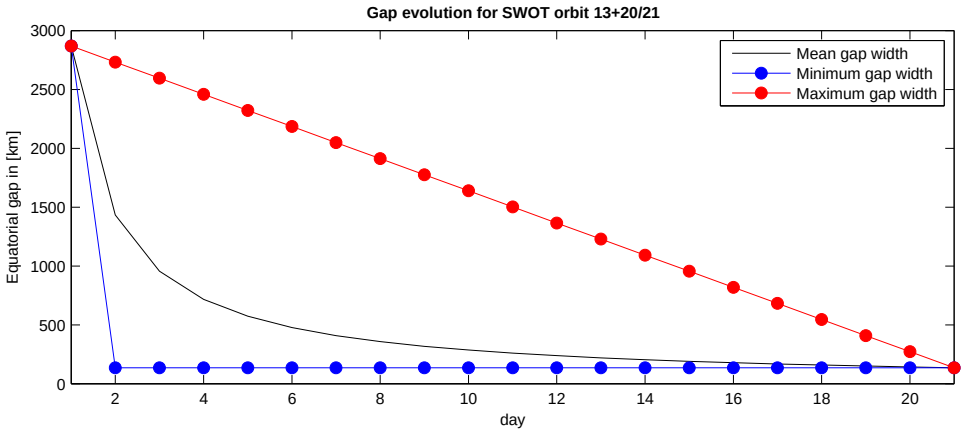

Figure B.7: *Gap evolution graph for a drifting orbit (SWOT), β=293 and α=21*

first type, each track occurs next to previous one. In this type of orbits sampling fundamental

interval will be completed progressively. Figure B.7 indicates a drifting orbit. From this figure we can see that the maximum and minimum gap curves are getting closer to each other slowly. In the second type of orbit, the fundamental interval is sampled in a more random way and filling the large gap in the fundamental interval is faster than that drifting orbits would do.

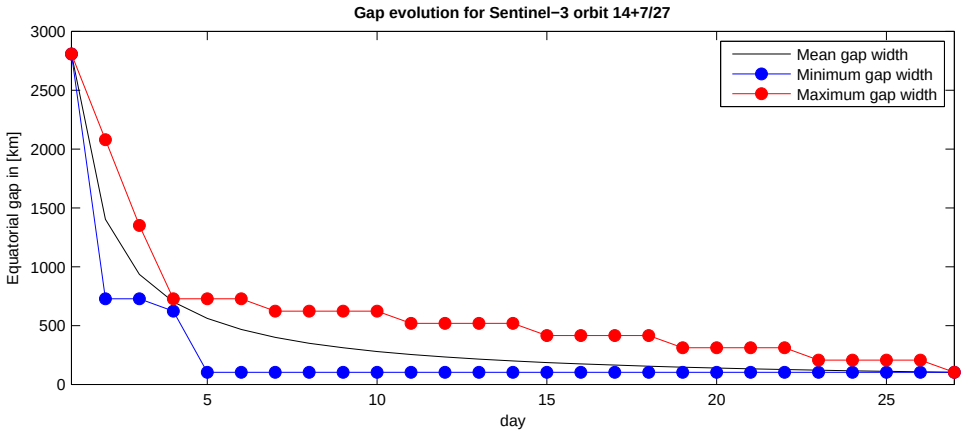

Figure B.8: *Gap evolution graph for a skipping orbit (Sentinel-3), β=385 and α=27*

B.2.5 Temporal and spatial sampling

One can analyze spatial and temporal resolution together or separately. The temporal resolution (revisit time) is the time elapsed between two successive passes over a given object that depends on the repeat orbit period and measurement mode as well as the geographical location of the object. For nadir altimeters the revisit time is equal to full repeat cycle or sub-cycle period but for the SWOT mission, equipped with a swath altimeter, the revisit time will be shorter than the sub-cycle. For instance the revisit time for an arbitrary point located at 69° latitude is 13 and 18 for an orbit with 23 days repeat cycle with inclination angle 74° and 78° respectively. For a conventional altimeter like RA-2 (on-board the Envisat) the temporal resolution for the same point with this rate is impossible.

To analyze the spatial resolution the inter-ground track spacing can be used. The spatial resolution is also a function of geographical location (latitude) of the object. Table 2.3 represents the spatial resolution of different missions at equator.

For hydrological applications one needs to consider spatial and temporal resolution simultaneously and to make a proper balance between them. In a repeat orbit mode β/α, the repeat period is T_{rep}=α nodal day and the revolution time is T_{rev}= α/β nodal day. If we consider the spatial resolution at equator as: D_{space}=$2\pi/\beta$ radian. For temporal scale we simply use D_{time}=α nodal day. Multiplication of the spatial resolution, D_{space}, and temporal resolution, D_{time}, leads to (Reubelt et al., 2010):

$$D_{\text{space}} \times D_{\text{time}} = \frac{2\pi\alpha}{\beta} = 2\pi T_{\text{rev}} \quad . \tag{B.6}$$

Since revolution time, T_{rev}, for a low earth orbiting satellite (LEO) such as SWOT is varying only marginally with the orbit height, i.e. T_{rev} (H_{min}=750 km) $\cong$ 1.66 h and T_{rev} (H_{max}=1000 km) $\cong$ 1.75 h, the product D_{space} and D_{time}:

$$D_{space} \times D_{time} = c \ , \tag{B.7}$$

can approximately be considered as a constant. Reubelt et al. (2010) called it Heisenberg uncertainty principle. According to this principle (equation (B.7)) the better spatial resolution the worse temporal resolution and vice versa. Figure B.9 shows relationship between spatial and temporal resolution based on the equation (B.7) for all possible orbits of SWOT mission.

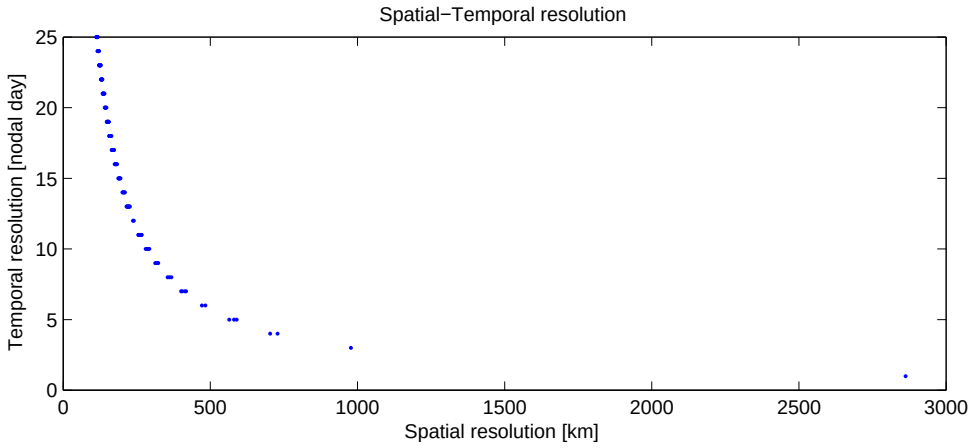

Figure B.9: *Spatial- Temporal resolution for* SWOT *with orbit heights between* 750 km *and* 1000 km

B.3 Possible orbits

One can study all possible orbits with orbit heights between two limited heights, maximum and minimum orbit heights, and select an optimized orbit depend on the mission purpose. To repeat an orbit, determining semi-major axis consistent to the repeat mode β/α is fundamental otherwise there are irregularities in ground track pattern and the ground track would not be repeated. According to Kaula (1966) in the repeat orbit at the presence of J_2 effect, the following relationship between satellite mean motion, n, semi-major axis, a, and inclination angle, i, should be satisfied:

$$n = \frac{\beta}{\alpha}\omega_e\{1 - \frac{3}{2}J_2(\frac{R_e}{a})^2(4\cos^2 i - \frac{\beta}{\alpha}\cos i - 1)\} \ , \tag{B.8}$$

in which J_2=-C_{20} , ω_e is the angular velocity of the earth and R_e is the earth radius. The orbit height via semi-major axis of the orbit is involved in this equation and $n = \sqrt{GM/a^3}$, i.e. the semi-major axis of orbit, a, appears in both sides of equation (B.8). To find a proper a required for repeat orbit scenario we use the Wagner's algorithm (Wagner, 1990):

$$a_0 = \{GM^2(\frac{\alpha}{\beta})^2\frac{1}{\omega_e^2}\}^{\frac{1}{3}} \ , \tag{B.9}$$

$$a_{i+1} = a_0[1 - \frac{3}{2}J_2(\frac{R_e}{a_i})^2(1 - \frac{3}{2}\sin^2 i)]^{\frac{2}{3}} \times [1 + J_2(\frac{R_e}{a})^2\{\frac{3}{2}(\frac{\beta}{\alpha})\cos i - \frac{3}{4}(5\cos^2 i - 1)\}]^{\frac{2}{3}} \quad , \quad \text{(B.10)}$$

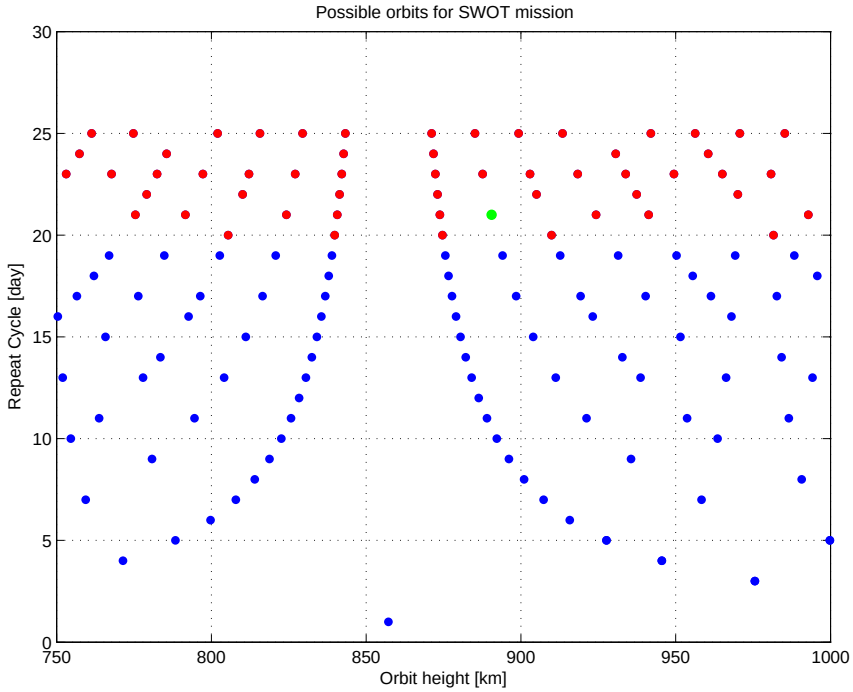

Figure B.10: *Different orbits with* 750 km$\leq H \leq$1000 km, i=77.6° *and* $\alpha \leq$25 *day*

After computing a the orbit height is determined because $H = a - R_e$. On the other hand based on equation (B.9) the repeat ratio, $ratio = \beta/\alpha$, can also be computed from the maximum and minimum a corresponds to the maximum and minimum orbit height $\beta = \alpha \times ratio$. So to have different orbit scenarios it is enough to select the maximum and minimum orbit heights, an inclination angle as well as a repeat orbit period. In figure B.10 all possible orbits between 750 km and 1000 km orbit heights with an inclination angle of 77.6° as well as the repeat orbit period less than 25 days for this mission were plotted. x-axis shows the orbit heights H, y-axis is repeat orbit period α and each dot is an orbit correspond to (H, α).

B.4 Candidate orbits

Based on the gap evolution graph, coverage pattern and spatial-temporal resolution, among all possible orbits with the orbit heights between 750 km and 1000 km and the repeat orbit period between 20 and 25 nodal days there are number of orbits that can be better choices and they can be candidate orbits for SWOT mission. The red dots on figure B.10 show these options for the nominal phase of this mission. Table B.1 includes more information about these possible candidate orbits. According to Biancamaria et al. (2016) an orbit with a 77.6° inclination, a 21 days repeat cycle and 891 km altitude has been selected for SWOT mission. The green dot on figure B.10 represents this orbit. This scenario is also highlighted in table B.2.

Table B.1: *All possible orbits with the orbit heights between* 750 km *and* 1000 km *for SWOT mission*

α	β	Orbit height (km)	Ground track separation (km) at equator
20	273	981.60	146.79
20	277	909.88	144.68
20	279	874.65	143.64
20	281	839.84	142.62
20	283	805.44	141.61
21	286	992.86	140.12
21	289	941.26	138.67
21	290	924.25	138.19
21	292	890.53	137.24
21	293	873.82	136.77
21	295	840.66	135.85
21	296	824.23	135.39
21	298	791.63	134.48
21	299	775.46	134.03
22	301	970.18	133.14
22	303	937.38	132.26
22	305	905.05	131.39
22	307	873.06	130.54
22	309	841.41	129.69
22	311	810.10	128.86
22	313	779.13	128.04
23	314	980.81	127.63
23	315	965.08	127.22
23	316	949.42	126.82
23	317	933.85	126.42
23	318	918.36	126.02
23	319	902.95	125.63
23	320	887.62	125.23
23	321	872.37	124.84
23	323	842.10	124.07
23	324	827.08	123.69
23	325	812.14	123.31
23	326	797.27	122.93
23	327	782.48	122.55
23	328	767.76	122.18
23	329	753.12	121.81
24	329	960.5	121.81
24	331	930.62	121.07
24	335	871.73	119.63
24	337	842.73	118.92
24	341	785.55	117.52
24	343	757.38	116.84
25	341	985.23	117.52
25	342	970.73	117.18
25	343	956.30	116.84
25	344	941.94	116.50
25	346	913.42	115.82
25	347	899.26	115.49
25	348	885.18	115.16
25	349	871.15	114.83
25	351	843.30	114.17
25	352	829.48	113.85
25	353	815.72	113.53
25	354	802.02	113.21
25	356	774.81	112.57
25	357	761.31	112.25

Table B.2: *Candidate orbits for the nominal phase of* SWOT *satellite mission*

α	β	Sub-cycle (day)	Orbit height (km)	Ground track separation (km) at equator
20	273	3	981.60	146.79
20	277	7	909.88	144.68
21	286	8	992.86	140.12
21	289	4	941.26	138.67
21	290	5	924.25	138.19
21	**292**	10	**890.53**	**137.24**
21	296	10	824.23	135.39
22	301	3	970.18	133.14
22	303	9	937.38	132.26
22	305	7	905.05	131.39
23	314	3	980.81	127.63
23	315	10	965.08	127.22
23	316	4	949.42	126.82
23	317	9	933.85	126.42
23	318	6	918.36	126.02
23	319	8	902.95	125.63
23	325	8	812.14	123.31
24	329	7	960.5	121.81
24	331	5	930.62	121.07
25	341	11	985.23	117.52
25	343	7	956.30	116.84
25	344	4	941.94	116.50
25	346	6	913.42	115.82
25	347	8	899.26	115.49
25	353	8	815.72	113.53
25	354	6	802.02	113.21

B.5 Water level/surface monitoring from SWOT-like data

SWOT simulated data has been provided by Gaultier et al. (2016). They used an Ocean General Circulation Model (OGCM) to retrieve Sea Surface Height (SSH) based on the radar system characteristics and orbital geometry of the SWOT mission. To this end, they interpolated the model spatially (2D interpolation) over grid points of the SWOT swath width. The grid size is 1 km in the along track and cross track directions. In the cross track direction the grid is defined between 10 km and 60 km off nadir (figure B.11).

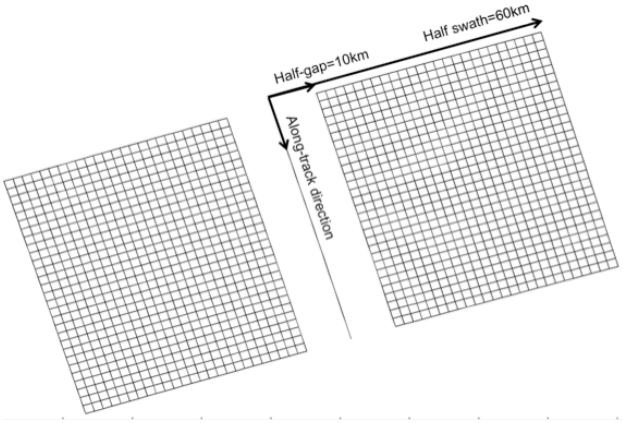

Figure B.11: *Schematic representative of* SWOT *grid at* 1 km *resolution*

Then noises and measurement errors have been added to interpolated SSH observations to make them close to reality as much as possible. Simulated measurement errors include instrument and geophysical errors. According to Gaultier et al. (2016) instrument errors used in the simulated SWOT data include KaRIN noises, roll, phase, baseline dilation and timing errors. So far, only the wet tropospheric error (the major geophysical error) has been used to provide the SWOT-like data. More detail about these errors and how they have been implemented are described in Gaultier et al. (2016).

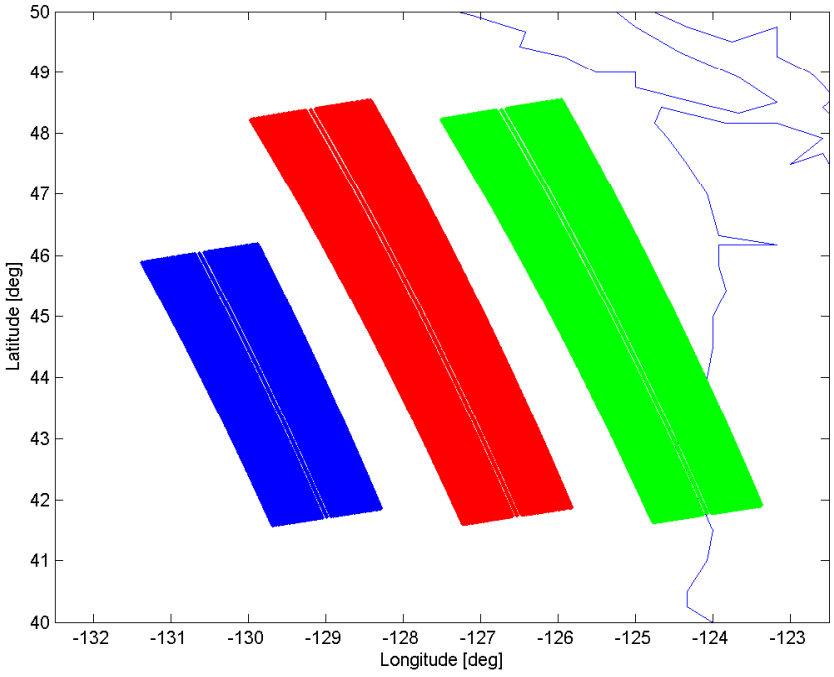

Figure B.12: SWOT *simulated coverage over Oregon coast*

Figure B.12 represents the simulate coverage of SWOT mission for three passes over Oregon coastal zone. The coverage of the middle pass has been zoomed in figures B.13 and B.14 to show SWOT sampling behavior. As mentioned before the main difference between SWOT and nadir altimetry mission is that SWOT will provide the water surface variations. Figure B.15 shows the water surface variations from the middle pass in figure B.12. One can extract a water level profile from this water surface variations. Figure B.16 represents water level variations of Oregon coast based on the SWOT simulated data.

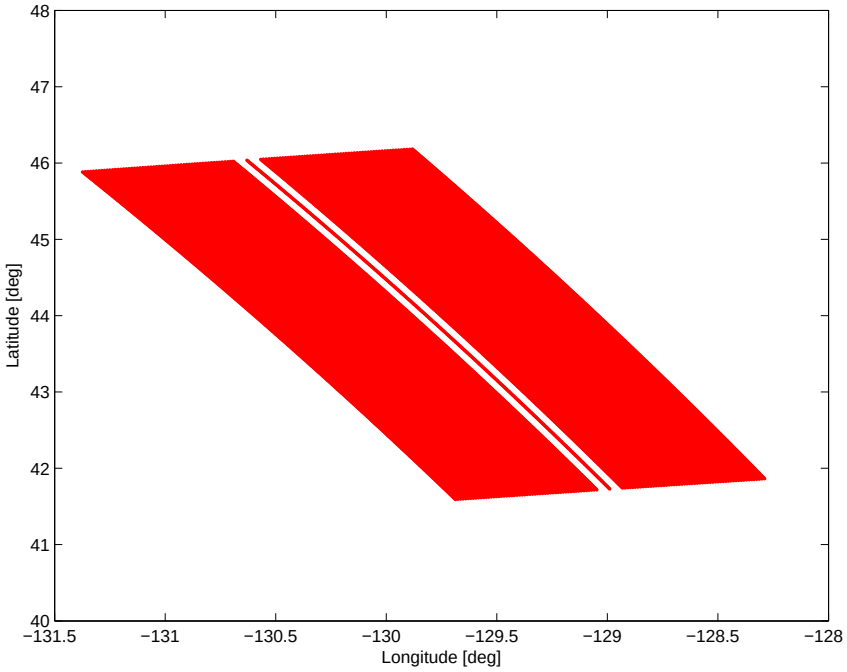

Figure B.13: SWOT *simulated coverage over Oregon coast*

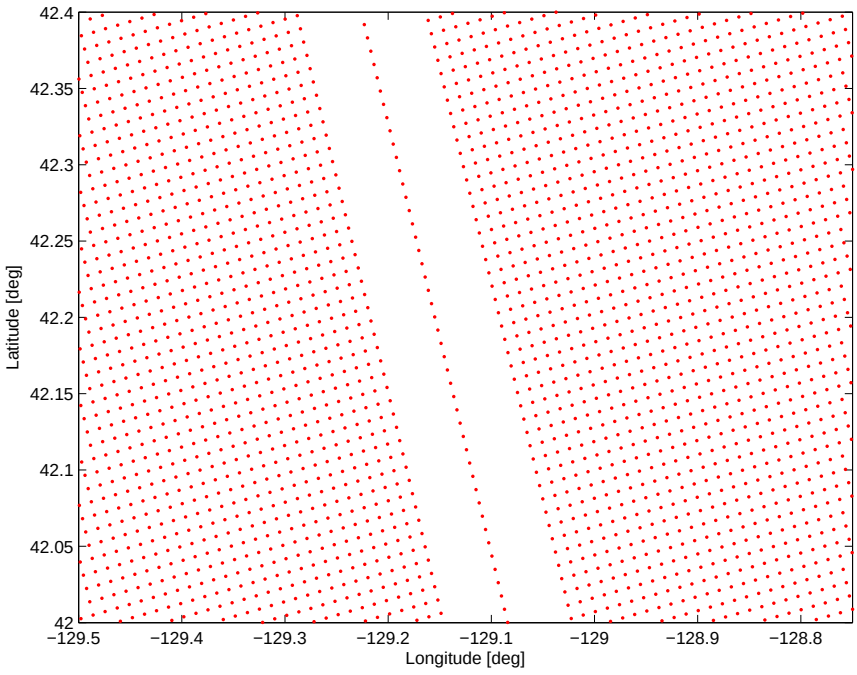

Figure B.14: SWOT *simulated coverage over Oregon coast*

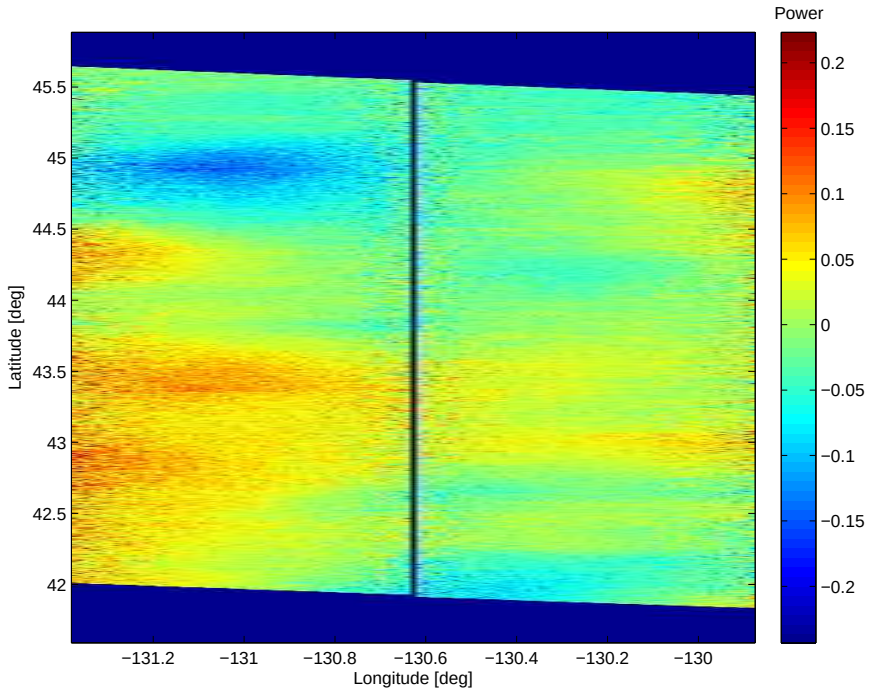

Figure B.15: *Water surface variations of Oregon coast from* SWOT *simulated data*

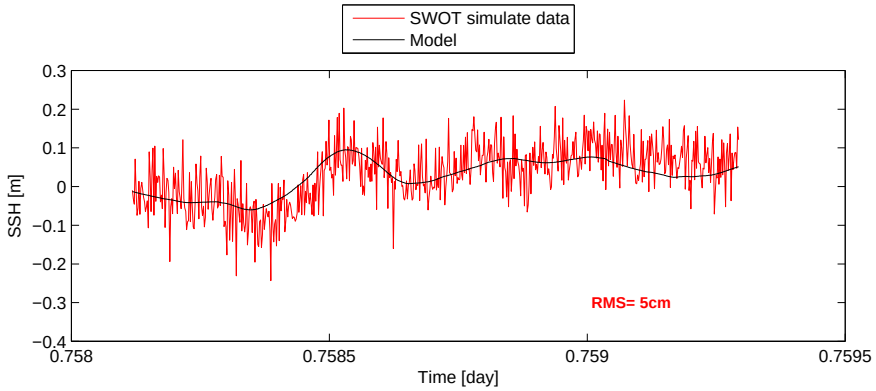

Figure B.16: *Water level variations of Oregon coast from* SWOT *simulated data*